An X-ray Scattering Study of the Nanoscale Structure of C_{70}-Pentacene Heterostructures and Metal-Halide Perovskite Nanocrystallites

Janina Melanie Roemer

München 2019

AN X-RAY SCATTERING STUDY OF THE NANOSCALE STRUCTURE OF C_{70}-PENTACENE HETEROSTRUCTURES AND METAL-HALIDE PEROVSKITE NANOCRYSTALLITES

JANINA MELANIE ROEMER

DISSERTATION

Fakultät für Physik
der
Ludwig-Maximilians-Universität

vorgelegt von
Janina Melanie Roemer
aus München

München, den 9. April 2019

ERSTGUTACHTER: PD Dr. Bert Nickel
ZWEITGUTACHTER: Prof. Dr. Thomas Weitz
TAG DER MÜNDLICHEN PRÜFUNG: 22. Mai 2019

ZUSAMMENFASSUNG

Die steigende weltweite Nachfrage nach elektronischen Geräten macht es immer wichtiger, klimaverträgliche Herstellungsverfahren zu entwickeln. Dazu müssen Halbleitermaterialien untersucht werden, die energieeffizient herzustellen sind, besonders solche, die sich für photovoltaische Anwendungen eignen. Die beiden Materialgruppen der organischen Halbleiter und Metallhalogenid-Perowskite entsprechen diesen Anforderungen. Ein besseres Verständnis der Struktur dieser Materialien im Nanobereich und von deren Einfluss auf die optoelektronischen Eigenschaften wäre gewinnbringend für die weitere Entwicklung dieser Forschungsgebiete.

In der vorliegenden Arbeit werden verschiedene komplementäre Röntgenstreutechniken verwendet, um die strukturellen Eigenschaften zweier Materialsysteme aufzuklären. Als Vertreter der organischen ambipolaren Heterostrukturen wurden Pentacen-C_{70}-Doppelschichten untersucht, die durch Molekularstrahl-Deposition hergestellt wurden. Dabei stand die Frage im Mittelpunkt, wie Kristallstruktur, Parakristallinität und Aggregatanordnung bei der Probenherstellung beeinflusst werden können. Die zweite untersuchte Materialklasse sind in porösen Filmen eingeschlossene Metallhalogenid-Perowskit-Nanopartikel, hergestellt von Kooperationspartnern an der Johannes Kepler Universität Linz. Durch Kristallisation in unterschiedlichen Porenmorphologien kann die Wellenlänge der Emission der Perowskite gesteuert werden. Um die optoelektronischen Eigenschaften gezielt einstellen zu können, ist die Kenntnis von Größe und Form der dabei entstehenden Perowskitkristallite sowie der sie umgebenden Poren von wesentlicher Bedeutung. Röntgenreflektivitätsmessungen an Pentacen-C_{70}-Doppelschichten, die an der High Resolution Beamline P08 am Deutschen Elektronen-Synchrotron (DESY) durchgeführt wurden, lieferten geeignete Daten für eine präzise Bestimmung des Netzebenenabstands entlang der Probennormalen und eine Quantifizierung seiner Regelmäßigkeit. Durch Anwendung von Hosemanns Theorie der Parakristalle konnte gezeigt werden, dass sich die Parakristallinität von C_{70}-Schichten durch gezielte Wahl der Aufdampftemperatur erheblich beeinflussen lässt. Die minimale Parakristallinität von 2.3 % wurde für C_{70}-Schichten erreicht, die bei 75 °C aufgedampft wurden. Für eine Aufdampftemperatur von 25 °C ergab sich eine Parakristallinität von 5.4 %. Die Daten zeigten zudem, dass eine Erhöhung der Aufdampftemperatur um 80 °C mit einer relativen Zunahme des Netzebenenabstands entlang der Probennormalen um 1.4 % verbunden ist. Die damit verbundenen Änderungen

der dreidimensionalen Kristallstruktur wurden mithilfe von Röntgenweitwinkelstreuung unter streifendem Einfall untersucht. Die Unterschiede der Streubilder konnten durch einen kontinuierlichen Übergang der C_{70}-Struktur von einer rhomboedrischen zu einer kubisch flächenzentrierten Phase erklärt werden. Röntgenkleinwinkelstreuungsexperimente unter streifendem Einfall deuten darauf hin, dass sich bei der Anordnung von C_{70}-Nanoaggregaten auf Pentacen-Schichten zwei charakteristische Abstände ergeben. An diese Ergebnisse können zukünftige experimentelle Untersuchungen des Einflusses der Nanostruktur auf unterschiedliche (opto)elektronische Eigenschaften der Materialien anknüpfen. Diese könnten sich beispielsweise mit dem Ladungstransport oder der Effizienz der Ladungsträgertrennung an der Grenzfläche befassen.

Weitwinkelstreuexperimente mit hochenergetischer fokussierter Röntgenstrahlung ermöglichten die Untersuchung von Größe und Form von Perowskit-Nanokristallen in 1-40 µm dicken porösen Schichten. Die Messungen wurden an P07, DESY, durchgeführt. Um das Streusignal zu erhöhen und in eine Komponente in der Probenebene und eine senkrecht dazu stehende trennen zu können, wurden die mehrere Millimeter langen Proben parallel zum Direktstrahl einjustiert. Die Auswertung ergab eine minimale Kristallitgröße von 1.8 nm in nanoporösem Silizium, die mit der Stromdichte, die beim Ätzprozess der porösen Schicht angelegt wird, zunimmt. In nanoporösem Aluminiumoxid wurde eine starke Anisotropie der Kristallite beobachtet. In der Probenebene ergab sich eine Kristallitlänge von 13 nm, entlang der Probennormalen etwa der doppelte Wert. Eine Ergänzung dieser Ergebnisse durch Kleinwinkelstreumessungen an ungefüllten porösen Schichten zeigte, dass die Kristallitlänge in nanoporösem Silizium etwa halb so groß ist wie der Porendurchmesser. In nanoporösem Aluminiumoxid hingegen scheinen die Kristallite den gesamten Querschnitt der Poren zu füllen. Diese Ergebnisse bieten Einblicke in den Prozess der Kristallitbildung in den Poren und tragen zu einem besseren Verständnis der optoelektronischen Eigenschaften und deren möglicher Beeinflussung durch verschiedene poröse Materialien bei.

Die vorliegende Dissertation leistet einen Beitrag zur Klärung der Frage, wie Struktur und Morphologie der untersuchten Materialsysteme durch die Wahl der Herstellungsparameter beeinflusst werden können. Sie bietet dadurch eine Grundlage um von einem experimentellen Ansatz aus ein besseres Verständnis der Zusammenhänge zwischen strukturellen und optoelektronischen Eigenschaften zu erreichen.

ABSTRACT

The growing worldwide demand for electronic devices increases the importance of finding climate-friendly production pathways. This setting motivates the investigation of semiconductors that can be processed energy efficiently, especially those that show potential for photovoltaic applications. The two material classes of organic semiconductors and metal-halide perovskites match these conditions. Understanding the nanoscale structure of these materials and how it influences the optoelectronic properties can provide important information for an advancement of the fields.

In this work several complementary X-ray scattering techniques were applied to examine various structural properties of two different material systems. Molecular beam deposited pentacene-C_{70} bilayers were investigated, as an example of organic ambipolar heterostructures. Here, the question of how crystal structure, disorder, and aggregate distribution can be adjusted by controlling the vacuum deposition parameters was addressed. The second material class investigated are metal halide perovskite nanoparticles, processed by spatial confinement in porous thin films. This method, developed and applied by members of the Johannes Kepler University Linz, can be used to control the perovskites emission wavelength directly within device-relevant structures. Here, information about the size and shape of perovskite crystallites as well as of the surrounding pores is important to allow for a well-directed tuning of the optoelectronic properties.

X-ray reflectivity measurements of pentacene-C_{70} bilayers performed at the High Resolution Beamline P08 at *Deutsches Elektronen-Synchrotron* (DESY) provided suitable data for quantifying the out-of-plane lattice spacing as well as its regularity. Applying the paracrystal theory developed by Hosemann revealed that the paracrystalline distortion of the C_{70} layers can be adjusted in a wide range by choice of the sample temperature during C_{70} deposition. A minimum paracrystalline distortion of 2.3 % occurs in C_{70} deposited at 75 °C, while a paracrystalline distortion of 5.4 % was found for deposition at 25 °C. The same data revealed a 1.4 % increase of the C_{70} out-of-plane lattice spacing for a deposition temperature increase of 80 °C. The respective changes of the three-dimensional crystal structure were investigated by grazing-incidence wide-angle diffraction. The differences of the diffraction patterns could be explained by a continuous transition from a rhombohedral phase to face-centred cubic structure of the fullerene. Grazing-incidence small-angle scattering revealed two characteristic length scales in the mor-

phology of C_{70} nanoaggregates on pentacene films, which are assigned to the distances of aggregates along and across pentacene step edges. The combined results provide a sound basis for future experiments investigating the effect of nanoscale structure on different (opto)electronic properties of the materials, such as charge transport or the efficiency of charge carrier separation at the heterojunction.

Accessing the size and shape of perovskite nanocrystals confined in 1-40 µm thick porous films was possible by high-energy X-ray microbeam wide-angle diffraction measurements performed at beamline P07 at DESY. Aligning the several-millimetre long films parallel to an incoming ~ 100 keV X-ray beam that was focussed onto their transverse plane enhanced the scattering signal and allowed for separation of in- and out-of-plane information. In nanoporous silicon, almost isotropic crystallites as small as 1.8 nm were observed. They increase in size with increasing etching current density that was applied to prepare the porous film. In nanoporous alumina, strongly anisotropic crystallites were observed, with an in-plane size of 13 nm and twice that size along the surface normal. Complementing this information with an analysis of small-angle scattering data of unfilled porous films indicates that the crystallite size in nanoporous silicon is only about half the pore diameter, while the crystallites in nanoporous alumina appear to fill the entire cross section of regularly arranged tubular pores. These results provide insights into the process of crystallite formation within the pores, helping to understand the observed optoelectronic properties and how they are affected by the differences of the two porous materials.

This dissertation helps to clarify how structure and morphology of the two investigated material systems can be tuned by the choice of processing parameters, thereby providing an experimental building block towards a better understanding of the correlation between structural and (opto)electronic properties.

CONTENTS

ACRONYMS

2d	two-dimensional
AFM	atomic force microscopy
$CsPbBr_3$	caesium lead tribromide
DESY	Deutsches Elektronen-Synchrotron
DMF	dimethylformamide
fcc	face-centred cubic
ESRF	European Synchrotron Radiation Facility
FWHM	full width at half maximum
GISAXS	grazing-incidence small-angle X-ray scattering
GIWAXS	grazing-incidence wide-angle X-ray scattering
HOMO	highest occupied molecular orbital
JKU	Johannes Kepler University Linz
LaB_6	lanthanum hexaboride
LED	light-emitting diode
LMU	Ludwig Maximilian University of Munich
LUMO	lowest unoccupied molecular orbital
$MAPbBr_3$	methylammonium lead tribromide
$MAPbI_3$	methylammonium lead triiodide
npAAO	nanoporous anodic aluminium oxide
npSi	nanoporous silicon
$PbBr_2$	lead(II) bromide
PbI_2	lead(II) iodide
PL	photoluminescence
SAXS	small-angle X-ray scattering

SEM	scanning electron microscopy
SiO_2	silicon dioxide
TEM	transmission electron microscopy
WAXS	wide-angle X-ray scattering

Part I

INTRODUCTION

1

MOTIVATION

The worldwide growing demand for electronic devices strongly motivates research aiming for energy-efficient production methods. Semiconducting materials that can be processed at low temperatures have received close attention in recent decades. In the 1980s the research field of organic electronics evolved and in 2012 organic-inorganic halide perovskite electronics became a rapidly developing field [1, 2]. Both classes of materials have shown promising results in photovoltaics [3, 4]. Investigating them thus has a double relevance in climate-change mitigation: it has the potential to advance the prospects of energy-efficient production of electronic devices as well as to increase the percentage of energy gained from photovoltaics by serving niche markets. Both technologies allow for light-weight, flexible and semitransparent devices [5–9]. Thus they can be applied for purposes that conventional inorganic solar cells are typically not suited for. The combination of light weight and flexibility makes low-temperature processable electronics attractive for installation on roofs of vehicles, tents or houses in regions where frail construction forms are prevalent [10]. Semitransparency additionally makes window areas accessible for solar energy generation [6, 9, 11, 12]. Another application in which organic semiconductors and perovskites have a distinct advantage over their purely inorganic counterparts is as active layers in light-emitting diodes. Both material classes are well known for narrow band emission, i.e. high colour purity, making them attractive for display applications. In this context, a main advantage of metal-halide perovskites is their suitability to tuning of the emission wavelength. Offering two rapidly investigated approaches of wavelength adjustment, namely mixed halide stoichiometry and quantum confinement, the emission can be tuned in the entire visible range [13].

While perovskite electronics still has obstacles to overcome to allow for a successful commercialisation [4, 14] organic solar cells have already been brought to niche markets. Despite considerable progress over the last years, the efficiencies of organic solar cells are still rather low compared to many other photovoltaic technologies [3, 15]. Recently, the biggest successes have been achieved by optimising the exploitation of the incident light, either by applying ternary [16] or tandem cell strategy [3] in contrast to improvements of the charge carrier separation at the heterojunction. To more efficiently exploit the potential for improvement arising from this central process that is

of essential importance for all organic solar cell architectures, it is neccessary to understand it on a nanoscale level [1]. Charge carrier separation, transport and recombination are known to be closely related to structure at the nanoscale; the details about the relation are however still the topic of debate, suggesting that additional studies are still required [17–20]. A controversial topic is how domain size and crystallinity are correlated to charge carrier separation efficiency [21, 22]. Tackling this question from an experimental approach requires control over the nanoscale structural properties of the materials involved and their interface. Detailed knowledge is needed about crystal structure and quality, domain sizes, and orientation of the molecules at the interfaces to each other and how they can be controlled during sample preparation.

Focussing on molecular beam deposition of a photovoltaic-relevant system of small molecules, namely the fullerene C_{70} and pentacene, this work aims to contribute to a better understanding of the correlation between structural and optoelectronic properties in two ways. Firstly, by investigating the influence of deposition parameters (i.e. the C_{70}-deposition temperature and rate) on the crystal structure and quality of C_{70} layers deposited on thin-film phase pentacene, showing that the paracrystalline distortion of C_{70} can be tuned in a wide range by adjusting the C_{70}-deposition temperature. Secondly, by describing a method to produce disconnected nanointerfaces between C_{70} and pentacene thin films and by investigating the influence of the C_{70}-deposition temperature on their morphology. This system has the advantage of well-defined individual interfaces, which can be assumed to be free of fullerene grain boundaries. This can be expected to considerably facilitate interpretation of experiments, increasing the chances of drawing reliable conclusions.

Quantum confinement of metal-halide perovskites is another example where optoelectronic properties are strongly dependent on the nanoscale structure. Here the most dominant factor influencing the emission is particle size. The work presented in this thesis includes a detailed X-ray diffraction and scattering study of metal-halide perovskite nanocrystals confined in nanoporous layers of anodised aluminium oxide and electrochemically etched silicon. This method of spatial confinement in thin films was developed by members of the Linz Institute of Organic Solar Cells and the Department of Soft Matter Physics and has already been successfully applied to fabricate LEDs with blue-shifted emission. A well-directed improvement of the method would rely on profound knowledge of the structural properties of the nanoparticles that evolve under different preparation conditions. This thesis aims to contribute to this goal by providing insights into shape and size of the nanopores as well as of the perovskite particles forming inside them. In nanoporous silicon the dependency of the perovskite crystallite

size on the etching current density was analysed. Additionally, the evolution of crystallite sizes over the depth of the tens of micrometres-thick layers was investigated and the distribution of perovskite crystallites and residual precursor material was analysed. Altogether the study provides a detailed picture of the structural properties of the samples, with relevant implications for the development of strategies for future manufacturing techniques.

Accessing all those different aspects of the nanostructure of the two different investigated material systems was possible by using various X-ray scattering and diffraction techniques. Diffraction provides unique resolution, even making differences in lattice spacing in the order of 10^{-2}Å observable. While imaging techniques as atomic force microscopy and transmission electron microscopy are valuable tools to pre-characterise samples, they only provide insight into small sample areas. X-ray scattering in contrast allows to average over significant sample volumes, and thus provides much better statistics. By choosing the scattering geometry and beam parameters, the experimenter can decide which part of the sample volume to probe.

In Chapter 2 the material systems investigated here will be briefly introduced. Chapter 3 will then deal with the question of how the relevant structural information can be accessed, introducing the associated concepts of diffraction analysis as well as discussing the advantages of different methods. Experimental details about the methods as applied in these studies are described in Part ii. The results of the work are presented and interpreted in Part iii. Part iv provides a summary of the findings and an outlook to suggested follow-up research.

2

MATERIALS INVESTIGATED

2.1 MOLECULAR SEMICONDUCTORS - PENTACENE-C_{70} HETEROSTRUCTURES

Organic electronics is based on hydrocarbons and other molecules that exhibit sp^2-hybridisation of carbon. The remaining unhybridised p_z-orbitals of neighbouring atoms can overlap, allowing electrons to delocalise across the molecule and form π-orbitals. In the ground state, there are no vacancies in the energetically highest occupied molecular orbital (HOMO). Semiconducting properties of the material arise from the energetic gap to the lowest unoccupied molecular orbital (LUMO). In the aggregated state, overlap between the π-orbitals of adjacent molecules can occur, enabling charge carrier transport across the van der Waals solid [23]. The electrical properties of the aggregate strongly depend on molecular packing, as this influences the electronic coupling between adjacent molecules as well as the polarisation effects of neighbouring molecules and consequently the energies of HOMO and LUMO in the solid [24]. Highly ordered ultrapure single crystals usually show the highest charge carrier mobilities [17]. Here charge transport can be described by the band-like transport model, i.e. the wave function of the charge carrier is delocalised over several molecules. In amorphous solids charge carrier mobilities are low and transport is usually thermally activated [17, 23, 25]. In polycrystalline thin films with a certain degree of disorder, predicting charge carrier mobility is challenging, as it is influenced by a large number of factors that are difficult to quantify. Among these are grain size, order within the individual domains, orientation of the domains to each other and impurities.

Organic semiconductors exihibit strong absorbtion in the solar spectrum, and are thus attractive materials for photovoltaics. Photon absorption in organic films creates excitons, i.e. Coulombically bound electron-hole pairs that need to be dissociated in order to generate a current. This dissociation is facilitated at heterojunctions between a donor, i.e. a material with low ionisation potential, and an acceptor, i.e. a material with high electron affinity. Charge carriers can then separate along the donor and acceptor respectively and be collected at the two opponent electrodes [26, 27]. Consequently the power conversion efficiency of an organic solar cell depends on the (opto)electrical

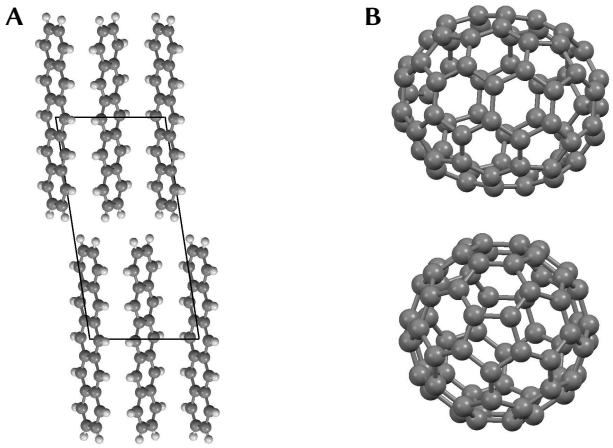

FIGURE 2.1: Structure of the molecular semiconductors investigated in this work. **A** Pentacene thin-film phase viewed along the unit cell vector $\boldsymbol{a}$. **B** C_{70} molecule viewed along one of its short axes (top) and along its long axis (bottom). The graphics were generated using the software Mercury of the Cambridge Crystallographic Data Centre [36] and data from [35] and [37]. Carbon atoms are shown in dark grey, hydrogen atoms in light grey.

properties of both organic materials, e.g. exciton diffusion length, exciton dissociation efficiency and charge carrier mobility [28], as well as the morphology of the interface between them [29].

Due to this complexity of influential factors, experimental investigations are most promising to lead to a better understanding of individual processes if the number of affecting parameters is reduced as far as possible and pre-knowledge of the system is maximised. While solution processing enables high throughput and promises lower production costs, molecular beam deposition allows for better control over morphology and structure [27, 29, 30]. The approach of this work is to employ molecular beam deposition to develop a method to control acceptor crystallinity as well as the donor-acceptor interface area. In order to ensure broad pre-knowledge, a well-investigated material combination was chosen. Pentacene was used as donor material and the fullerene C_{70} as acceptor material. Fullerenes and pentacene have both been subjects of intensive research, and numerous studies dealing with the interaction between them have been published [31–34]. Pentacene is a hydrocarbon consisting of a linear series of five fused benzene rings. It is known to nucleate in the substrate-induced thin-film phase on many materials, including silicon dioxide (SiO_2). This is a herringbone structure consisting of layers of molecules whose long axes are only slightly tilted with respect to the surface normal [35]. FIGURE 2.1 A shows the respective unit cell from the perspective along the unit cell vector $\boldsymbol{a}$. In C_{70} the carbon atoms are arranged in a cage-like structure as in the better-known C_{60}. In contrast to the latter, C_{70} does however exhibit lower symmetry, since an additional central

ring of 10 carbon atoms gives the molecule an elongated shape, as shown in the top panel of FIGURE 2.1 B. This reduced symmetry has the advantage of higher absorption in the visible spectrum [38]. It moreover promises better control over the crystal structure, as orientational ordering effects can be exploited. A variety of different crystal structures have been reported for C_{70} crystallisation under different conditions, ranging from monoclinic to rhombohedral to cubic. An overview is provided in [39].

Starting from 2012 an increasing number of studies indicated that charge carrier separation efficiency appears to be crucially aided by delocalised charge transfer states in fullerene domains [40–42], strongly suggesting a big importance of crystallinity of the acceptor material [43]. The discussion if, and to what extent, delocalisation aids dissociation of the excitons, does not appear to have reached a clear conclusion yet [21, 22]. Calculations performed by D'Avino et al. suggest that in the nearly spherical fullerene C_{60} the electronic connectivity between molecules is not enhanced by crystallinity [44]. However an experimental investigation of the question if and how fullerene nanostructure influences charge carrier separation efficiency can still be considered a significant contribution, especially for the less symmetrical C_{70}.

2.2 METAL-HALIDE PEROVSKITES - CONFINEMENT IN NANOPOROUS LAYERS[1]

Sharing many convenient properties with organic electronics, such as the possibility of low-temperature processing of light-weight, flexible and semi-transperent devices, perovskite based electronics is a rapidly evolving field. Reaching power conversion efficiencies of up to 23.7 % [15] only 12 years after the first publication reporting a perovskite solar cell in 2006 [2], can be considered a most promising new technology for solar energy generation.

Another major research field exploiting the unique properties of this material class are metal-halide perovskite light emitters. Here, narrow band emission allows for production of devices with high colour purity [47, 48]. Emission in wide ranges of the visible spectrum can be achieved, by synthesising mixed halide perovskites. By additionally controlling size to exploite quantum effects, the remaining gaps of the spectrum can be accessed [13, 45]. The numerous state-of-the-art approaches to synthesise perovskite nanoparticles can be categorised into colloidal and template-assisted methods [49].

1 The contents of this section have been partly published in [45] and [46]. Sample preparation and photoluminescence measurements were performed by Stepan Demchyshyn, electron microscopy by Heiko Groiß and Günter Hesser. The project was conceived and supervised by Martin Kaltenbrunner and Eric Daniel Głowacki.

While the versatility of the colloidal synthesis approach has promoted a rapidly increasing number of publications on the subject [50], template-assisted growth has a crucial advantage for application in layered devices: the nanoparticles can be confined within porous thin films that can be directly used as active layers. In this context several groups have investigated how size and density - and hence optical properties - of the nanoparticles can be tuned by controlling the morphology of the porous scaffold [45, 51–53].

Members of the Linz Institute of Organic Solar Cells (LIOS) and the Department of Soft Matter Physics (SOMAP) have developed a method to produce nanocrystals of methylammonium lead trihalide ($MAPbX_3$), with chloride, bromide, and iodide (X = Cl, Br, I) and caesium lead tribromide ($CsPbBr_3$) in thin films of nanoporous anodic aluminium oxide (npAAO) , as well as in nanoporous silicon (npSi) films. By depositing precursor solution on top of the porous films, spin coating and annealing, they achieve photoluminescence (PL) that is strongly blue-shifted compared to the respective bulk material. As shown in Figure 2.2 A, the magnitude of blue shifts of the peak emission wavelength strongly depends on the compound, reaching up to 150 nm in npSi and 62 nm in npAAO for $MAPbI_3$. This strongly indicates that differently sized nanocrystals form within the pores of the two types of thin films, motivating the schematics displayed in Figure 2.2 C and D. All features presented in these schematics are based on expectations about the pore morphology based on literature combined with a transmission electron microscopy (TEM) investigation. The TEM images presented in Figure 2.2 E and F show the cross sections of a perovskite-infiltrated npAAO and npSi layer respectively. They allow for rough insights into the pore morphology, and are generally in line with the prior observations from the literature, i.e. that npAAO exhibits elongated pores that span across the film while npSi shows a rather isotropic sponge-like structure [54–56]. Dark spots in Figure 2.2 E and F correspond to perovskite and indicate partial pore filling. The precision and statistical relevance of this imaging technique are however limited. Thin lamellae of the samples have to be prepared by focused ion beam milling and subsequently scanned individually to yield a TEM image of an area of less than a square micrometre. The method is thus not suited to systematically investigating different samples with satisfactory statistical relevance. Moreover, the slices prepared by focused ion beam milling are about 100 nm thick, and respective TEM images consequently always show a projection of many pores on top of each other, inhibiting a quantitative analysis of arrangement, size, and shape of pores and perovskite crystallites. These properties are however highly relevant, since they determine the electrical and optical properties of the samples. Size and shape of the crystallites

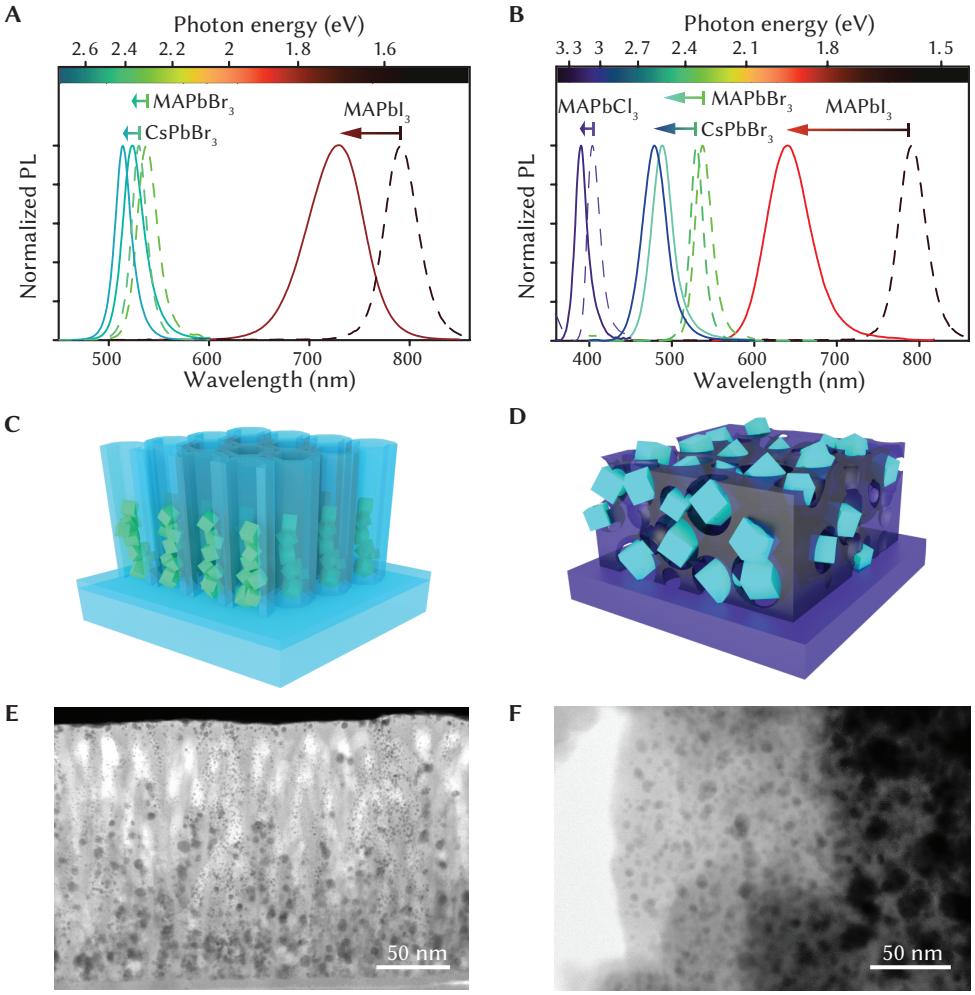

FIGURE 2.2: **A** photoluminescence (PL) from $CsPbBr_3$ (solid cyan line), $MAPbBr_3$ (solid green line) and $MAPbI_3$ (solid red line) crystallites confined in npAAO in comparison to the PL from the respective bulk material (dashed lines). For $MAPbI_3$ a maximum blue shift of 62 nm is achieved. **B** PL from $MAPbCl_3$ (solid purple line), $CsPbBr_3$ (solid blue line), $MAPbBr_3$ (solid cyan line) and $MAPbI_3$ (solid red line) crystallites confined in npSi in comparison to the PL from the respective bulk material (dashed lines). Again the largest blue shift occurs for $MAPbI_3$, here reaching 150 nm. **C - D** Schematics of perovskite-infiltrated npAAO (C) and npSi (D), designed by Stepan Demchyshyn. **E** TEM image of a 100 nm thick slice of an approximately 170 nm-high perovskite-infiltrated npAAO film. Perovskites appear dark due to diffraction and mass contrast. The aluminium oxide pores exhibit a strong anisotropy and appear to be partly filled by perovskite nanoparticles. **F** TEM image of an exfoliated flake of $MAPbI_3$-infiltrated npSi. The pore structure appears to be rather isotropic in this material. Due to a gradient in the thickness of the flake perovskite accumulations appear to be larger on the right side. Adapted from [45].

influence their emission wavelength. To implement the porous films as active layers into light-emitting diodes, charge transport across the film is required. This is expected to depend on shape and arrangement of the perovskite crystallites. Their formation is influenced by the different spatial limitations enforced by the pore morphology. Consequently, more precise knowledge about the latter is also necessary to gain cohesive understanding about the confinement method that is required to advance it. This can be achieved by a combination of different X-ray scattering techniques, which are described in the following chapter.

3

X-RAY SCATTERING

The following sections discuss how the nanostructural properties of interest stated in Chapter 2 can be accessed by X-ray scattering analysis. Due to the different requirements given by the properties of the investigated materials and the variety of questions addressed, various X-ray scattering techniques and analysis methods were applied. This chapter provides a brief review of the basic concepts that underlie the applied methods and discusses which criteria should be considered in order to exploit the advantages of each method.

3.1 QUANTIFYING IMPERFECTIONS OF A CRYSTAL

The concept of paracrystallinity developed by Hosemann [57–59] provides a suitable measure to quantify imperfections of a crystal. It is based on the effect that any deviation from an infinite ideal crystal causes broadening of the diffraction peaks. These imperfections can be categorised into noncumulative and cumulative disorder and finite size [60]. While noncumulative disorder reduces the peak intensity without affecting its shape, finite size of the crystal and cumulative disorder both result in peak broadening. In experiments they can be separated, as the peak broadening caused by the two effects shows a different dependency on the diffraction order [57–60]. This will be elucidated in the following sections.

3.1.1 *Noncumulative disorder - Debye-Waller factor*

Noncumulative disorder, i.e. random fluctuations of the lattice points around the ideal lattice positions, leads to a reduction of the peak intensity, which depends on the magnitude of the scattering vector $q = 4\pi \sin\Theta/\lambda$. Here Θ is half the scattering angle 2Θ and λ is the X-ray wavelength. The q dependency of the diffracted intensity I is given by the relation [61]

$$I \propto e^{-\langle u^2 \rangle \cdot q^2} \tag{3.1}$$

where $\langle u^2 \rangle$ is the average square displacement of the lattice points in the direction measured by the diffraction experiment. Noncumulative disorder occurs in all experiments, as thermal vibration leads to a random fluctuation

of the lattice points in any real crystal. The term on the right hand side of EQUATION 3.1 is commonly referred to as Debye temperature factor or Debye-Waller factor [61, 62].

3.1.2 *Size effects in perfectly ordered crystals - Scherrer approximation*

A simple but effective method to measure the size of a defect free small crystallite is the Scherrer analysis [63]. The diffraction peak profile from a perfect parallelepipedon crystal with N_i ($i = 1, 2, 3$) lattice planes along the three unit cell vectors $\boldsymbol{a_i}$ has the shape of a Laue function [61]:

$$I \propto \prod_{i=1}^{3} \frac{\sin^2((N_i \cdot \boldsymbol{q} \cdot \boldsymbol{a_i})/2)}{\sin^2((\boldsymbol{q} \cdot \boldsymbol{a_i})/2)} \tag{3.2}$$

Assuming a cubic crystallite with $N_1 = N_2 = N_3 = N$ and $|\boldsymbol{a_1}| = |\boldsymbol{a_2}| = |\boldsymbol{a_3}| = a$ and choosing the scattering vector parallel to one of the lattice vectors, EQUATION 3.2 simplifies to

$$I \propto \frac{\sin^2((N \cdot q \cdot a)/2)}{\sin^2((q \cdot a)/2)} \tag{3.3}$$

Approximating EQUATION 3.3 by a Gaussian (EQUATION 3.4) provides a correlation between the peak width and the crystallite size $L = N \cdot a$, as the full width at half maximum (Δq) of a Gaussian can be calculated analytically (EQUATION 3.5).

$$\frac{\sin^2((N \cdot q \cdot a)/2)}{\sin^2((q \cdot a)/2)} \approx N^2 \cdot exp\left(-\frac{1}{\pi}\left(N \cdot \frac{q \cdot a}{2}\right)^2\right) \tag{3.4}$$

$$\Rightarrow \Delta q = \frac{4\sqrt{\pi \ln 2}}{N \cdot a} = \frac{4\sqrt{\pi \ln 2}}{L} \tag{3.5}$$

Expressing the peak width in terms of q is convenient, as this parameter is suitable to display data in a wavelength independent form, allowing for easier comparability of data acquired with different setups. Historically, however, many expressions were derived in terms of the scattering angle 2Θ. Correspondingly, Paul Scherrer applied the peakwidth expressed in radians of the scattering angle, which will be named $\Delta 2\Theta$ in the following.

Using the relation $\Delta 2\Theta \approx 2\Delta q/(dq/d\Theta)$ with $dq/d\Theta = (4\pi/\lambda)\cdot\cos\Theta$ the original form of the Scherrer equation [63] is regained from EQUATION 3.5.

$$\Delta(2\Theta) = 2\cdot\sqrt{\frac{\ln 2}{\pi}}\cdot\frac{\lambda}{L}\cdot\frac{1}{\cos(2\Theta/2)} \tag{3.6}$$

In order to avoid confusion, some of the variable names used by Paul Scherrer have been altered to the modern notation used in this work.

3.1.3 *Cumulative disorder - Paracrystal theory*

EQUATION 3.5 shows, that the peak broadening caused by the finite size of a crystallite is virtually independent of the peak position. Cumulative disorder in contrast causes peak broadening that increases with the magnitude of the scattering vector q. The term cumulative disorder implies that the average fluctuation of the distance between two lattice points increases with their distance to each other. Cumulative disorder consequently reduces the long-range order [60]. Hosemann and Hindeleh quantified this disorder by the relative paracrystalline distance fluctuating g [58], which is commonly referred to as paracrystalline distortion parameter [57, 59]:

$$g_{hkl} = \sqrt{\langle d_{hkl}^2\rangle / \langle d_{hkl}\rangle^2 - 1} \tag{3.7}$$

Here, h,k,l are the Miller indices, describing the direction in the crystal, $\langle d_{hkl}\rangle$ is the average of all lattice plane spacings occurring in the corresponding direction and g_{hkl} is the associated paracrystalline distortion parameter.

Hosemann and Hindeleh showed that the integral breadth δb_{hkl} of the diffraction peaks is correlated to their diffraction order n by the following relation

$$\delta b_{hkl} = \frac{1}{\langle d_{hkl}\rangle}\cdot\left(\frac{1}{\langle N_{hkl}\rangle} + (\pi g_{hkl})^2\cdot n^2\right) \tag{3.8}$$

where $\langle N_{hkl}\rangle$ is the average number of lattice planes in the respective direction [64]. By plotting the integral breadths against the squared diffraction order the average crystallite size $\langle L_{hkl}\rangle = \langle d_{hkl}\rangle\cdot\langle N_{hkl}\rangle$ and the paracrystalline distortion parameter g_{hkl} can easily be extracted from a linear fit. This constitutes a straight forward method to quantify imperfections in crystals. A more detailed and illustrative description of the concept of paracrystallinity can be read in [57].

3.1.4 *Advantages and limitations*

The paracrystal method is a powerful tool to handle data from samples where finite size is not the only cause for peak broadening. It does however impose high requirements on the signal to noise ratio of the diffraction data as at least three well resolved diffraction orders from the same set of lattice planes are required to allow for the linear fit of their peak widths.

For samples in which finite size is the major contribution to peak broadening the Scherrer equation yields a good approximation of the crystallite size. It can be applied even if only a single diffraction order is available. Another major advantage of the Scherrer approximation is its robustness: For experiments performed on an instrument with a high energy resolution the relative standard error of the extracted crystallite size can well be approximated by the relative uncertainty of the peak width determination. The Scherrer approximation can thus be applied to powder diffraction data of small crystallites, where diffractions from different planes usually overlap if non-cubic structures are investigated. The simplicity of the method moreover allows for easy batch analysis.

3.2 ANALYSING AMORPHOUS MATTER - SMALL-ANGLE X-RAY SCATTERING

The analysis methods presented so far depend on diffraction form ordered matter and can thus not be applied to amorphous materials. Small-angle X-ray scattering (SAXS) provides a powerful tool to investigate size and shape of particles, independently of their atomic order.

3.2.1 *Basic principles of small-angle X-ray scattering*

The scattered intensity $I(\boldsymbol{q})$ of N identical isolated particles with homogenous scattering length density ρ is given by

$$I(\boldsymbol{q}) = N \cdot \Delta\rho^2 \cdot |\int_V e^{i\boldsymbol{q}\cdot\boldsymbol{r}} dV|^2 \tag{3.9}$$

where $\boldsymbol{q}$ is the scattering vector, $\Delta\rho$ is the scattering length density contrast between particle and its environment and V is the volume of the particle.

This can also be expressed as

$$I(\boldsymbol{q}) = N \cdot \Delta\rho^2 \cdot V^2 \cdot |F(\boldsymbol{q})|^2 \tag{3.10}$$

where $|F(\boldsymbol{q})|^2 = 1/V^2 \cdot |\int_V e^{i\boldsymbol{q}\cdot\boldsymbol{r}} dV|^2$ is called the form factor. It depends on the size and shape of the particles and can be calculated analytically for simple shapes. Integration in spherical coordinates up to the radius R yields the form factor of monodisperse spherical particles with a homogenous scattering length density [65]:

$$|F_{sphere}(q)| = 3 \cdot \left(\frac{\sin(qR) - qR\cos(qR)}{(qR)^3} \right) \tag{3.11}$$

Analogously, the form factor of a cylinder with the radius R and the length L can be calculated by integration in cylindric coordinates. Here the result depends on the angle α between the scattering vector $\boldsymbol{q}$ and the cylinder axis [66]:

$$|F_{cylinder}(q,\alpha)| = \left(\frac{2 \cdot \sin(q \cdot \cos\alpha \cdot L/2)}{q \cdot \cos\alpha \cdot L/2} \right) \cdot \left(\frac{J_1(q \cdot \sin\alpha \cdot R)}{q \cdot \sin\alpha \cdot R} \right) \tag{3.12}$$

J_1 is the first order Bessel function of the first kind.

A summary of more analytical expressions of form factors is found in [67].

For all shapes polydispersity can be accounted for by integrating over the probability distribution of particle sizes $p(R)$ [65]:

$$I(\boldsymbol{q}) = \Delta\rho^2 \int_0^\infty p(R) \cdot V(R)^2 \cdot |F(\boldsymbol{q}, R)|^2 dR \tag{3.13}$$

If particles in solution are investigated the concentration can be adjusted in a way that the distance between individual particles is large enough to prevent interference effects and only the form factor is observed. In solid samples, as e.g. porous films, in contrast, the arrangement of the particles (or pores) will inevitably affect the scattered intensity if the distances between them are of comparable size as the particles. The scattered intensity then results in [65, 68]

$$I(\boldsymbol{q}) = N \cdot \Delta\rho^2 \cdot V^2 \cdot |F(\boldsymbol{q})|^2 \cdot S(q) \tag{3.14}$$

$S(q)$ is called the structure factor. It is related to the pair correlation function $g(r)$, i.e. the probability distribution function of the distances r between the particles, via the relation

$$S(q) = 1 + 4\pi\rho_n \int (g(r) - 1) \frac{\sin(qr)}{qr} r^2 dr \tag{3.15}$$

where ρ_n is the number density [69]. A completely arbitrary arrangement of particles would result in $g(r) = 1$ for all r and consequently in $S(q) = 1$ for all q-values. For highly ordered nanoparticles as e.g. processable with DNA-origami, $S(q)$ can exhibit sharp peaks at small scattering angles [70]. $S(q)$ always approaches 1 for very large q.

3.2.2 *Advantages and limitations*

SAXS is a versatile method that can provide detailed information about the morphology of a sample: Shape, size distribution and arrangement of particles can be extracted from one measurement. It does however require considerable prior knowledge of the sample morphology to ensure reliable results. Only if a realistic model and boundary conditions can be found in advance, the fit of the data will correlate to the actual properties of the sample. For sufficiently simple sample structures this information can usually be provided by a pre-characterisation using imaging techniques.

3.3 EXPERIMENTAL CONSIDERATIONS - DATA COLLECTION

3.3.1 *Choice of experimental method*

The choice of the scattering geometry strongly depends on the addressed question and the properties of the investigated material. This section focusses on synchrotron experiments, but most of the general considerations are applicable to in-house setups, too. The main difference is, that X-ray tube based in-house setups are limited to the characteristic energy given by the anode material and generally provide orders of magnitude lower flux. The latter results in considerably lower signal to noise ratio and involves longer exposure times.

If high q-resolution and signal to noise ratio are the main requirements **X-ray reflectivity measurements** are usually the method of choice. Here the specular intensity is measured by varying the incident angel ω and measuring the intensity at the scattering angle $2\theta = 2 \cdot \omega$. Outstanding q-resolution can be achieved for all scattering angles, by collimating the radiation incident on the detector by two sets of slits that are axially shifted to each other and scanning with a small angular step width. Thus, X-ray reflectivity was chosen to acquire the data for a paracrystal analysis of the C_{70} films. Due to the high resolution of this experiment, changes of the out-of-plane lattice spacing in the order of $1 \times 10^{-2}\,\text{Å}^{-1}$ could be observed. The collimation on the detector moreover strongly reduces the noise caused by e.g. cosmic background, which makes the method a powerful tool at in-house setups

with low flux. A major drawback of the method is that data acquisition is slow, as hundreds of exposures are required to perform a high resolution scan that contains several diffraction orders.

For purposes that do not crucially depend on excellent resolution, methods that require a single exposure of a linear or area detector are often preferred, especially at synchrotron sources, where beamtime is particularly valuable and high flux ensures superior signal to noise ratio. By this means the overall measurement time can be reduced by one to two orders of magnitude compared to a large q-range high resolution reflectivity measurement at the same source. The major limitation of X-ray reflectivity measurements is, that they solely provide out-of-plane information. With the exception of samples with isotropic crystallite orientation, additional techniques are required to clarify the crystal structure.

To investigate the three-dimensional structure of polycrystalline pentacene-C_{70} bilayers, **grazing-incidence wide-angle X-ray scattering** (GIWAXS) was employed in this study. There are two main reasons for this choice. First, the method provides the required information about the crystal structure as well as its orientation along the surface normal. Second, the grazing-incidence geometry enhances the signal from the surface and near-surface layers. In this study it thus provided strong enough signal of the C_{70} top layers to show several diffraction peaks, despite of their high level of disorder. To optimise the sensitivity of the measurement to the layer of interest the penetration length l can be adjusted by choosing wavelength λ and angle of incidence α_i [71].

$$l = \lambda/(2\pi(\alpha_c^2 - \alpha_i^2)^{1/2}) \tag{3.16}$$

Here, α_c is the critical angle for total external reflection. Due to the small angle of incidence α_i the projection l_b of the vertical beam size h_b onto the plane of the sample surface becomes very long. In most setups this so called footprint of the beam will cover the entire sample length as $l_b = h_b / \sin\alpha_i$ can easily range to decimetres. This has the advantage, that the method averages over large sample areas and thus provides data of high statistical relevance. It is however associated with a considerable loss of flux, that is more severe for shorter samples. On the other hand the instrumental broadening in out-of-plane direction increases with the footprint and thus with sample length. Consequently, the sample length should be optimised to yield a compromise between signal strength and resolution that meets the requirements imposed by the aim of the experiment.

When an area detector is employed the method provides data of a wide two-dimensional (2d) q-range in one X-ray exposure. To each detector pixel an in-plane component $q_{\parallel}$ and out-of-plane component $q_{\perp}$ of the scattering vector can be assigned, according to the orientation of the sample. In these coordinates the diffraction pattern can easily be compared to calculated peak positions for any structure and orientation. An outline of the respective calculations is found in Section 3.3.3. Limited only by the size of beam stop and detector, data is available almost for the entire $q_{\parallel}$-$q_{\perp}$ plane, leaving only a small area around $q_{\parallel} = 0$ inaccessible. Thus, GIWAXS and X-ray reflectivity are complementary techniques, that if combined provide comprehensive information about the structure of oriented samples.

For very small crystallites it is challenging to acquire sufficiently strong signal for a diffraction based size analysis. For the disconnected C_{70} nanoaggregates investigated in this thesis it could neither be accomplished by GIWAXS nor X-ray reflectivity measurements. This can be ascribed to the low amounts of weakly scattering organic material in combination with strong peak broadening caused by disorder and finite size. In such cases, as well as for amorphous particles, **small-angle X-ray scattering** can provide information about the morphology of the sample. Here again, the **grazing-incidence geometry** was employed, to exploit the advantage of high surface sensitivity. Like its wide-angle counterpart this method provides information about structures within the plane of the sample surface, as well as perpendicular to it. The data can be transferred to q-space following the same procedure as for GIWAXS (see Section 3.3.3). Simulating the scattered intensity in 2d is however complex since dynamic effects at shallow angles need to be considered, making a treatment in the distorted-wave Born approximation necessary [72]. Pure in-plane information can be accessed by evaluating horizontal cuts along a constant $q_{\perp}$ value, substantially simplifying the analysis [73, 74]. For very small incidence angles the inaccessible q-range around $q_{\parallel} = 0$ is so narrow that it is often not resolved at the low $q_{\perp}$-values of interest. As also for transmission SAXS the beam stop is thus usually the main factor limiting the minimum accessible q-value.

For the investigation of micrometre thick porous films a statistically relevant representation of the morphology of the entire film thickness is required, making **SAXS in transmission geometry** the method of choice. As anisotropies within the plane of the sample surface are rare, data can usually be reduced to 1d by azimuthal integration. This improves the signal to noise ratio and significantly simplifies data treatment. The data can then be fitted according

to the principles described in SECTION 3.2.

While small-angels scattering techniques have the unique advantage that they can be applied to any material independently of its structure, in some cases they need to be complemented by diffraction techniques to provide a complete picture of the sample. This is especially the case for complicated sample morphologies, as SAXS data interpretation is often ambiguous if the investigated system requires many fit parameters [75]. Investigating size and shape of pores as well as of perovskite crystallites confined within them was only possible by combining small- and wide-angle methods. While transmission SAXS experiments provided insights into the morphology or empty pores, the interpretation of such measurements on perovskite filled pores would be prevented by the interaction of the signal from pores and crystallites. This problem can be overcome by investigating the diffraction signal of the crystallites, as this occurs in the wide-angle range, clearly separated from the small angle scattering features arising from the pores. Gaining a sufficiently high signal to noise ratio to allow for an anisotropy sensitive peak broadening analysis of micrometre thin porous films that are only partially filled with nanocrystallites is however not trivial. Typical transmission experiments neither promise strong signal nor are they appropriate to investigate orientational effects. Grazing incidence geometry would, on the other hand, be biased towards surface properties that are likely to differ from the rest of the layer.

A suitable solution is the use of **high-energy microbeam diffraction**. Due to penetration depths on the order of centimetres for X-ray energies of $\sim$100 keV (see SECTION 3.3.2), films can be probed with the beam parallel to the surface. The microfocus ensures that the flux of the instrument is effectively used. It moreover opens up the option to probe for heterogeneities with depth, if the vertical beam width is smaller than the film thickness. As a result, effects occurring on the surface of a sample can be separated from the main properties of the film. The use of high-energy X-rays brings some characteristic attributes along, such as special requirements on source and detectors, as well as differences of the material dependent probabilities of photoelectric absorption and scattering processes. In the following sections these characteristics will be summarised. The choice of photon wavelength depending on the material of interest will be discussed, as well as further applications of high-energy diffraction and the q-resolution of high-energy experiments.

3.3.2 *High-energy X-ray diffraction*

3.3.2.1 *Sources and detectors*

Sources of high-energy X-ray radiation are radioactive γ-emitters, high-energy X-ray tubes and synchrotron sources. Radioactive sources emit characteristic radiation but require to be treated with caution. Continuous high-energy radiation can be obtained from high-energy X-ray tubes. The generation of hard X-rays of high brilliance however requires a third generation synchrotron source [76]. Highly requested European beamlines that are optimised for high X-ray energies are ID31 at ESRF (Grenoble, France) and P07 at DESY (Hamburg, Germany). The undulator based beamlines ID15 (ESRF) and P21 (DESY) and the wiggler based beamline I12 at the Diamond (Oxfordshire, United Kingdom) also offer energies of 100 keV and above [77–79]. The nth harmonic wavelength λ_n emitted in forward direction by an undulator is of the form

$$\lambda_n = \frac{\lambda_u}{2n\gamma^2}\left(1 + \frac{1}{2}\left(\frac{e}{mc2\pi}\right)^2 \lambda_u^2 B_0^2\right) \tag{3.17}$$

where λ_u is the spatial period of the undulator, $\gamma = 1/\sqrt{1 - v^2/c^2}$ with the electron velocity v and the speed of light c is the Lorentz factor of the electron, e and m are the electron charge and rest mass, and B_0^2 is the maximum magnetic field in the undulator [65, 80]. High X-ray energies are therefore more easily accessible at storage rings that operate at high particle energies and undulators optimised for the generation of high-energy radiation have shorter spatial periods than standard. At ID31 (ESRF) e.g. a period of 14.5 mm is used [81], at P07 (DESY) the installation of an 19 mm undulator is planned for spring 2019 [82]. Both storage rings operate at 6 GeV [83, 84].

As high-energy X-ray diffraction at high fluxes is a rather young field the majority of 2d detectors available for diffraction applications is optimised for lower X-ray energies [85]. Amorphous silicon flat-panel detectors with CsI scintillator layers originally designed for medical applications are however rather well suited for the requirements [85, 86]. They are optimised for an X-ray energy of ∼80 keV and offer short read out times, low spatial distortion and wide dynamic ranges [85].

3.3.2.2 *Photon matter interaction - implications on the choice of energy*

The main reason for the low efficiency of direct solid state detectors at high energies is the associated lower photon absorption. While presenting a challenge for photon detection, low photoelectric absorption within the sample is highly beneficial for any scattering experiment. For the experiments per-

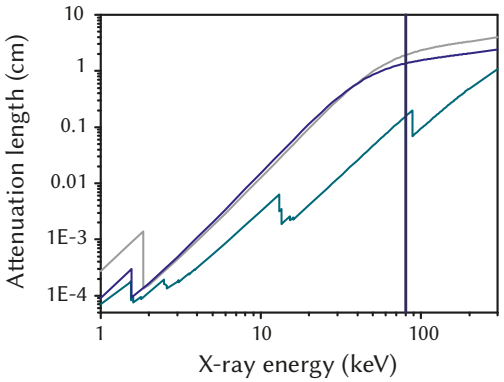

FIGURE 3.1: X-ray energy dependency of the attenuation length of Si (grey), Al_2O_3 (blue) and $MAPbBr_3$ (cyan). With the exceptions of the Si and Al K absorption edges the attenuation length in Si and Al_2O_3 increases monotonously with the X-ray energy. It rises up to 1.9 cm and 1.4 cm, respectively, at 80 keV, as marked by the vertical line. An increase of the attenuation length with the X-ray energy is the general trend in $MAPbBr_3$, too, while here absorption edges of the contained heavy elements occure up to high energies, and attenuation is generally much stronger. The curves were calculated based on data provided by the National Institute of Standards and Technology [87].

formed on perovskite-infiltrated porous thin films presented in this thesis the lower photoelectric absorption for higher energies was of two-fold importance. On the one hand it was a prerequisite for the employed geometry and the resultant suitability to detect anisotropic structures and exploit the enhancement of the scattering signal due to large sample lengths. On the other hand it significantly reduced radiation damage, as will be discussed further below. The first aspect becomes evident in FIGURE 3.1 showing the attenuation length in Si (grey), Al_2O_3 (blue) and $MAPbBr_3$ (cyan) plotted against the X-ray energy. The curves have been calculated based on the total attenuation cross sections listed in the NIST (National Institute of Standards and Technology) Standard Reference Database 8 (XGAM) [87]. At an X-ray energy of 20 keV the attenuation length in Si and Al_2O_3 is only about 1 mm. At 80 keV (marked by a vertical line) it has increased to 1.9 cm in Si and to 1.4 cm in Al_2O_3, thus allowing to measure in transmission with the beam parallel to the surface of many millimetres long films. Choosing an X-ray energy below the Pb K absorption edge at 88 keV has the advantage over somewhat higher energies that an attenuation length of up to 2 mm can be achieved in $MAPbBr_3$, which is otherwise only possible for energies of 130 keV and above. As the perovskite density in the samples is expected to be only of a few percent this is of limited importance for the accessible sample length. The main contribution to the total attenuation in the perovskite is however photoelectric absorption and consequently the choice of energy is crucially important to prevent radiation damage.

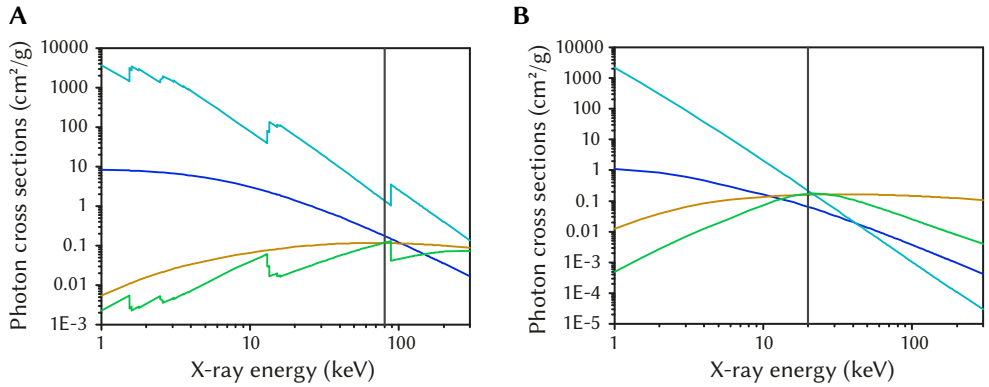

FIGURE 3.2: Energy dependence of the photon cross sections of photoelectric absorption (cyan), coherent scattering (blue) and incoherent scattering (orange) in **A** $MAPbBr_3$ and **B** carbon. The green curve corresponds to the ratio between the coherent scattering cross section and the sum of the ones of incoherent scattering and photoelectric absorption. Choosing an X-ray energy close to the maximum of this curve can be considered a reasonable compromise between signal strength and radiation damage. X-ray energies chosen for the experiments on the respective materials presented in this thesis are marked by vertical lines. The plots are based on data provided by the National Institute of Standards and Technology [87].

FIGURE 3.2 A illustrates how the photon cross sections of photoelectric absorption σ_{abs} (cyan), coherent scattering σ_{coh} (blue) and incoherent scattering σ_{incoh} (orange) vary with the X-ray energy in $MAPbBr_3$. Due to the high atomic number Z of elements contained in the investigated perovskites ($Z_{Pb} = 82$, $Z_{Cs} = 55$, $Z_I = 53$, $Z_{Br} = 35$) they are generally subject to significant photoelectric absorption, even at high energies. The scattering cross sections are however also increased compared to lighter elements and the relative drop of the cross section of coherent scattering associated with increased X-ray energy is thus acceptable to prevent radiation damage. This consideration is illustrated by the green curve in FIGURE 3.2 A which represents the ratio between the coherent scattering cross section and the sum of the ones of incoherent scattering and photoelectric absorption, i.e. $\sigma_{coh}/(\sigma_{incoh} + \sigma_{abs})$. Its maximum value of 0.13 occurs at 88 keV.

In the molecular crystals investigated in this work, carbon is the element that interacts the strongest with X-rays. The respective photon cross sections are shown in FIGURE 3.2 B. Again cyan corresponds to photoelectric absorption, blue to coherent and orange to incoherent scattering. As the cross section of coherent scattering is about one order of magnitude lower than for the perovskite, the loss of choosing a high energy would be more severe in this case. This is however not required, since the photoelectric absorption cross section of carbon decreases rapidly with the X-ray energy, falling below $1\,cm^2/g$ at an energy as low as 13 keV. For carbon the ratio between the coherent scattering cross section and the sum of the ones of incoherent scattering and

photoelectric absorption ($\sigma_{coh}/(\sigma_{incoh}+\sigma_{abs})$, green curve) has its maximum at 22 keV, i.e. at much lower X-ray energy than the perovskite. Choosing an X-ray energy of 20 keV, as marked by a vertical line, can thus be considered a good compromise between radiation damage and signal to noise ratio.

3.3.2.3 *Further applications of high-energy X-ray diffraction*

Diffraction occurs at smaller angles when high X-ray energies are used, as the sine of half the scattering vector scales with the X-ray wavelength: $\sin(2\theta/2) = (q \cdot \lambda)/(4\pi)$. This is beneficial if large q-ranges need to be covered by an experiment. For an X-ray wavelength of $\lambda = 1\,\text{Å}$ the maximum theoretically accessible momentum transfer is $q = 4\pi/\lambda = 12.6\,\text{Å}^{-1}$, as restricted by the geometrical limitations. For an X-ray wavelength of $\lambda = 0.1\,\text{Å}$ it is one order of magnitude larger. Accessing a large q-range is of special importance in total scattering measurements. The goal of these measurements is to record the entire intensity pattern consisting of diffuse scattering and in case of ordered matter additional Bragg peaks. By Fourier transforming the signal, the reduced pair distribution function is acquired, which is then analysed in real space [88, 89]. Being the upper integration limit of the Fourier transform the maximum measured q-value determines the real space resolution [88]. As 2d detectors can in practice cover a scattering angle range up to 60° at maximum [88], a fast acquisition of the required data range requires high-energy X-rays of high flux [90].

Another important application of high-energy X-ray radiation is the analysis of diffuse scattering in the proximity of Bragg reflections. High X-ray energies result in low curvatures of the Ewald sphere. Consequently an area detector cuts through the reciprocal lattice in close proximity to many Bragg reflexes [91]. Diffuse scattering is thus captured on the detector and can be analysed to investigate lattice vibrations or crystal defects. High-energy surface X-ray diffraction is another method that makes use of the low curvature of the Ewald sphere. Most commonly performed in grazing-incidence geometry truncation rods or nanocrystal facet diffraction signals are captured on a 2d detector representing an almost planar and vertical surface in reciprocal space [92, 93]. For single crystalline samples a vast number of diffraction features can be recorded by rotating the crystal, while samples with imperfections as mosaicity provide a wide range of diffraction signals even in stationary geometry, making time resolved measurements possible [93]. In 2017, Reikowski et al. presented similar measurements in transmission geometry allowing them to directly visualise the symmetry of surface lattices. As the detector represents a part of the Ewald sphere that is almost parallel to the interface the truncation rods intersect it [94]. By employing a microbeam,

the geometry even enables lateral mapping of the surface properties of heterogeneous materials. In the data of nanoporous Si films presented in this thesis the low Ewald sphere curvature results in the observation of broadened Si peaks extending into the reciprocal space region covered by the detector. These were exploited to qualitatively measure the porosity-evolution of the films, by quantifying the associated Si peak broadening caused by finite pore wall thickness.

3.3.2.4 *Q-resolution of high-energy X-ray diffraction experiments*

In the following the q-resolution of high-energy X-ray diffraction experiments will be discussed on the example of a microdiffraction setup at P07, DESY with an X-ray energy of 80 keV and a sample to detector distance of 2 m. The most influential factor determining the angular peak broadening in high-energy experiments is usually the energy resolution $\Delta E/E$ of typically 2-3 $\times 10^{-3}$ [93, 95]. In FIGURE 3.3 the respective q-resolution is plotted in green against the magnitude of the scattering vector for $\Delta E/E = 2.5 \times 10^{-3}$. Due to the large attenuation lengths associated with high X-ray energies, the length of the penetration path of the beam within the sample l_p can however be chosen so large that its effect on the resolution surpasses the influence of the energy bandwidth by far. The blue curve in FIGURE 3.3 shows the line broadening resulting from a sample length of $l_p = 4$ mm calculated for the setup parameters mentioned above. As shown in FIGURE 3.1 the attenuation length in Si and Al_2O_3 would allow for sample lengths of over 10 mm, which would cause a much steeper increase of the line broadening. While typically in the order of 1×10^{-4} Å^{-1} in collimation mode (e.g. $2-10 \times 10^{-6}$ rad divergance at P07, DESY [95]), beam divergence can have a considerable effect on the resolution at low q if a microbeam is employed. The red line in FIGURE 3.3 shows as an example the line broadening resulting from the divergence caused by focussing the X-ray beam from an width of 0.3 mm at the position of the lenses down to 2 µm at the sample 4410 mm further down the beam. As typical pixel sizes in detectors suitable for high-energy applications range between 0.15-0.4 mm [85, 86] and high energies result in small scattering angles, the effect of divergence is however only relevant if large sample to detector distances are applied. The black line in FIGURE 3.3 representing the best achievable resolution for a pixel size of 0.2 mm and a sample to detector distance of 2 m at 80 keV shows that even at this sample to detector distance pixel size is the limiting factor at small angles. In microfocus experiments the effect of the beamsize onto the q-resolution is always neglectable compared to the effect of divergence. In FIGURE 3.3 the in-plane line broadening caused by a horizontal beam width of 30 µm is plotted in cyan for the parameters mentioned above. A vertical beam width

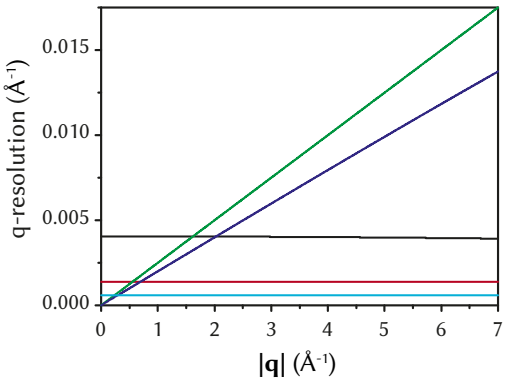

FIGURE 3.3: The different contributions defining the q-resolution calculated for the example of a high-energy microbeam experiment performed at 80 keV with an sample to detector distance of 2 m: broadening due to a energy bandwidth of $\Delta E/E = 2.5 \times 10^{-3}$ (green), sample length of 4 mm (blue), beam divergence of 0.002° (red), detector pixel size of 0.2 mm (black) and horizontal beam size of 30 µm (cyan).

of 2 µm causes an out-of-plane line broadening of 4×10^{-5} Å^{-1}, which is too small to be observed in FIGURE 3.3.

3.3.3 *Data processing*

Reflectivity measurements provide pure out-of-plane signal, that can be transferred to q-space following the simple relation

$$q = |\boldsymbol{q}| = \frac{4\pi}{\lambda} \cdot \sin(2\Theta/2) \tag{3.18}$$

with the wavelength λ and the scattering angle 2Θ.

For powder diffraction and transmission SAXS measurements the data can be averaged azimuthally and then be translated to q using the same relation.

For grazing incidence measurements, the scattered intensity can be split up in an in-plane $q_{\parallel}$ and an out-of-plane component $q_{\perp}$ of the scattering vector $\boldsymbol{q}$ when being transferred to q-space. When an area detector is placed perpendicular to the direct beam this can most easily be performed by geometrical considerations in the laboratory coordinate system, choosing the incident wave vector $\boldsymbol{k_i}$ along the x-axis.

$$\boldsymbol{k_i} = \frac{2\pi}{\lambda} \begin{pmatrix} 1 \\ 0 \\ 0 \end{pmatrix} \tag{3.19}$$

The scattered wave vector $\boldsymbol{k}_f$ can be described as

$$\boldsymbol{k}_f = \frac{2\pi}{\lambda} \cdot \frac{1}{\sqrt{1 + \tan^2\varphi_\parallel + \tan^2\varphi_\perp}} \begin{pmatrix} 1 \\ \tan\varphi_\parallel \\ \tan\varphi_\perp \end{pmatrix} \tag{3.20}$$

Here, the horizontal and the vertical detector angle $\varphi_\parallel = \arctan(d_\parallel / d_{sd})$ and $\varphi_\perp = \arctan(d_\perp / d_{sd})$ have been introduced. Here $d_\parallel$ is the horizontal distance of the respective detector pixel from the incident beam position, d_{sd} is the sample to detector distance and $d_\perp$ is the vertical distance of the respective detector pixel from the incident beam position.

For an incidence angle ω the sample normal $\boldsymbol{n}$ is

$$\boldsymbol{n} = R_y(-\omega) \begin{pmatrix} 0 \\ 0 \\ 1 \end{pmatrix} = \begin{pmatrix} -\sin\omega \\ 0 \\ \cos\omega \end{pmatrix} \tag{3.21}$$

where the rotation matrix $R_y(-\omega)$ for a backward rotation around the y-axis has been used. The projection of the scattering vector $\boldsymbol{q} = \boldsymbol{k}_f - \boldsymbol{k}_i$ onto $\boldsymbol{n}$ yields the out-of-plane component $q_\perp$. Introducing $\Sigma = \sqrt{1 + \tan^2\varphi_\parallel + \tan^2\varphi_\perp}$ results in

$$q_\perp = \boldsymbol{q} \cdot \boldsymbol{n} = \frac{2\pi}{\lambda} \left[\sin\omega \left(1 - \frac{1}{\Sigma} \right) + \frac{\cos\omega \cdot \tan\varphi_\perp}{\Sigma} \right] \tag{3.22}$$

The in-plane component is then given by

$$\begin{aligned} q_\parallel &= |\boldsymbol{q} - q_\perp \cdot \boldsymbol{n}| \\ &= \frac{2\pi}{\lambda \cdot \Sigma} \cdot [(1 - \Sigma + \sin^2\omega(\Sigma - 1) + \sin\omega\cos\omega\tan\varphi_\perp)^2 + \tan^2\varphi_\parallel \\ &\qquad + (\tan\varphi_\perp - \sin\omega\cos\omega(\Sigma - 1) - \cos^2\omega\tan\varphi_\perp)]^{1/2} \end{aligned} \tag{3.23}$$

Expected peak positions can be calculated for different structures and compared to the observed diffraction pattern in q-space. From the unit cell vectors $\boldsymbol{a}$, $\boldsymbol{b}$ and $\boldsymbol{c}$ of a given structure the reciprocal lattice with its vectors $\boldsymbol{a}^*$, $\boldsymbol{b}^*$ and $\boldsymbol{c}^*$ can be calculated following textbook knowledge [96, 97]. Constructive interference occurs for

$$\boldsymbol{q} = \boldsymbol{G} = h \cdot \boldsymbol{a}^* + k \cdot \boldsymbol{b}^* + h \cdot \boldsymbol{c}^* \tag{3.24}$$

where h, k, l are the Miller indices [61]. This can be split up in an in-plane and an out-of-plane component as described above, while $\boldsymbol{n}$ now represents the

direction in the lattice that is assumed to be parallel to the surface normal. A more detailed description of these calculations is found in [98].

Part II

SAMPLE PREPARATION AND EXPERIMENTAL METHODS

4

SAMPLE PREPARATION

4.1 PREPARATION OF PENTACENE-C_{70} HETEROSTRUCTURES

Si substrates with a 300 nm thick thermal SiO_2 layer were sonicated in acetone, isopropanol and deionised water for 10 min each and dried in a N_2 stream. 20 nm of pentacene (triple sublimed, Sigma-Aldrich) were deposited by molecular beam deposition onto the unheated substrates at a rate of 0.09 Å/s. The base pressure was 2×10^{-7} mbar. Subsequently C_{70} (double sublimed, Crea-Phys) was deposited at different sample temperatures and rates. Prior to each deposition process a base pressure in the order of 10^{-7} mbar was achieved. For each combination of deposition temperature and rate C_{70} was deposited onto two samples in the same process. After heating both samples to the desired temperature, an adjustable shadow mask was used to deposit a 20 nm thick film on one of them and a nominal thickness of 8 Å on the other one. Deposition rates between 0.04 Å/s and 0.19 Å/s and sample temperatures between 25 °C and 140 °C were chosen. The sample temperature was measured by a PT100 sensor. The rate was determined using a quartz microbalance that was mounted in about 3 cm distance of the centre of the sample holder. To improve comparability of the data, all C_{70} layers that were used to investigate the effect of the C_{70}-deposition temperature were deposited onto pentacene films from the same pentacene deposition process.

4.2 PREPARATION OF PEROVSKITE NANOCRYSTALS IN POROUS THIN FILMS

All sample preparation steps summarised in this section were performed by Stepan Demchyshyn at the Johannes Kepler University (JKU) Linz. A more detailed description of the procedures has been published in [45] and [46].

4.2.1 *Nanoporous silicon*

Boron-doped p-type silicon wafer pieces with $R_0 = 8 - 20\,\Omega \cdot \mathrm{cm}$, a thickness of 0.5 mm and $\langle 100 \rangle$ orientation were sonicated in Hellmanex III (2 vol% in deionised water), deionised water, acetone, and isopropanol for 20 min each. Subsequently the RCA (Radio Corporation of America) standard cleaning steps were performed. 250 nm thick Al contacts were evaporated onto

the alkaline-etched backsides of the samples. After being annealed in N_2 atmosphere at 450 °C for 20 min the samples were anodised for 20 min in galvanostatic mode at different current densities between 5 and 20 $mAcm^{-2}$ using the standard etch cell defined by Sailor [56]. A 1:1 mixture of 48 % HF and absolute ethanol was used as electrolyte. The samples were subsequently washed with absolute ethanol, dried with N_2 and treated with O_2 plasma at 50 W for 5 min to improve wetting of the perovskite precursor solutions.

4.2.2 *Nanoporous aluminium oxide*

The nanoporous aluminium oxide films investigated with small-angle X-ray scattering were prepared on glass substrates. The samples investigated by high-energy X-ray microbeam diffraction were fabricated on Si wafer pieces with a 120 nm thick thermal SiO_2 layer. All substrates were sonicated in Hellmanex, deionised water, isopropanol, and acetone for 20 min each and dried in a N_2 stream. 1.0 µm to 1.2 µm thick layers of Al were thermally evaporated onto the samples. The samples were anodised for 60 min in 0.2 M oxalic acid electrolyte under potentiostatic conditions at 5 V. Subsequently they were washed with dionised water, dried and treated with O_2 plasma at 50 W for 5 min.

4.2.3 *Infiltration with perovskite precursor solutions*

The precursor solution for $MAPbI_3$ was prepared by mixing 922 mg of lead(II) iodide (PbI_2), 334 mg of methylammonium iodide and 2.25 ml of dimethylformamide (DMF). For $MAPbBr_3$ 368 mg of lead(II) bromide ($PbBr_2$), 124 mg of methylammonium bromide and 1.10 ml of DMF were mixed and stirred overnight at 50 °C. For $CsPbBr_3$ 367 mg of $PbBr_2$, 215 mg of caesium bromide and 2.40 ml of dimethylsulfoxide were mixed and stirred overnight at 70 °C. The precursor solutions were deposited onto the nanoporous thin films by spin-coating at 2400 rpm for 7 s. Subsequently silicon and aluminium oxide samples were annealed for 30 and 20 min, respectively, at 115 °C in ambient atmosphere.

5

CHARACTERISATION METHODS[1]

5.1 IMAGING AND OPTICAL CHARACTERISATION

Atomic force microscopy (AFM) and transmission electron microscopy (TEM) were used to pre-characterise the samples and aid interpretation of scattering data. AFM was performed in tapping mode using a Veeco Dimension3100 AFM, which is part of the clean room equipment of the Chair of Solid State Physics at Ludwig-Maximilians University (LMU) Munich. Images were processed and analysed with the WSxM software (Nanotec) [99]. TEM images were acquired by Heiko Groiß and Günter Hesser at JKU Linz using a JEOL JEM-2200FS TEM operated in scanning mode at 200 kV. Photoluminescence measurements were performed by Stepan Demchyshyn at JKU Linz, using a photomultiplier tube-equipped double-grating input and output fluorometer (Photon Technology International).

5.2 STRUCTURAL INVESTIGATION BY X-RAY SCATTERING

All X-ray experiments described in this section were performed at beamlines P07 and P08 of the PETRA III storage ring at DESY (Deutsches Elektronen-Synchrotron). X-ray reflectivity (Section 5.2.1), grazing-incidence wide-angle X-ray scattering (GIWAXS, Section 5.2.2) and grazing-incidence small-angle X-ray scattering (GISAXS, Section 5.2.3) of pentacene-C_{70} samples were measured in collimation mode at the high resolution diffraction beamline P08. Here, the X-ray beam had an energy of 20 keV with a bandwidth of 1×10^{-5}, a vertical and horizontal beam width of 0.3 mm and 0.7 mm respectively and a vertical and horizontal divergence of 2×10^{-6} rad and 1×10^{-5} rad, respectively. This led to a transversal vertical coherence length of 3.1 µm, a transversal horizontal coherence length of 15.5 µm and a longitudinal coherence length of 3.1 µm. Perovskite-infiltrated nanoporous layers were investigated by high-energy X-ray microbeam diffraction performed at P07 (Section 5.2.4), the empty porous layers were characterised by transmission SAXS under normal incidence at P08 (Section 5.2.5).

1 Parts of the characterisation methods described in this chapter have been published in references [45] and [46].

5.2.1 *X-ray reflectivity*

5.2.1.1 *Setup*

Reflectivity data were recorded using a Mythen 1k (Dectris, Switzerland) detector that was mounted on a vacuum tube equipped detector arm of a 6-circle diffractometer (Kohzu NZD-3) with a sample to detector distance of 1051 mm. The samples were aligned such that for $\omega = 0°$ the incident beam was in the plane of the sample surface and parallel to the 20 mm long side of the samples. To measure the reflectivity, the samples were moved in steps of $\Delta\omega = 0.01°$ with respect to the incident beam, while the detector arm was moved accordingly, always preserving the relation $2\Theta = 2 \cdot \omega$. Due to a slit with a full width of 0.4 mm in front of the detector an angular resolution of 0.022° can be calculated, corresponding to a q-resolution of 3.9×10^{-3} Å^{-1}. Counting times per data point ranged between 1 s for $\omega \leqslant 1.2°$. up to 10 s for $\omega \geqslant 5.95°$. Adjustable attenuators were used for $\omega < 0.5°$.

5.2.1.2 *Data analysis*

The data were processed using OriginPro (OriginLab). The measured intensity was corrected for absorption by the attenuators and variations of the flux of the incident beam, which was constantly monitored by a point detector. Geometrical corrections of the intensity have been applied as described by Salah et al. [100] for an entrance slit with a width of 0.3 mm in front of the sample and a sample length of 20 mm. I.e. up to the spill-over angle ω_{so} of 0.859° the intensity was multiplied by a factor of $0.015/\sin(\omega)$. Subsequently the reflectivity profiles were normalised to the intensity at the plateau of total external reflection. The background was subtracted in form of the sum of a power-low function and a constant. To analyse the disorder of the samples, the diffraction signal was fitted by a superposition of pseudo Voigt peaks, i.e. linear combinations of a Lorentzian and a Gaussian peak each. The lattice spacing d was calculated from the peak positions q_c, following the relation $d = n \cdot 2\pi/q_c$, where n is the diffraction order. The integral breath of the individual diffraction orders were calculated from the fit results, and corrected for instrumental broadening as described below. The paracrystalline distortion parameter g and the crystallite size were calculated, according to Hosemanns paracrystal theory (see Section 3.1.3) [57, 64, 101].

5.2.1.3 *Correction for instrumental broadening*

To verify the q-resolution calculated from geometrical considerations, an upper estimate of the instrumental broadening was determined experimentally from the width of the Si (200) peak observed in the reflectivity measurement

of the C_{70} layer deposited at 120 °C. With 4.3×10^{-3} Å^{-1} the result agrees well with the geometrical approximation (3.9×10^{-3} Å^{-1}) and is a magnitude lower than the width of the most narrow diffraction peaks from the investigated materials. It can be estimated that completely neglecting instrumental broadening would result in a relative error of up to 2 % for the domain size and only up to 0.2 % for the paracrystalline distortion. The low sensitivity of the results to the correction, justifies to subtract the instrumental broadening by approximating all peak shapes by Gaussian profiles:

$$\delta b_s = \sqrt{\delta b_m{}^2 - \delta b_i{}^2} \tag{5.1}$$

Here, δb_s is the corrected peak broadening, i.e. the broadening contribution of the sample, δb_m is the peak width measured in the experiment and $\delta b_i = 4 \times 10^{-3}$ Å^{-1} is the peak broadening ascribed to the instrument.

5.2.2 *Grazing-incidence wide-angle X-ray scattering*

GIWAXS measurements were performed using the beam parameters described at the beginning of this Section 5.2. The signal was recorded by a PerkinElmer XRD 1621 flat panel detector 1459 mm behind the sample. The detector was placed in asymmetric position, with the primary beam positioned close to one corner of the detector, to reach maximum q-values of 2.6 Å^{-1} in both in-plane ($q_\parallel$) and out-of-plane ($q_\perp$) direction. An incidence angle α_i of 0.07° (1.22×10^{-3} rad) was used to promote the signal of the C_{70} layer. It corresponds to a penetration depth l of 14.6 nm as calculated via the relation $l = \lambda/(2\pi(\alpha_c^2 - \alpha_i^2)^{1/2})$ [71] with the critical angle $\alpha_c = 1.40 \times 10^{-3}$ rad. The latter was determined from the q-position of the edge of the plateau of total external reflection found in the reflectivity measurements of the respective samples. For each sample 120 exposures with a counting time of 1 s each were summed up. To generate 2d maps with in-plane and out-of-plane component of the scattering vector as abscissa and ordinate respectively a MATLAB program developed by Stefan Fischer [102] was modified to fit the detector geometry. The applied calculations are given in Section 3.3.3. Additionally, a refraction correction was added according to H. Doschs semikinematical approach [71], i.e. the out-of-plane component of the momentum transfer $q_z = Re(k_i - k_f)$ was calculated from the refraction corrected initial and final momentum k_i and k_f:

$$k_{i,f} = \pm(2\pi/\lambda) \cdot (sin^2\alpha_{i,f} - 2\delta - 2i\beta)^{1/2} \tag{5.2}$$

where α_f is the angle between the sample surface and the scattered wave k_f, $\delta = 1.141 \times 10^{-6}$ and $\beta = 3.961 \times 10^{-10}$ as determined for C_{70} at 20 keV using the Index of Refraction online tool of E.M. Gullikson [103, 104]. The Bragg peaks were separated from broad scattering background using the Subtract Background tool of ImageJ [105] with a rolling ball radius of 150 pixels. Subsequently, a constant of 1000 was added to eliminate negative intensity values. The processed data were plotted using OriginPro (OriginLab). Expected peak positions were calculated from a given unit cell by calculating the reciprocal lattice vectors, subsequently calculating the scattering vector $\boldsymbol{q}$ for numerous combinations of miller indices and finally projecting $\boldsymbol{q}$ onto the assumed orientation of the lattice on the sample to extract its in- and out-of-plane magnitudes. The respective calculations were performed analogously to Chapter 3 of Reference [98].

5.2.3 *Grazing-incidence small-angle X-ray scattering*

The GIWAXS measurements were performed using a PerkinElmer XRD 1621 flat panel detector in symmetric position around the primary beam. The sample to detector distance was 2309 mm, as calibrated using silver behenate powder. To reduce air scattering a helium filled beam tube was placed between sample and detector. The incident angle was varied between 0.04° and 0.06° to yield maximum signal. Reading off the critical angle for total reflection of the pentacene-C_{70} bilayers from the q-position of the edge of the plateau of total external reflection in the reflectivity measurements, the corresponding penetration depths were calculated to range between 8.2 nm and 14.6 nm [71, 106]. For each sample a series of twelve 10 s exposures were taken and averaged using ImageJ [105].The data were transferred into q-space by a modified version of the MATLAB program used for the GIWAXS analysis. Here, data points from both sides of the direct beam position were preserved, to increase the accuracy of the further analysis. Negative q_{xy} values were assigned to data points left of the direct beam position. As only horizontal cuts through the 2d profile at $q_\perp \gg q_{yoneda}$ were analysed, the born approximation was applicable in this case and refraction effects were neglected [71, 74, 107]. For further analysis horizontal line profiles were calculated by averaging the signal over q_z in the range between 0.09 Å^{-1} and 0.11 Å^{-1}.

5.2.4 *High-energy X-ray microbeam diffraction*

5.2.4.1 *Setup and real-space resolution*

Longitudinal transmission wide-angle X-ray scattering (WAXS) measurements were conducted at the high-energy materials science beamline (P07) at PETRA III at DESY. The porous layers were aligned parallel to the X-ray beam, which was focussed down to vertical full width at half maximum (FWHM) of few micrometres on the sample using aluminium compound lenses. The scattered intensity was measured with a PerkinElmer XRD 1621 flat panel detector in transmission mode. A beam stop was placed behind the sample to protect the detector and to reduce air scattering. The data shown in this thesis was acquired during three different beamtimes. The 30 mA cm^{-2} npSi sample was measured during beamtime 1 with an X-ray energy of 98.5 keV, a beam cross section of about 5 µm × ~50 µm (vertical × horizontal FWHM) and a sample-detector distance of 2000 mm. For the 15 mA cm^{-2} npSi and 25 mA cm^{-2} npSi samples, which were measured during beamtime 2, the respective values were 80.0 keV, 2 µm × ~30 µm and 2000 mm; for the npAAO samples, measured during beamtime 3, 101.9 keV, 1.6 µm × ~30 µm and 2520 mm.

The setup allowed for a precise alignment of the samples in steps of $\Delta\omega = 0.001°$. The uncertainty caused by the finite stepwidth affects the real space resolution by less than 0.2 µm for a sample length of 1 cm and is thus neglectable compared to the influence of the beam width. For high-energy diffraction experiments on npAAO samples these considerations suffice and the real space resolution is directly given by the beam profile. For the npSi samples, however, a higher sample alignment uncertainty has to be taken into account, which is expected to affect the real space resolution considerably. This uncertainty most likely arises from an inhomogeneity of the thickness of the electrochemically etched npSi layers (see Appendix a.2). As a result, two interfaces (npSi to air and Si to npSi) that are slightly tilted to each other reflect the high-energy X-ray beam when it is brought to grazing incidence. The most effective alignment method for high-energy X-ray experiments is to rock the sample and monitor the intensity of the direct beam, that is decreased by reflection on both sides of the surface. The maximum in between the two evolving intensity minima in the angular scan corresponds to parallel alignment of the samples surface to the beam. The presence of two non parallel interfaces in the sample therefore severely reduces the precision of the alignment, as the signature of both interfaces superimpose. Consequently the real space resolution of high-energy experiments on npSi is expected to

be considerably lower than given by the beam profile and to vary between the individual samples.

5.2.4.2 *Background correction*

To facilitate background correction the intensity scattered of a nanoporous reference sample without perovskite was measured for all setups. Using the "Nika" package [108] for Igor Pro (WaveMetrics) all oriented background features as broadened Bragg peaks from the npSi scaffold, or respectively the silicon substrate and residual aluminium for the npAAO samples, were masked and the remaining data were reduced to one dimension. To correct for amorphous background, the one-dimensional reference signal of the corresponding depth was scaled and subtracted from the data. Due to limited beamtime only one npSi reference sample could be measured for each setup. As the thickness of the porous layers varies with anodisation current density, each measurement had to be correlated to the background measurement at the same relative depth, i.e. the background measurement with the closest resemblance to the background of the data, as recognisable in the low q-range. This step and all further analysis were performed using OriginPro (OriginLab).
For the $15\,\mathrm{mA\,cm^{-2}}$ npSi/$MAPbI_3$ sample and the $25\,\mathrm{mA\,cm^{-2}}$ npSi/$MAPbI_3$ sample the signal of crystalline PbI_2 was observed primarily close to the surface. As this signal consists of broadened peaks, which overlap with the $MAPbI_3$ signal it was subtracted before analysing the perovskite crystallite sizes. The scattered intensity recorded 5 µm below the surface of the $15\,\mathrm{mA\,cm^{-2}}$ npSi/$MAPbI_3$ sample is dominated by the PbI_2 signal and was used to remove its influence from the other patterns: For each depth, the contribution of PbI_2 to the diffraction profile was quantified by the difference of the intensity at the position of the most intense PbI_2 diffraction peak $(103)\&(113)$ and the corresponding intensity value at the unmodified high angle flank of the $MAPbI_3$ $(004)\&(220)$ diffraction peak. The respective proportion of the PbI_2 signal - represented by the diffraction profile recorded 5 µm below the surface - was then subtracted from the intensity profile to isolate the contribution of the perovskite crystallites.
For the $25\,\mathrm{mA\,cm^{-2}}$ npSi/$MAPbBr_3$ sample a similar procedure was applied to correct for the broad background, also primarily occurring close to the surface. The signal at the surface was used to define a background signature. It exhibits only weak $MAPbBr_3$ peaks, which together with the Pb diffractions were excluded from the analysis, interpolating linearly over the missing q-range. For each depth the resulting background signal was scaled by the quotient of the measured intensity values at the position of maximum perovskite signal and the position of the intensity maximum of

the background signature. The scaled background signal was then subtracted from the scattered intensity for each measurement.

5.2.4.3 *Peak width analysis*

For the npSi/$MAPbI_3$ samples the ranges around three peaks consisting of two $MAPbI_3$ reflections each $((002)\&(110), (004)\&(220)$ and $(224)\&(400))$ were fitted by the sum of six Gaussian peaks with fixed positions. For the $15\,mA\,cm^{-2}$ npSi/$MAPbI_3$ sample and the $25\,mA\,cm^{-2}$ npSi/$MAPbI_3$ sample the peak positions were directly calculated from the crystal structure described by Stoumpos et al. ($a = b = 8.849$ Å and $c = 12.642$ Å) [109], as this provided the best fits. For the $30\,mA\,cm^{-2}$ npSi/$MAPbI_3$ sample the peak positions were calculated from a likewise tetragonal structure with slightly larger lattice constants ($a = b = 8.90$ Å and $c = 12.71$ Å). The diffraction profiles of npSi/$MAPbBr_3$, npAAO/$MAPbBr_3$, and npAAO/$CsPbBr_3$ were fitted by the sums of Gaussian peaks with peak positions described by a single fit parameter each. For $MAPbBr_3$ the peak positions were expressed in terms of the lattice spacing a for cubic structure. For $CsPbBr_3$ the peak positions were calculated for an orthorhombic structure, using the lattice parameter a as fit parameter and keeping the ratios of the lattice parameters fixed to the values described by Stoumpos et al. [110].
Using the Scherrer approximation (EQUATION 3.6), the crystallite size L was calculated from the positions (2Θ) of the perovskite peaks and their FWHM $\Delta(2\Theta)$, which in the case of npAAO were previously corrected for instrumental broadening.

5.2.4.4 *Correction for instrumental broadening*

Due to the small crystallite size within the npSi films, instrumental broadening was neglected in the analysis of these samples. For the $15\,mA\,cm^{-2}$ npSi sample and the $25\,mA\,cm^{-2}$ npSi sample this affected the results by less than 0.1 % as calculated from a lanthanum hexaboride (LaB_6) calibration measurement, for the $30\,mA\,cm^{-2}$ npSi sample by 0.4 % or less, as calculated from a CeO_2 calibration measurement. As the npAAO samples showed much narrower perovskite diffraction peaks, instrumental broadening was accounted for when analysing their crystallite sizes. The corrected peak broadening ($FWHM_s$) was calculated from the measured peak widths ($FWHM_m$) and the instrumental broadening ($FWHM_i$) assuming Gaussian line shapes for all peak broadening contributions:

$$FWHM_s = \sqrt{FWHM_m{}^2 - FWHM_i{}^2}. \tag{5.3}$$

The instrumental broadening was determined from a calibration measurement of a LaB_6 powder sample with 10 µm particle size (purchased from Sigma Aldrich). It showed an almost linear increase with the scattering vector q from 0.007 $Å^{-1}$ at q = 0.5 $Å^{-1}$ to 0.015 $Å^{-1}$ at q = 4.2 $Å^{-1}$, and was about 1 % stronger in the plane of the sample surface compared to the direction perpendicular to it.

5.2.5 *Transmission small-angle X-ray scattering*

The SAXS data of nanoporous thin films presented in this work were kindly provided by Anton Böhm (LMU). They were acquired at beamline P08 at PETRA III at DESY measuring in transmission with a 20 keV X-ray beam perpendicular to the sample surface. The direct beam was blocked and the scattered intensity was recorded by a PerkinElmer XRD 1621 flat panel detector with a sample to detector distance of 2435 mm. The setup was calibrated using silver behenate. In the analysed q-region between 0.014 $Å^{-1}$ and 0.3 $Å^{-1}$ a q-resolution of 2×10^{-3} $Å^{-1}$ was achieved. The Nika package [108] for Igor Pro (WaveMetrics) was used to reduce the data to one dimension. Further analysis was performed with OriginPro (OriginLab). For the Porod analysis of the npSi poresize the software SASfit [111] was used.

Part III

STRUCTURAL PROPERTIES OF C_{70}-PENTACENE HETEROSTRUCTURES AND METAL-HALIDE PEROVSKITE NANOCRYSTALLITES

6

C_{70}- PENTACENE HETEROSTRUCTURES[1]

6.1 CRYSTAL STRUCTURE OF C_{70} ON THE PENTACENE THIN-FILM PHASE

To address the question which crystal structure C_{70} exhibits when deposited on thin-film phase pentacene and how its growth is influenced by the deposition temperature and rate, different X-ray diffraction techniques were applied. To identify the three-dimensional crystal structure grazing-incidence wide-angle X-ray scattering (GIWAXS) was used, while high resolution X-ray reflectivity measurements allowed to quantify disorder and to precisely determine the out-of-plane lattice spacing. All scattering experiments presented in this chapter have been performed at the High Resolution Diffraction Beamline P08 at DESY (Deutsches Elektronen-Synchrotron).

6.1.1 *Deposition-temperature dependency of the out-of-plane structure*

FIGURE 6.1 shows the reflected intensity from pentacene-C_{70} bilayers deposited onto Si substrates with a 300 nm thick thermal SiO_2 layer. While all pentacene layers were deposited onto unheated substrates, the C_{70}-deposition temperature T_D, i.e. the sample temperature during C_{70}-deposition, was varied between 25 °C and 115 °C in steps of $\sim$ 15 °C. After applying the appropriate geometrical corrections (see SECTION 5.2.1) the curves have been normalised to the intensity at the plateau of total external reflection. The observed Bragg peaks can be assigned to two different lattice spacings. Peaks marked by blue vertical lines correspond to a lattice spacing of about 15.5 Å and can be assigned to the pentacene thin-film phase [35]. Green vertical lines mark peak positions that correspond to an out-of-plane lattice spacing of 8.56 Å, which can be attributed to the C_{70} layer.

While the pentacene peaks vary mainly in height, for the C_{70} peaks strong variations in height as well as in width are observed and even the peak position varies noticeably. The insets in FIGURE 6.1 show the background corrected data for the first two C_{70} diffraction orders in linear representation and highlight the strong variation of the C_{70} signal with the deposition temperature. It should be noted that the scaling of the abscissa is kept constant

1 The scattering data presented in this chapter were acquired together with Stefan Fischer, Clemens Liewald, Jasmin Moazzami-Fallah, and Bert Nickel (LMU) with the assistance of Florian Bertram, and Uta Rütt (DESY).

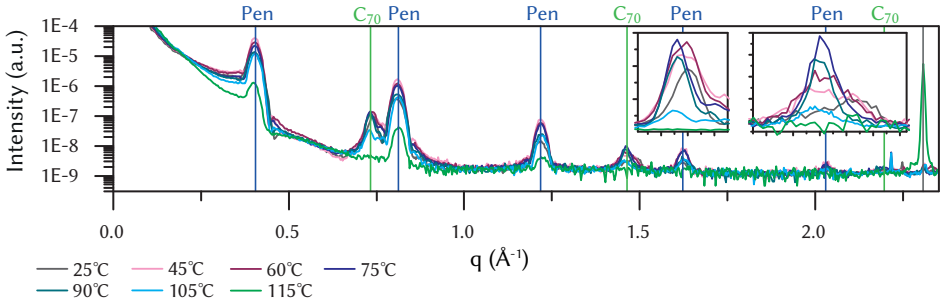

FIGURE 6.1: Normalised reflectivity of pentacene-C_{70} bilayers. C_{70} was deposited onto the pentacene films with a rate of 0.18 Å/s at varying deposition temperatures. Blue vertical lines mark peak positions that correspond to the pentacene thin-film phase, green vertical lines indicate C_{70} peaks and the grey vertical line marks the Si (200) peak. The insets showing the background corrected data for the first two C_{70} diffraction orders in linear representation highlight the dependency of peak height, width and position on the C_{70}-deposition temperature. The scaling of the abscissa is equal in both insets, while the ordinate spans a 16 times larger range in the first inset.

between the two insets, while the ordinate spans a 16 times smaller range for the second order peak. To precisely quantify the positions, intensities and widths of the peaks the background corrected data were fitted by a superposition of pseudo-Voigt functions (see SECTION 5.2.1). In FIGURE 6.2 A and B the out-of-plane lattice spacings of pentacene and C_{70} obtained from the peak positions are plotted against the C_{70}-deposition temperature. Data points correspond to the average values calculated from the 2 to 5 diffraction peaks, error bars to their standard deviation. While the values for pentacene vary irregularly around 15.5 Å (see linear fit in FIGURE 6.2 A), a monotonous increase with temperature is observed for the out-of-plane lattice spacing of C_{70}. A linear fit reveals a slope of $175 \times 10^{-6}\,\mathrm{K}^{-1}$.

As measure for the amount of crystalline matter in the two layers, the normalised integrated intensity of the diffraction peaks is plotted against the C_{70}-deposition temperature in FIGURE 6.3 A and B for pentacene and C_{70}, respectively. The integrated intensity of the third pentacene diffraction order is shown. Positioned at $q = 1.22\,\text{Å}^{-1}$ it is well comparable to the second order C_{70} diffraction ($q = 1.46\,\text{Å}^{-1}$), which yielded the most reliable results, as explained below. A strong increase of the integrated intensity occurs for raising the C_{70}-deposition temperature from 25 °C to 46 °C. This suggests, that the annealing of the pentacene film allows for post deposition crystallisation, enhancing the proportion of crystalline matter in the pentacene film. For a further increase of the C_{70}-deposition temperature an almost linear decrease of the integrated intensity is observed, suggesting that the amount of thin-film phase pentacene declines. In FIGURE 6.3 B the integrated intensity of the second order diffraction of the C_{70} layers is shown. This diffraction order was

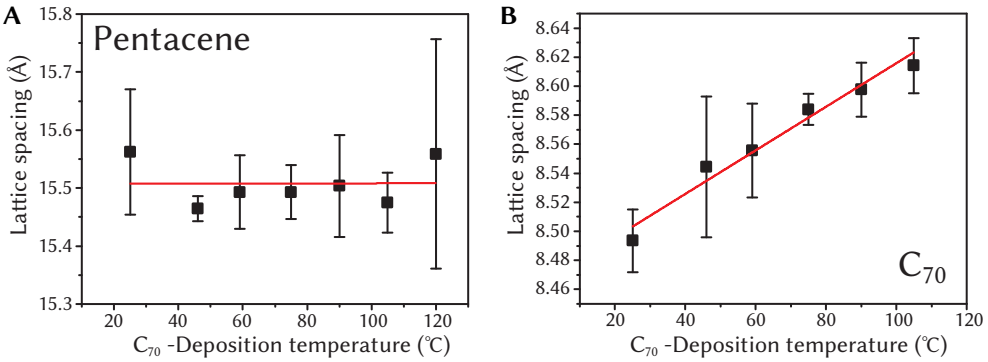

FIGURE 6.2: Dependency of the out-of-plane lattice spacings of pentacene-C_{70} bilayers on the C_{70}-deposition temperature. The results obtained from the positions of the different diffraction orders were averaged, error bars correspond to their standard deviations. **A** The lattice constant of pentacene does not show a clear dependency on the C_{70}-deposition temperature (see linear fit shown in red), i.e. no post deposition rearrangement of the structure exceeding the uncertainty of the experiment is observed. **B** The C_{70} lattice spacing increases considerably with the deposition temperature and can be approximated by a linear fit with a slope of $0.0015\,\text{Å}\,\text{K}^{-1}$.

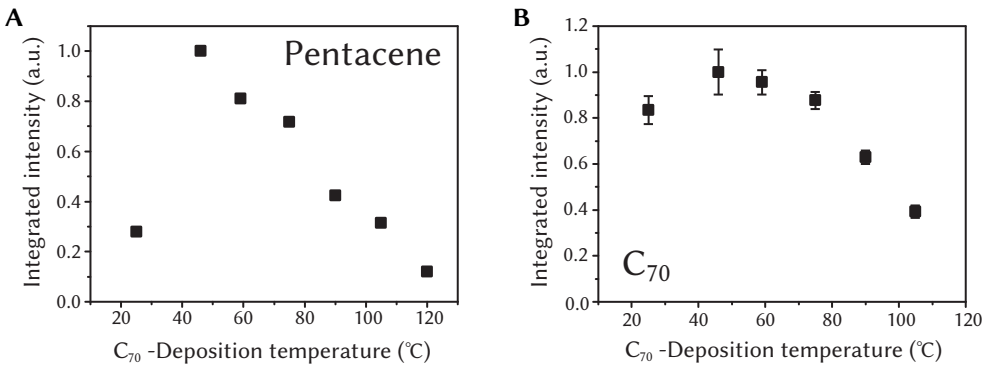

FIGURE 6.3: Normalised integrated intensity of the out-of-plane diffraction peaks as a measure for the amount of crystalline matter plotted against the C_{70}-deposition temperature. Error bars represent the propagated standard errors of the fit parameters. **A** Post deposition annealing of the pentacene film initially leads to an increase of the integrated intensity of the pentacene diffraction peaks, here shown for the third order diffraction ($q = 1.22\,\text{Å}^{-1}$). For temperatures exceeding 46 °C an almost linear decrease is observed. **B** For the C_{70} signal an initial slight increase of the integrated intensity with the C_{70}-deposition temperature is observed, followed by an initially slow decrease, that becomes much steeper at 75 °C. Here the results of the second order peak ($q = 1.46\,\text{Å}^{-1}$) are shown.

chosen, because the first order is superimposed by the much stronger pentacene second order diffraction, hampering a precise analysis, and the third order peak intensities are approaching the noise level for high deposition temperatures and room temperature. For increasing C_{70}-deposition temperatures initially a slight increase of the integrated intensity is observed. This might well be an effect of the thermal energy promoting crystalline growth, as described in literature for many molecular beam deposed materials [23, 112]. For higher C_{70}-deposition temperatures FIGURE 6.3 B indicates a decrease of the integrated intensity. For temperatures up to 75 °C the variations are however in the same order of magnitude as the standard error. For temperatures of 90 °C and above a much faster decrease of the integrated intensity is observed, clearly exceeding the uncertainty. This is likely to be related to a disruption of the pentacene crystal structure, for which the data shown in FIGURE 6.3 A is a first indication. This will be discussed in SECTION 6.1.2 after all relevant data has been presented.

Crystalline disorder was analysed according to the paracrystal theory of Hosemann [57, 64, 101], as described in SECTION 3.1.3. From a linear fit of the dependency of the integral breadth of the peaks on their squared diffraction order, the paracrystalline distortion parameter g can be extracted together with the domain size L. The results are presented in FIGURE 6.4. The C_{70} layers deposited at temperatures between 25 °C and 90 °C yielded three evaluable diffraction orders. For the one deposited at 105 °C only two diffraction orders were observable and consequently no uncertainty could be determined for the corresponding values of g and L. For all other data points error bars as propagated from the uncertainty of the linear fits are plotted in FIGURE 6.4. In several cases they are however smaller than the square marking the data point. It should be noted that these errors can be understood as lower estimate of the experimental uncertainty. A reliable assessment of its upper limit is not achievable, as not all relevant factors can be reasonably quantified. The obtained paracrystalline distortion parameters of the pentacene and C_{70} layers are plotted against the C_{70}-deposition temperature in FIGURE 6.4 A and B, respectively. In the range between 46 °C and 105 °C the paracrystalline distortion of the pentacene layers varies only slightly around a value of 1.1 %. The values for the samples with C_{70}-deposition temperatures of 25 °C and 120 °C differ with 2.1 % and 4.5 %, respectively. This might indicate that annealing the pentacene layer at 46 °C increases order, while temperatures exceeding 105 °C lead to increased disorder. The paracrystalline distortion of C_{70} shows a strong dependency on the C_{70}-deposition temperature in the entire investigated temperature range. Starting at 5.4 % for a deposition temperature of 25 °C a monotonous decrease of the paracrystalline distortion

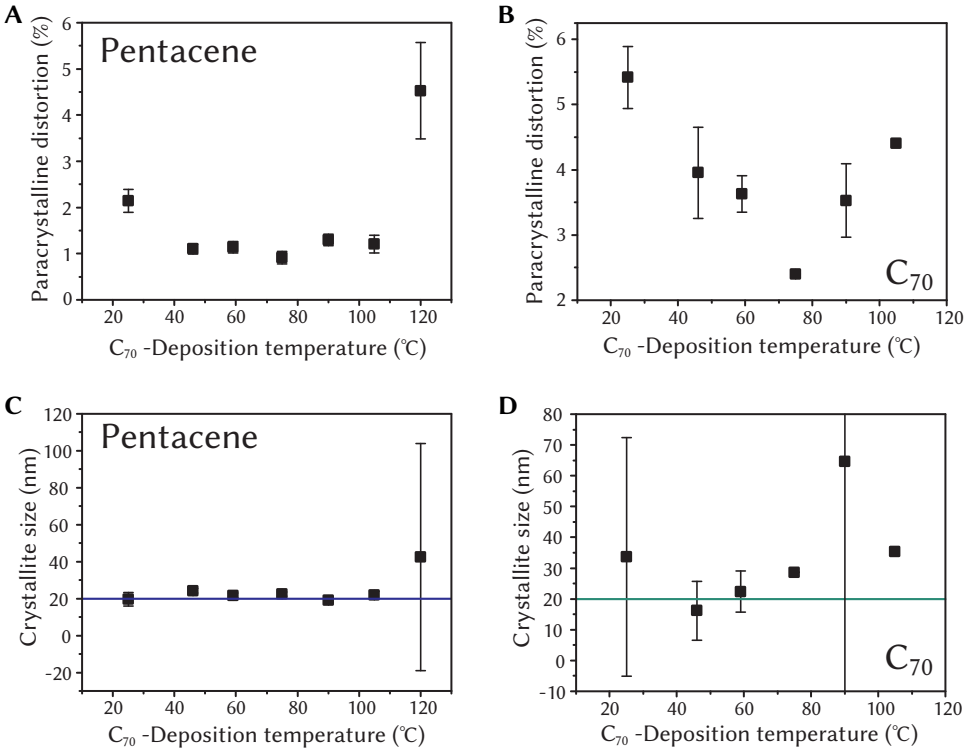

FIGURE 6.4: Paracrystalline distortion and out-of-plane crystallite size in pentacene-C_{70} bilayers. Error bars correspond to the propagated standard error from the linear fit of the integral breadths. For pentacene the plotted values were obtained from fitting three and five diffraction orders, respectively, for T_D = 120 °C and all other C_{70}-deposition temperatures. For C_{70} two and three diffraction orders were analysed, respectively, for the layer deposited at 105 °C and all other layers. **A** In the range between 46 °C and 105 °C the paracrystalline distortion parameter of the pentacene layer shows little dependency on the C_{70}-deposition temperature, only slightly varying around 1.1 %. The pentacene films on which C_{70} was deposited at room temperature and at 120 °C show a paracrystalline distortion of 2.1 % and 4.5 %, respectively. **B** The paracrystalline distortion of C_{70} deposited onto pentacene thin-film phase exhibits a minimum at T_D = 75 °C. **C** All investigated pentacene layers exhibit out-of-plane crystallite size values of approximately 20 nm, with the only exception of the sample with T_D = 120 °C. Due to its large uncertainty this data point is still in accordance with the measured layer thickness of 20 nm, which is depicted as blue horizontal line. **D** The standard errors for the C_{70} layers deposited at 25 °C and 90 °C are 39 nm and 100 nm, respectively, i.e. larger than the results of the crystallite size. Regarding the other data points only, the crystallite size appears to increase with the C_{70}-deposition temperature. Due to the generally high level of uncertainties (note that error bars have to be considered as lower estimates only) it however remains unclear if this is a real trend or noise.

parameter with the deposition temperature is observed, down to a value of 2.3 % for deposition at 75 °C. For further increase of the deposition temperature an increase of distortion is observed, up to a value of 4.4 % at 105 °C before the C_{70} diffraction signal is completely lost for deposition at 120 °C.

FIGURE 6.4 C shows the resulting out-of-plane crystallite sizes of the pentacene layers. Most data points lie fairly close to the blue horizontal line marking the intended layer thickness of 20 nm as measured by a quartz crystal microbalance. Only the one at 120 °C deviates considerably from this value. Due to the large uncertainty of this data point this divergence is however not significant. The data thus indicates, that the crystal growth is continuous throughout the entire layer thickness without being interrupted by grain boundaries and that this state is retained when the samples are exposed to temperatures of at least up to 105 °C. For the C_{70} layers the results show stronger variations from the nominal layer thickness of 20 nm (green line in FIGURE 6.4 D) determined with a quartz crystal microbalance. Disregarding the data points at 25 °C and 90 °C for which the standard error exceeds the magnitude of the result, and the one at 105 °C which was determined from two diffraction orders only, FIGURE 6.4 D seems to suggest an increase of the crystallite size with T_D from 16 nm at 46 °C to 29 nm at 75 °C. However, due to the generally high level of uncertainties (note that all error bars in FIGURE 6.4 have to be considered as lower estimates only), no unambiguous conclusion can be drawn.

6.1.2 *Morphology of pentacene-C_{70} bilayers*

To assist the interpretation of the diffraction data at higher C_{70}-deposition temperatures, the morphology of two pentacene-C_{70} bilayers with C_{70}-deposition temperatures of 105 °C and 140 °C, respectively were investigated by AFM. For a C_{70}-deposition temperature of 105 °C the typical topographic signature of a fullerene film deposited on thin-film phase pentacene is observed [113, 114], as FIGURE 6.5 A shows. Droplet-like C_{70} grains evolved on top of pyramid-shaped grains that are characteristic for the pentacene thin-film phase [35]. Only few small flat areas of minimum height suggest minor interruptions of the pentacene layer, possibly caused by heating of the sample. Typical height differences between valleys and pyramid tips are about 15 nm (including the C_{70} grains). Between the flat areas and adjacent pyramid tops a height difference of about 30 nm is found.
Depositing C_{70} onto a pentacene thin-film heated to 140 °C in contrast yields a very different morphology. Irregularly shaped, disconnected islands are observed, most of which show a typical height of about 20 nm to 30 nm,

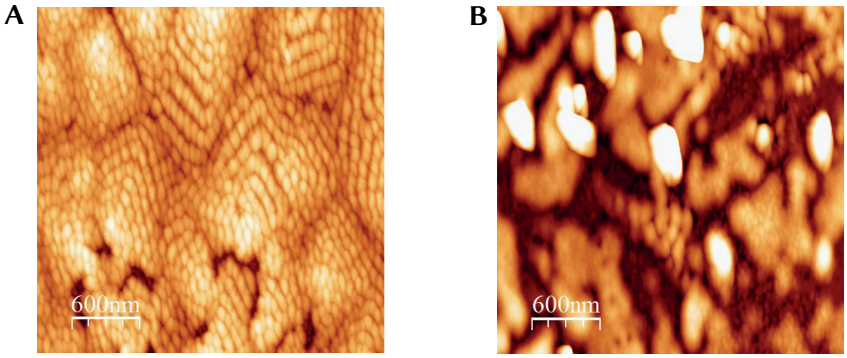

FIGURE 6.5: AFM images of pentacene-C_{70} bilayers. C_{70} was deposited with a rate of 0.1 Å s^{-1} onto samples with different temperatures T_D. **A** T_D = 105 °C. **B** T_D = 140 °C. The sample with T_D = 105 °C shows an almost completely closed layer of pyramid-shaped pentacene grains that are overlaid by droplet-like C_{70} grains, while the sample with T_D = 140 °C exhibits an inhomogeneous morphology of disconnected islands of irregular height, ranging from 20 nm to 180 nm.

while few reach heights of up to 180 nm. Between these grains flat areas are observed, which most likely can be interpreted as pentacene free substrate. The entire base morphology is overlaid by round grains having diameters in the order of few tens of nanometres, suggesting that C_{70} aggregates formed on the strongly distorted pentacene layer, as well as on the bare substrate. The AFM investigation thus suggests, that the pentacene layer has partly rearranged or even sublimed, exposing parts of the substrate before or while C_{70} was deposited. These findings can explain the decrease of the amount of crystalline pentacene observed for higher C_{70}-deposition temperatures, if the molecules leaving the thin-film phase either aggregate in a different order or transfer to the gas phase. The results are moreover in line with the observed preservation of the out-of-plane pentacene crystallite size, as the typical pentacene grain heights remain unaltered. The early onset of the decrease of the integrated intensity of the pentacene signal starting at 46 °C (see FIGURE 6.3 A) might be connected to strain induced by thermal expansion and successive shrinking associated with heating and cooling of the samples. As it is known that a phase transition can be triggered when pentacene thin-films cool down after having been deposited at temperatures above 50 °C, it seems plausible that a comparable effect might occur in samples that are heated after deposition. In this context the observed initially slight and for higher temperatures stronger decrease of the amount of crystalline C_{70} for C_{70}-deposition temperatures above 46 °C could be interpreted as follows: An increasingly disturbed pentacene layer hampers the growth of crystalline C_{70}. Increasing the C_{70}-deposition temperature to 105 °C and higher exposes parts of the SiO_2 substrate. As previous X-ray reflectivity measurements had indicated amorphous growth of C_{70} on SiO_2 (see APPENDIX a.1), the amount of crystalline C_{70} can thus be expected to be proportional to the ratio of the

substrate that is covered with thin-film phase pentacene. This is in line with the observed decrease of the integrated intensity of the C_{70} signal with a comparable slope as the decrease of the pentacene thin-film phase signal. The C_{70} out-of-plane crystallite size should not be affected by the percentage of substrate area covered by pentacene and might even increase slightly with the C_{70}-deposition temperature, as thermal energy can be expected to assist continuous crystalline out-of-plane growth and the formation of more pronounced aggregates [115].

6.1.3 *Three-dimensional crystal structure*

The three-dimensional crystal structure of the bilayers was investigated by GIWAXS using an incident angle of 0.07°. Experiment and data processing are described in detail in SECTION 5.2.3. FIGURES 6.6, 6.7, and 6.8 show background corrected diffraction patterns from pentacene-C_{70} bilayers of different C_{70}-deposition temperatures. The data are plotted against the in-plane ($q_{\parallel}$) and out-of-plane component ($q_{\perp}$) of the scattering vector. Blue crosses indicate calculated peak positions of the pentacene thin-film phase as determied by Schiefer et al. [35]. For reasons of clarity only peaks of comparatively high intensity are marked. The remaining diffraction peaks can be assigned to the C_{70} layer. Their pattern resembles diffraction from a face-centred cubic (fcc) crystal oriented with the space diagonal of the unit cell parallel to the surface normal of the sample. Orange crosses in FIGURES 6.6, 6.7, and 6.8 represent the fcc peak positions calculated from the out-of-plane lattice spacing obtained from the reflectivity analysis of the respective sample (see FIGURE 6.2 B). In FIGURE 6.6 A they are indexed for $q_{\perp} \parallel [-111]$.

Especially for $T_D \leqslant 46\,°C$ (FIGURE 6.6 A and B) some of the observed C_{70} peaks show a noticeable deviation from the positions expected for fcc growth. This is most easily observed on the $(-3, 1, 1)$ and $(-3, -1, 1)$ peaks. With increasing C_{70}-deposition temperature the discrepancy decreases (FIGURE 6.7 A and B) and for $T_D = 90\,°C$ and higher (see FIGURE 6.8 A and B) the data is matched fairly well by the cubic model. While the highly symmetric C_{60} molecules were found to be orientationally disordered in crystals for temperatures above 249 K [116], Vaughan et al. found that ordering of the long axis of C_{70} molecules occurs for temperatures up to 345 K [117]. In agreement with this, fcc structure is commonly reported for C_{70} at high temperatures, while rhombohedrally distorted structures with $\alpha < 90°$ were described in literature for temperatures below ~ 350 K [117–119] as well as for high pressure (350 MPa [118], 1.2 GPa [120]). This prompts the hypothesis that C_{70} might grow in rhombohedral structure on the pentacene thin-film phase for

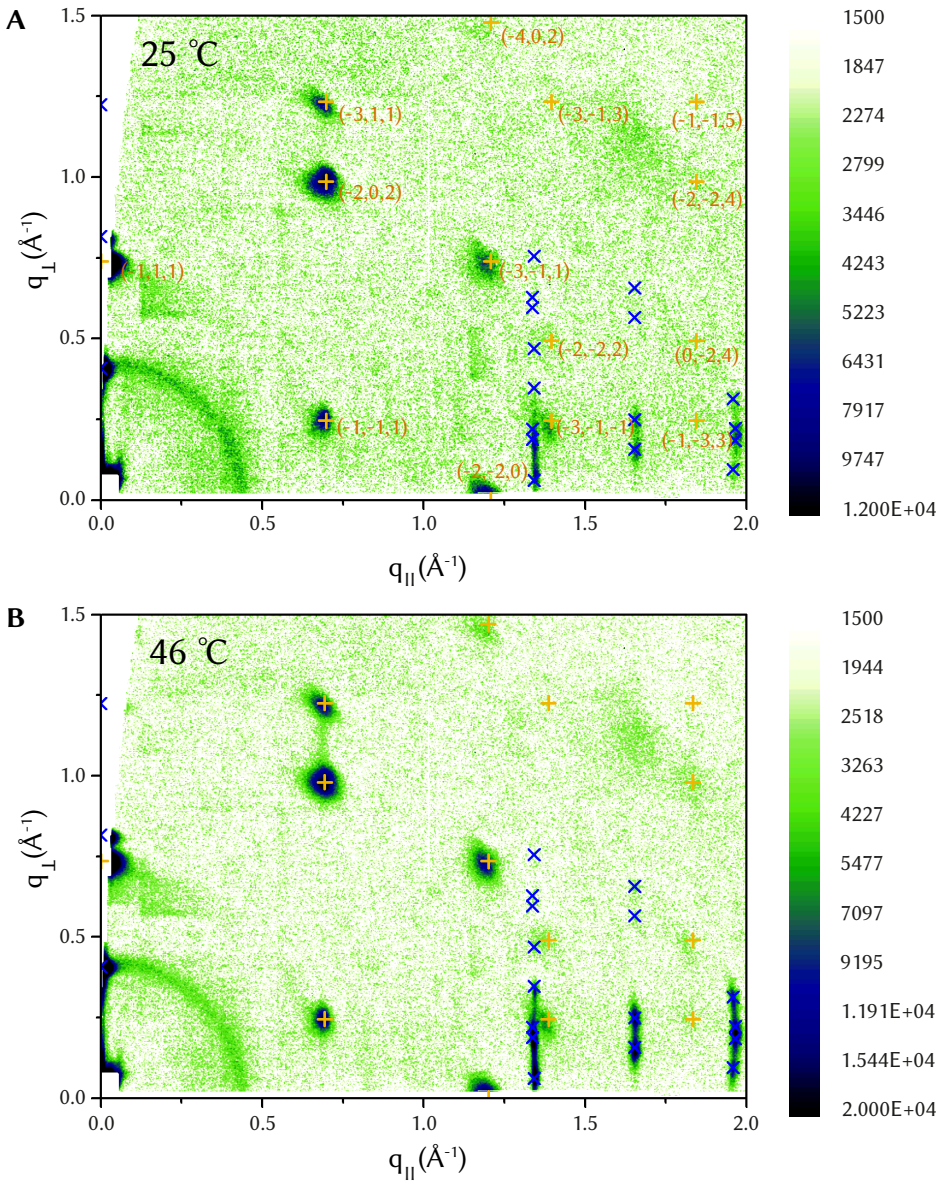

FIGURE 6.6: Logarithmically scaled, background corrected GIWAXS intensity of pentacene-C_{70} bilayers with different C_{70}-deposition temperatures: **A** $T_D = 25\,°C$. **B** $T_D = 46\,°C$. Blue crosses mark the calculated peak positions for the pentacene thin-film phase with the (001) plane lying parallel to the sample surface. Orange crosses indicate where fcc peaks are expected if the lattice constant corresponds to the out-of-plane lattice spacing obtained from the reflectivety analysis of the respective sample and the space diagonal of the unit cell is parallel to the sample normal. The peaks are indexed for $q_\perp \parallel [-111]$ in A. For these two C_{70}-deposition temperatures some fcc peak positions (e.g. $(-3,1,1)$ and $(-3,-1,1)$) are not in satisfactory agreement with the data.

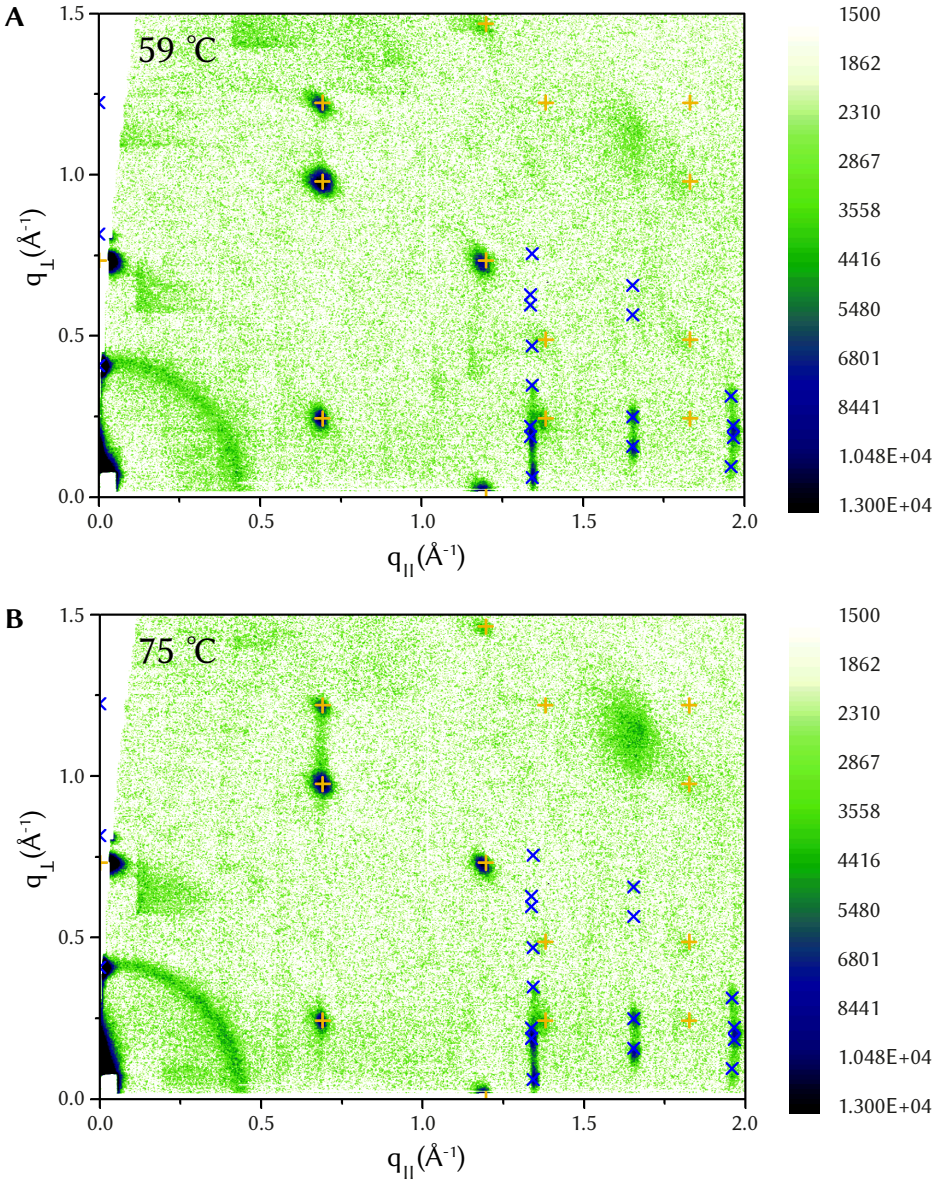

FIGURE 6.7: Logarithmically scaled, background corrected GIWAXS intensity of pentacene-C_{70} bilayers with C_{70}-deposition temperatures of: **A** T_D = 59 °C. **B** T_D = 75 °C. Calculated peak positions for the pentacene thin-film phase oriented with the (001) plane parallel to the sample surface are marked by blue crosses. Orange crosses show the peak positions expected for fcc growth in [−111] direction with the out-of-plane lattice spacing obtained from the reflectivity curve of the respective film. With increasing C_{70}-deposition the fcc model agrees increasingly well with the data.

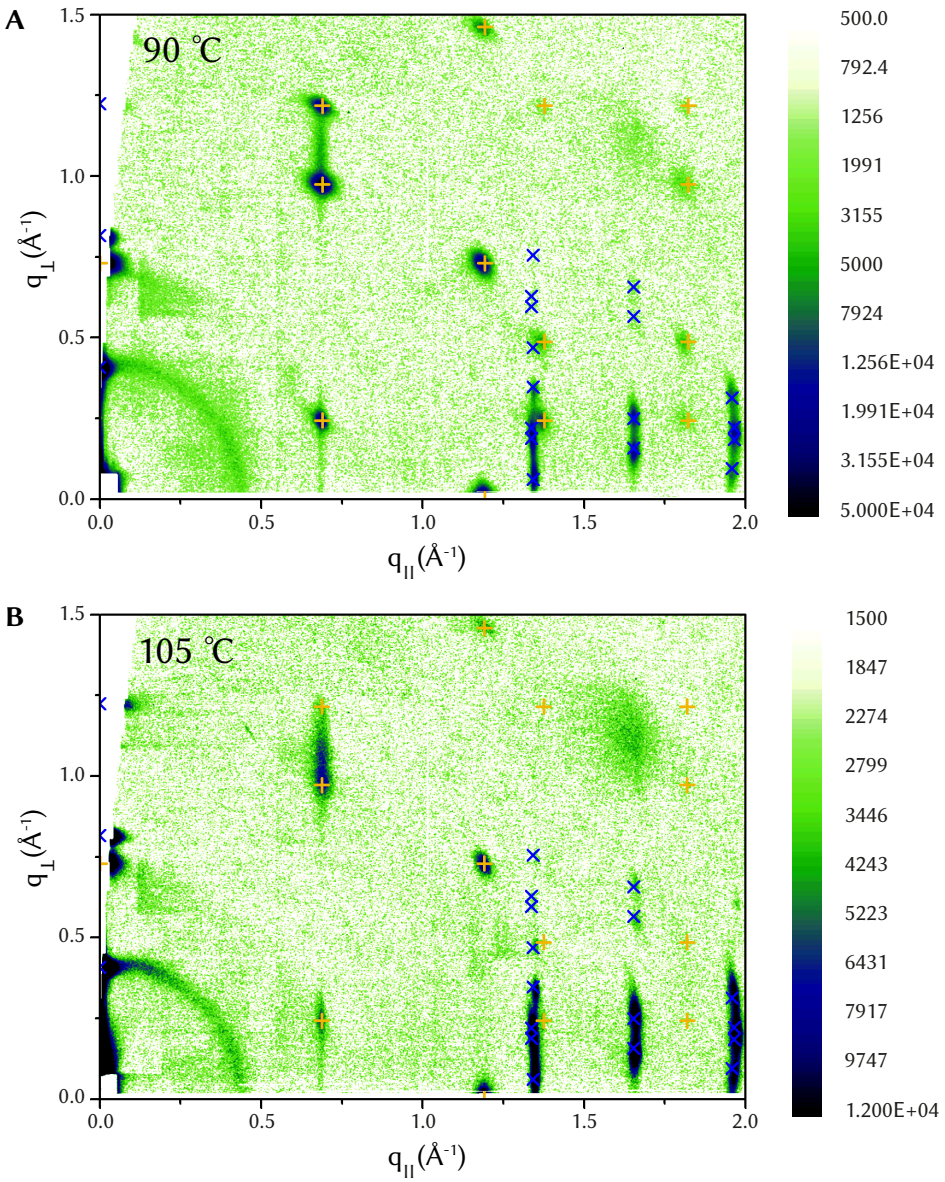

FIGURE 6.8: Logarithmically scaled, background corrected GIWAXS intensity of pentacene-C_{70} bilayers with different C_{70}-deposition temperatures. **A** T_D = 90 °C. **B** T_D = 105 °C. A comparison to calculated peak positions (orange crosses) shows, that fcc structure with the lattice constant corresponding to the out-of-plane lattice spacing obtained from the respective reflectivety curve agrees fairly well with the diffraction patterns of these samples. Blue crosses mark the peak positions calculated for the pentacene thin-film phase with the (001) plane lying parallel to the sample surface.

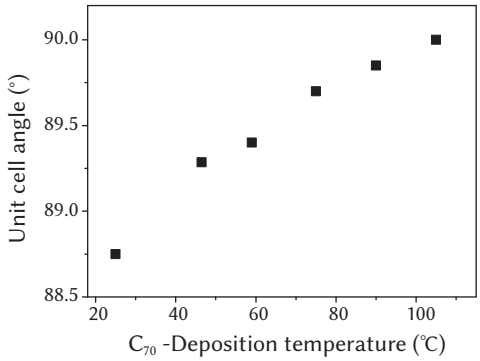

FIGURE 6.9: C_{70}-deposition temperature dependency of the lattice angle α calculated for a =14.92 Å from the out-of-plane lattice spacings obtained from reflectivity analysis under the assumption of rhombohedral growth with the [−111] direction parallel to the surface normal. This corresponds to the hypothesis that fcc structure occurs for C_{70}-deposition $\geq$ 105 °C, i.e. α = 90° while $\alpha < 90°$ for lower C_{70}-deposition temperatures.

sufficiently low deposition temperatures. For an orientation of the [−111] direction, i.e. one of the short space diagonals parallel to the surface normal, this would be in line with the observation that the out-of-plane lattice spacing is smaller for lower C_{70}-deposition temperatures.

To test if this assumption is consistent with the GIWAXS data, the following growth model is considered. All investigated C_{70} layers with $T_D \leq 90$ °C exhibit rhombohedral structure oriented with the [−111] direction parallel to the surface normal and the deposition temperature only affects the angle α between the lattice vectors, while their magnitude equals 14.92 Å as calculated from the out-of-plane lattice spacing observed for the C_{70} layer deposited at 105 °C assuming [−111] fcc growth. Then the angles plotted in FIGURE 6.9 yield the observed out-of-plane lattice spacings of C_{70} thin films deposited at the respective sample temperatures (see FIGURE 6.2 B). By definition α equals 90° for T_D = 105 °C. For lower C_{70}-deposition temperatures it decreases with decreasing temperature. The peak positions expected for the resultant unit cell values were calculated for all investigated C_{70}-deposition temperatures for the [−111] space diagonal of the real space unit cell oriented parallel to the surface normal.

FIGURE 6.10 compares these peak positions (depicted in violet) to the ones expected for a fcc structure (marked in orange) with the same out-of-plane lattice spacing on the example of the C_{70} layer deposited at $\sim$ 25 °C. As the minimum out-of-plane lattice spacing was observed for this deposition temperature, it also coincides with the smallest lattice angle of $\alpha = 88.75°$ in the framework of the assumptions mentioned above. Consequently the deviations from the cubic structure are most easily observed for this sample. Due to the symmetry breaking the peaks observed for the fcc structure split

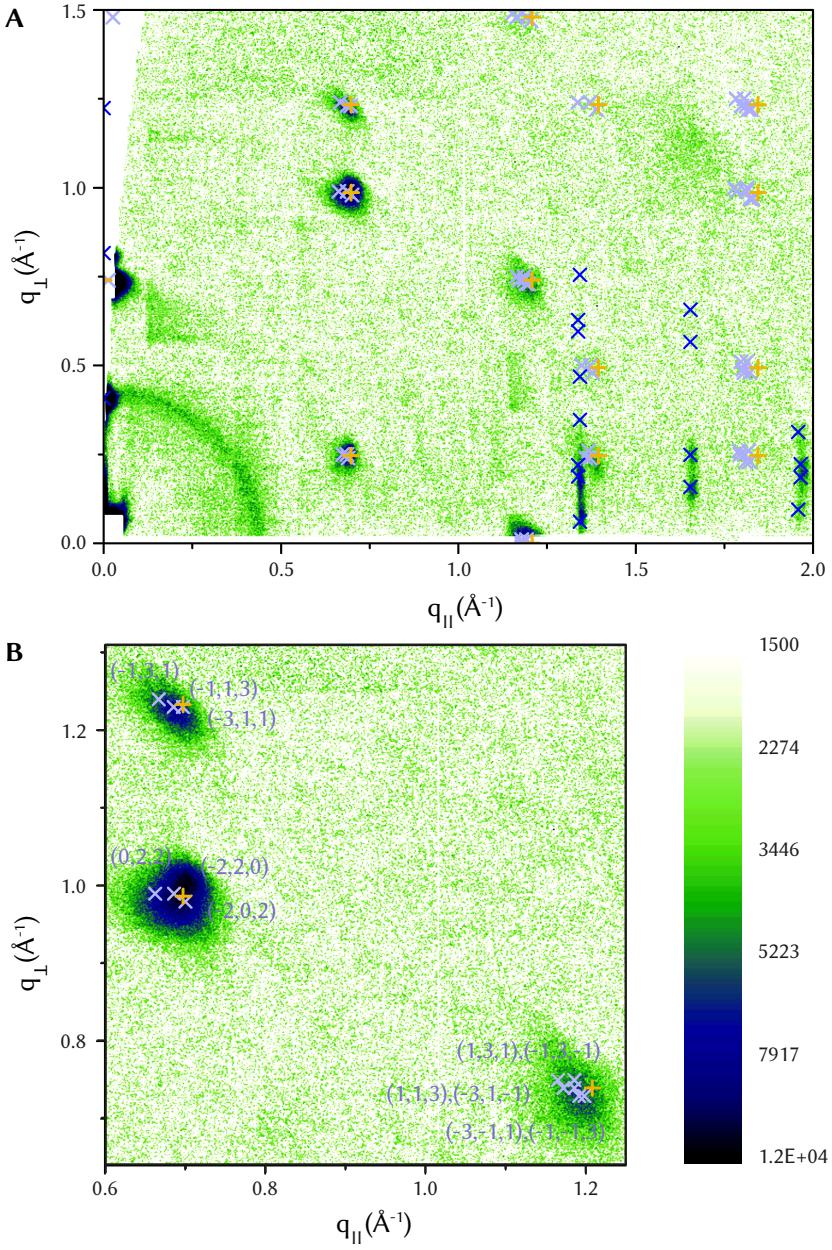

FIGURE 6.10: Comparison of GIWAXS data of a pentacene-C_{70} bilayer (T_D = 25 °C) with the peak positions calculated for fcc structure (orange crosses) and rhombohedral structure (violet crosses) with the $[-111]$ direction parallel to the surface normal. The rhombohedral lattice angle was calculated to match the out-of-plane lattice spacing observed in reflectivity analysis, assuming a = 14.92 Å. **A** Full q-range with observable C_{70} signal. Due to symmetry breaking the fcc peaks split up several times each. The shape of the asymmetric diffraction peaks correlates fairly well to the direction of this splitting. **B** Close up on the $(-3, 1, 1)$ and $(-3, -1, 1)$ fcc peak positions which show the strongest deviation from the data. For the rhombohedral model the deviations from the data are considerably smaller, although the in-plane lattice spacing is slightly overestimated.

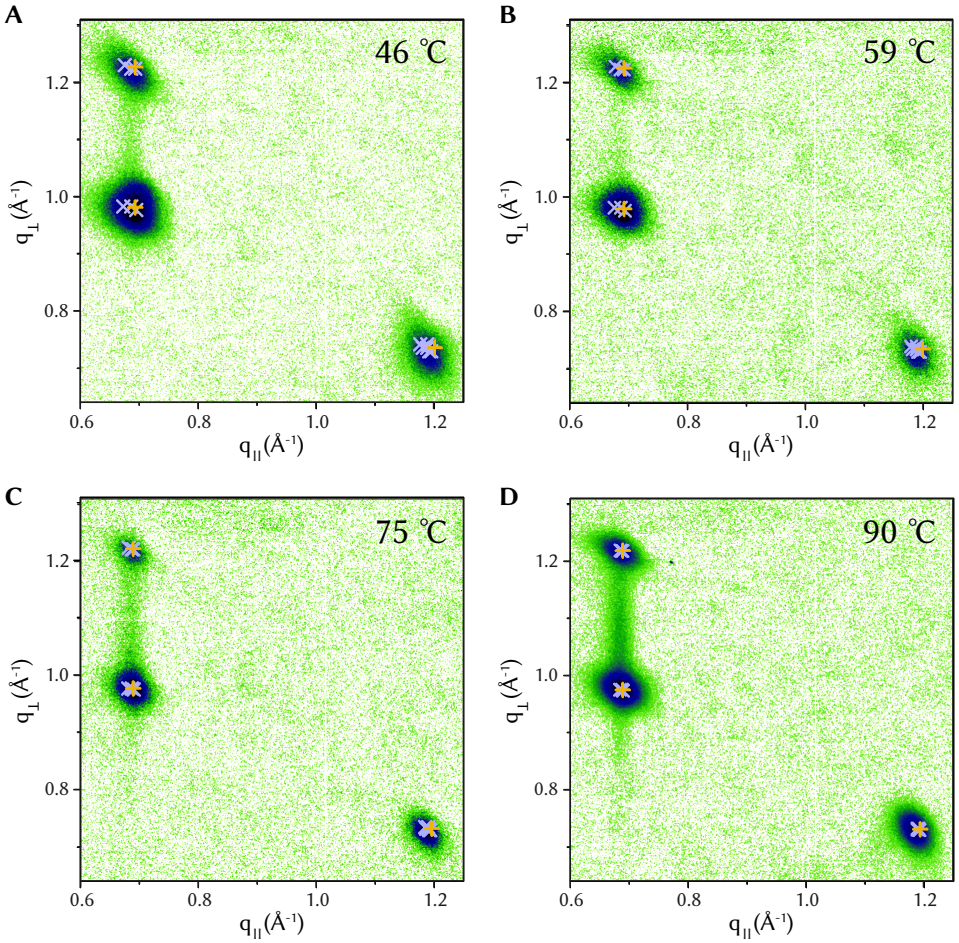

FIGURE 6.11: Comparison of GIWAXS data of a pentacene-C_{70} bilayers with the peak positions calculated for fcc structure (orange crosses) and rhombohedral structure (violet crosses) with the $[-111]$ direction parallel to the surface normal. **A** $T_D = 46\,°C$. **B** $T_D = 59\,°C$. **C** $T_D = 75\,°C$. **D** $T_D = 90\,°C$. Similarity of the calculated peak positions for fcc and rhombohedral increases with C_{70}-deposition temperature.

up to several peaks each, with their number depending on the multiplicity of the respective fcc peak. This splitting appears to correlate fairly well to the observed peak shapes in the entire q-range featuring observable C_{70} diffraction signal (see FIGURE 6.10 A). A close up on the three peaks corresponding to the cubic $(-3,1,1)$, $(-2,0,2)$ and $(-3,-1,1)$ peaks shown in FIGURE 6.10 B reveals that the rhombohedral model describes the peak positions of the data more accurately than the cubic model. It however overestimates the in-plain lattice spacing slightly.

FIGURE 6.11 A, B, C and D show the same q-range with the peak positions calculated for both the fcc and the rhombohedral model for the C_{70} layers deposited at 46 °C, 59 °C, 75 °C and 90 °C, respectively. As expected the two models show increasing similarity with increasing C_{70}-deposition temperature. For T_D = 105° they are identical by definition. Although the

rhombohedral model appears to describe all data sets better than the cubic one, a small discrepancy remains. This might indicate that the assumption that all grains in each investigated C_{70} layer are oriented exactly in [−111] direction oversimplifies the actual structural properties. It seems likely that the [−111] direction is tilted by a small angle with respect to the sample normal, which would also result in a different lattice angle corresponding to the out-of-plane lattice spacing. The tilt angle might well be dependent on the C_{70}-deposition temperature and could also vary from grain to grain. The latter would result in a broadening effect of the out-of-plain diffraction peaks that would be expected to decrease with increasing C_{70}-deposition temperature and increase with the scattering angle. Such a lateral inhomogeneity of the out-of-plane lattice spacings on the scale of individual grains constitutes a different type of disorder than paracrystallinity and can be expected to have different effects on the (opto)electronic properties of the films. As the paracrystallinity determination method of Hosemann does not separate these broadening effects, the paracrystallinity parameters determined in this work would have to be assumed to overestimate the actual paracrystallinity for low C_{70}-deposition temperatures if different orientations of a rhombohedral phase coexist.

A quantification of structural and orientational variations within the individual films would require an extensive fitting procedure that would exceed the scope of this work. It can however be considered a valuable follow up investigation, as it could facilitate a separation of the different types of disorder and thereby also allow for a more precise determination of the paracrystalline distortion.

6.1.4 *Deposition-rate dependency of the out-of-plane structure*

The C_{70}-deposition rate dependency of the structure of pentacene-C_{70} bilayers was investigated as described for temperature dependency in SECTION 6.1.1. Three samples with C_{70}-deposition rates between 0.05 Å s^{-1} and 0.18 Å s^{-1} were investigated. FIGURE 6.12 summarises the results. FIGURE 6.12 A seems to suggests a slight decrease of the lattice spacing with the deposition rate. The overall change of 0.4 % is however of comparable size as the standard errors ranging between 0.3 % and 0.4 %. The results for the pentacene lattice spacing (see FIGURE 6.12 B) show variations of a similar extent (0.4 %) and an average uncertainty of 0.5 %.

For the paracrystalline distortion parameter the experiment did not show a clear C_{70}-deposition rate dependency either. The variation of the paracrystalline distortion in C_{70} between 5.3 % and 5.9 % is of the same order of magnitude as the uncertainty of these values. Additionally an influence of

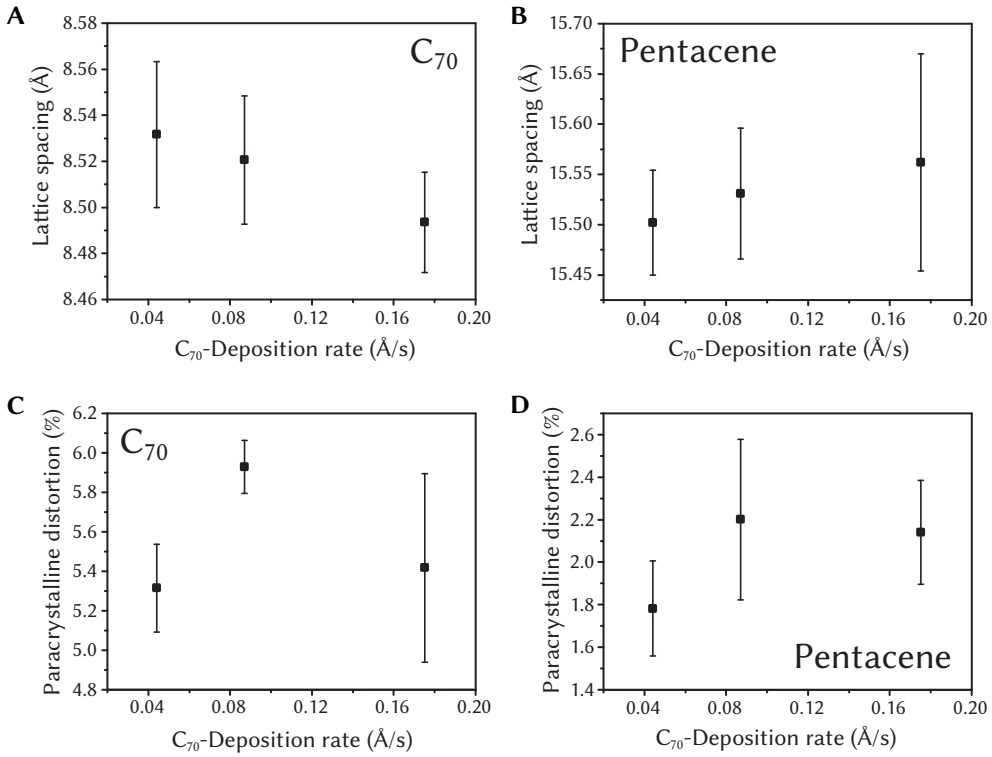

FIGURE 6.12: The C_{70}-deposition rate does not show a clear influence on the structure of the bilayers. In both layers the uncertainties of the analysis of the lattice spacing are larger or equal to the variations of the resulting values: **A** C_{70} lattice spacing. **B** Pentacene lattice spacing. **C** The variations of the paracrystalline distortion of C_{70} with the rate are much weaker than the dependence on the deposition temperature and might well depend on the quality of the pentacene film. **D** Paracrystalline distortion in the subjacent pentacene layers.

the paracrystallinity of the underlying pentacene film on the growth of the C_{70} layer has been suggested by the results described in SECTIONS 6.1.1 and 6.1.2. Due to large uncertainties of the paracrystalline distortion parameters of the pentacene layers (see FIGURE 6.12 D), it is infeasible to separate the actual influence of the C_{70}-deposition rate from preconditions given by the individual pentacene layer. Summarising it can be said that the C_{70}-deposition rate shows much weaker influence on the structure of the bilayers than the C_{70}-deposition temperature.

6.2 MORPHOLOGY OF C_{70} AGGREGATES ON PENTACENE

The morphology of C_{70} aggregates deposited onto pentacene thin films at different sample temperatures was investigated by grazing-incidence small-angle X-ray scattering (GISAXS). A nominal thickness of 8 Å of C_{70} was deposited onto 20 nm thick pentacene films, at different sample temperatures in the same deposition process as the respective bilayers prepared for structural investigation (see SECTION 4.1). GISAXS data were recorded and processed as described in SECTION 5.2.3. FIGURE 6.13 shows GISAXS patterns of C_{70} aggregates deposited onto pentacene at different temperatures as well as one of a bare pentacene thin film. The scattering signal from the pentacene film (FIGURE 6.13 A) exhibits two parallel stripes of high intensity along $q_{\parallel} \approx \pm\ 0.004\,\text{Å}^{-1}$. In the scattered intensity of pentacene films that were topped with C_{70} submonolayers, additionally two broader streaks appear along $q_{\parallel} \approx \pm\ 0.01\,\text{Å}^{-1}$. For higher C_{70}-deposition temperatures they are shifted to slightly higher $q_{\parallel}$-values, and therefore more clearly separated from the narrow streaks already observed for the pure pentacene film.

FIGURE 6.14 A shows in-plane line profiles that were extracted from the patterns shown above by averaging the intensity over $q_{\perp}$ in the range between $0.09\,\text{Å}^{-1} \leq q_{\perp} \leq 0.11\,\text{Å}^{-1}$. The positions of the peak centres were extracted, by fitting the curves by the sum of four Gaussian peaks. Dividing 2π by the peak positions gives a rough estimate about prevalently occurring distances in the sample [121]. FIGURE 6.14 B shows this parameter for the peaks close to $q_{\parallel} = 0.004\,\text{Å}^{-1}$, the ones corresponding to the broad peaks at higher $q_{\parallel}$-values are shown in FIGURE 6.14 C. For the interpretation of these plots, all the different features of the sample morphology that contribute to the scattering pattern need to be considered. In case of the pristine pentacene film two typical length scales are expected to influence the in-plane scattering signal: The distance of the typically pyramid shaped mounds as well as the width of the terraces formed by the individual monolayers [122]. Distances between individual pyramids are typically around 600 nm [107], corresponding to

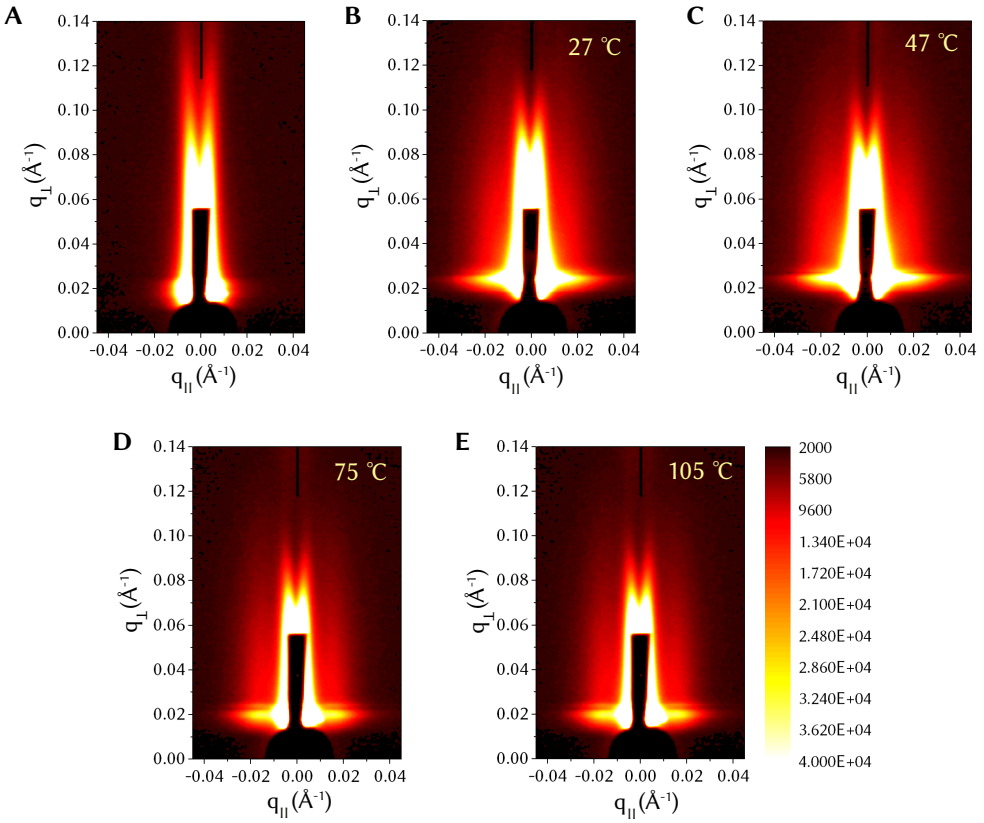

FIGURE 6.13: GISAXS patterns of pentacene thin films without and with C_{70} submonolayers deposited at different temperatures plotted against in-plane ($q_\parallel$) and out-of-plane momentum transfer ($q_\perp$). The scale bar shown in E is valid for all diagrams. The vertical black line at $q_\parallel = 0$ Å in the upper part of the patterns represents the area without data points, arising from the transformation to q-space. **A** The GISAXS pattern of a pristine pentacene film contains two parallel stripes of high intensity along $q_\parallel \approx \pm\ 0.004\,\text{Å}^{-1}$. **B-E** After depositing C_{70} with a nominal thickness of 8 Å onto pentacene at different temperatures, an additional pair of parallel streaks appears along $q_\parallel \approx \pm\ 0.01\,\text{Å}^{-1}$: **B** T_D = 27 °C. **C** T_D = 47 °C. **D** T_D = 75 °C. **E** T_D = 105 °C.

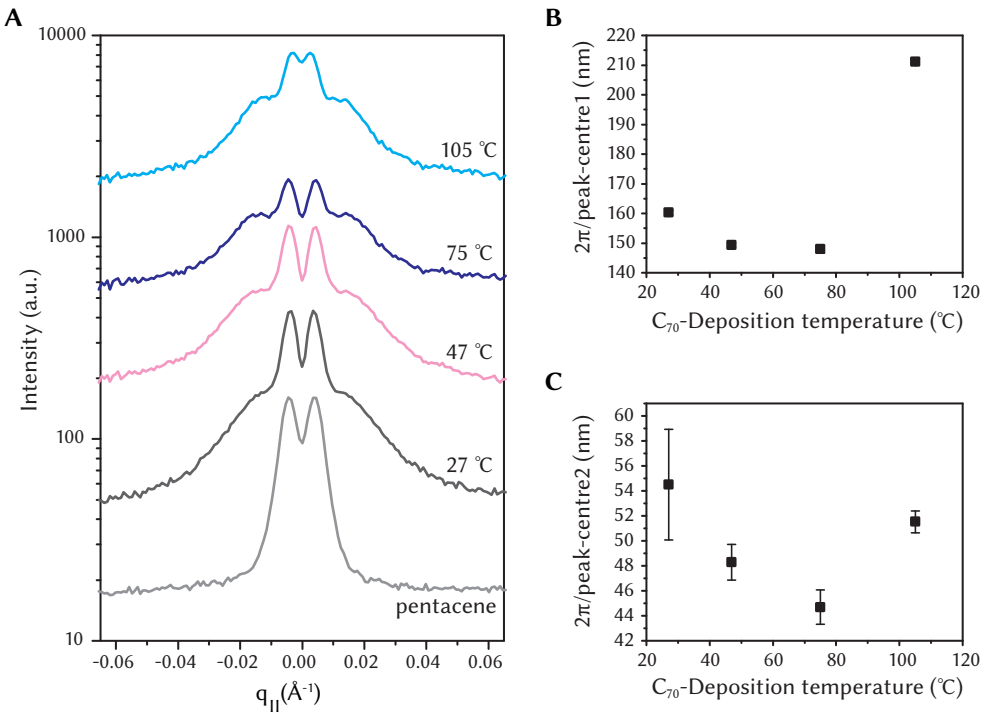

FIGURE 6.14: **A** In-plane line profiles extracted from the data presented in FIGURE 6.13 by averaging over $q_\perp$ in the range from 0.09 Å^{-1} to 0.11 Å^{-1}. Each curve was fitted by the sum of four Gaussian peaks. **B** and **C** Dividing 2π by the peak centres gives an estimation about characteristic distances occurring in the samples. Both quantities decrease for increasing C_{70}-deposition temperatures up to T_D = 75 °C (by 8 % in B and by 20 % in C) and increase again for T_D = 105 °C. Error bares solely comprise the propagated fit uncertainty.

$q_{\parallel} = 1 \times 10^{-3}\,\text{Å}^{-1}$, which is below the resolution of the presented data. Consequently the arrangement of the pentacene pyramids will together with their form factor increase the intensity close to $q_{\parallel} = 0\,\text{Å}^{-1}$. Due to the unknown shape and magnitude of the resulting central peak that underlies the resolved signal, the features can not be separated from each other. It should thus be noted that all observed peaks will be shifted towards smaller magnitudes of $q_{\parallel}$, while the effect can be expected to be larger for peak positions closer to $q_{\parallel} = 0\,\text{Å}^{-1}$. I.e. FIGURES 6.14 B and C have to be assumed to overestimate characteristic distances in the sample.

FIGURE 6.15 shows an AFM image of a C_{70} submonolayer deposited onto thin-film phase pentacene at 27 °C with a rate of $0.08\,\text{Å s}^{-1}$. It aids the interpretation of the GISAXS data, as two characteristic distances between C_{70} aggregates become evident. The majority of aggregates is located at the step edges and only few are found on the terraces between the step edges. Consequently the distance between two neighbouring aggregates on the same step edge is considerably smaller than the distance between two aggregates on neighbouring step edges. The blue line in FIGURE 6.15 illustrates this: Segment 1 and 3 follow along step edges, while in segment 2 the step edges are oriented almost perpendicular to the line. The average nearest neighbour distance of 27 nm found for segment 1 and 3 is much lower than the value of 73 nm obtained for segment 2. Note that these values measure the direct distances. In contrast the GISAXS measurement with an irradiated sample area of many square millimetres averages over virtually all possible grain orientations. They thus represent a much broader distribution of distances, and the values in FIGURE 6.14 B and C should be interpreted as average distances. This can however not explain the observed factor of ~2 between the distances indicated by GISAXS and AFM on its own. Additional statistical variations have to be taken into account, as individual AFM images provide low statistical relevance, especially as large variations of morphology can occur between individual pentacene films. The large extent of the discrepancy however suggests that the aforementioned impracticability of correction for the central background peak in the GISAXS profiles significantly affects the results shown in FIGURES 6.14 A and B. They will therefore only be discussed qualitatively.

The predominent accumulation at pentacen terrace step edges has been well investigated for C_{60}. Breuer and Witte [115] have observed almost homogeneous distribution of C_{60} aggregates deposited onto pentacene at 145 K. Increasing the deposition temperature resulted in a higher proportion of C_{60} aggregating at the step edges, up to complete step edge decoration at 240 K. Deposition at 345 K yielded fewer but larger aggregates, all located at step

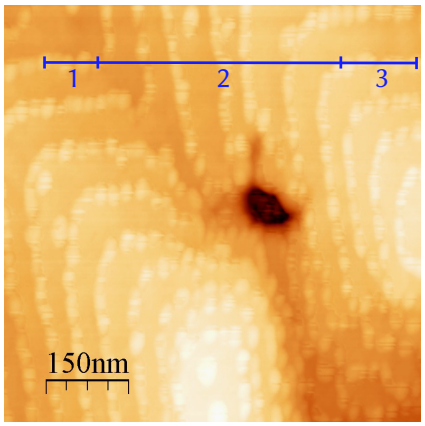

FIGURE 6.15: AFM image of a nominal layer thickness of 2 Å C_{70} deposited on pentacene at 27 °C. While a few aggregates are located on the pentacene terraces, the vast majority is observed at the step edges. Two characteristic distances between the C_{70} aggregates are found: the nearest neighbour distance in the lines along the step edges and the distance from one step edge to the next. Averaging the nearest neighbour distances in segment 1 and 3 of the blue line yields 27 nm, the aggregates in segment 2 have in average a distance of 73 nm to the next one on the line.

edges [115]. In this context the decrease of distance 2 (see FIGURE 6.14 C) with T_D up to 75 °C could be interpreted by an increasingly complete decoration of the terrace step edges which would result in the aggregates moving closer together along the step edges. The larger distance found for 105 °C could be explained by a trend to fewer aggregates, increasing the distance between them. Due to the lower symmetry of C_{70} it seems consistent that the entire evolution appears shifted to higher temperatures compared to C_{60}. Only the initial decrease of distance 1 (see FIGURE 6.14 B) is in conflict with this interpretation. With a maximum change of 8 % it is however less than half as pronounced as the change observed for distance 2 (20 %). Moreover possible variations of the terrace breadths of different samples have to be considered.

6.3 CONCLUSIONS AND SUMMARY

The data presented in this chapter indicates, that the C_{70}-deposition temperature can be used to tune the order in C_{70} layers grown on pentacene thin-film phase in a wide range. Paracrystalline distortion parameters between 2.3 % and 5.4 % were found. This inspires numerous experiments to investigate the relation between C_{70} crystallinity and electronic and optoelectronic properties, such as charge carrier mobility in ambipolar bilayer transistors or charge carrier separation efficiency at the pentacene-C_{70} interface. Especially for the latter, disconnected C_{70} grains as presented in SECTION 6.2 appear to be a promising study system, as they could aid to considerably reduce the number of unknown effects, such as processes at grain boundaries. The

results however also demonstrate, that in designing and interpreting such experiments extreme care is required to consider all relevant interrelations. This is illustrated by the observation that C_{70}-deposition temperature does not only affect the quality of the crystal but also the structure itself, and moreover influences morphology.

In the following the results from the different methods will be summarised, emphasising how closely the different structural properties are interrelated. The results presented in SECTION 6.1.1 suggest the following interpretation of the C_{70}-deposition temperature dependency of the disorder in C_{70}. Increased excess energy from sample heating results in increased order of the C_{70} film up to a temperature of about 75 °C. Further heating of the pentacene layer results in an initially slight distortion of the pentacene film, which hampers well ordered growth of the C_{70} layer, resulting in a monotonously increase of the paracrystalline distortion of the C_{70} film from this temperature on, until the diffraction signal is completely lost for a C_{70}-deposition temperature of 120 °C. It should be noted that the performed analyses can not exclude a coexistence of different crystallographic orientations within the C_{70} films. As this would contribute to the disorder quantified by the paracrystallinity calculation following the method of Hosemann, further analyses is required to verify if the values determined in this study can be interpreted to result solely from paracrystallinity (see also the end of SECTION 6.1.3). In both materials the disorder is not restricted to the out-of-plane direction, as GIWAXS data reveals. As the GIWAXS method only provides data for $q_{\parallel} \neq 0$, narrow out-of-plane peaks can not be observed with this technique. A high defect density can however cause considerable diffuse scattering around the out-of-plane peaks, which is known to occure in the pentacene thin-film phase [123]. In all the presented GIWAXS patterns diffuse scattering extends into the measured data range for the C_{70} (-111) diffraction and the first two orders of the pentacene thin-film phase (00L) diffractions. For T_D =105 °C even the third order of the pentacene out-of-plane diffractions is observed, i.e. it extends further than to $q_{\parallel}$ =0.08 Å^{-1}. This indicates that considerable lateral disorder occurs in both films and that the strongest disorder in the pentacene layers is found for the film onto which C_{70} was deposited at 105 °C.

For a C_{70}-deposition temperature of 105 °C, fcc growth with the out-of-plane lattice constant determined by the reflectivity measurements describes the GIWAXS data well. However, this model systematically and increasingly underestimates the in-plane dimensions of the C_{70} structure for lower C_{70}-deposition temperatures. The C_{70}-deposition temperature dependency of the out-of-plane lattice parameter thus has to result from a deformation of the

unit cell rather than a mere change of the cubic lattice parameter. An increasing rhombohedral distortion for decreasing C_{70}-deposition temperature seems to be a probable explanation for the observed trends. It is consistent with findings of Verheijen et al. who described a contineous transition between fcc and rhombohedral in C_{70} single crystals [119] as well as with the GIWAXS data presented in this work. The presented results are in line with the assumption that a continuous transition from fcc to rhombohedral structure with a predominent orientation of the long space diagonal of the unit cells parallel to the sample surface occurs for decreasing deposition temperatures. In this interpretation of the data the observed strong C_{70}-deposition temperature dependency of the out-of-plane lattice spacing (1.4 % change in a range of 80 K) translates to a comparably small change of the unit cell volume of 0.07 % in the investigated C_{70}-deposition temperature range of 80 K. This compares well to other organic molecules exhibiting different polymorphs. The difference between the volume of the pentacene thin-film phase and its bulk phase for comparison is 0.17 % [124].

The C_{70}-deposition temperature was also found to influence the morphology of disconnected C_{70} aggregates formed by deposition of low amounts of the fullerene onto thin-film phase pentacene. Interestingly, the smallest characteristic distance observed in GISAXS seems to be correlated to the crystallinity in the samples: It has a minimum at T_D = 75 °C, i.e. the C_{70}-deposition temperature with the lowest paracrystalline distoriton of the C_{70} film. The question if there is a causality between these trends remains open for investigation. The finding is however relevant on its own, as it has to be considered when planing experiments using disconnected C_{70} aggregates to investigate the influence of C_{70} crystallinity on optoelectronic properties.

7

METAL-HALIDE PEROVSKITES CONFINED IN NANOPOROUS THIN FILMS[1]

The work presented in this chapter was performed in collaboration with members of the Linz Institute of Organic Solar Cells and the Department of Soft Matter Physics of the Johannes Kepler University Linz (JKU). They developed a method to achieve blue-shifted emission from metal-halide perovskites by spatial confinement in nanoporous thin films. Two different materials were used as templates: electrochemically etched nanoporous silicon (npSi) and nanoporous anodic aluminium oxide (npAAO). Using npSi thin films yielded the largest blue shifts and allowed for tuning of the emission wavelength by using differently processed npSi films. Thin films of npAAO, on the other hand, have successfully been applied as active layers in light-emitting diodes (LEDs). A more detailed introduction to the project has been given in Section 2.2. In this chapter the results of an X-ray scattering study on perovskite filled npSi and npAAO thin films will be presented. Aim of the study was to investigate the structural properties, such as shape and size of the pores and the perovskite crystallites formed within them. The different types of perovskites that were investigated are methylammonium lead triiodide ($MAPbI_3$), methylammonium lead tribromide ($MAPbBr_3$) and caesium lead tribromide ($CsPbBr_3$).

7.1 NANOPOROUS SILICON THIN FILMS

Electrochemical etched npSi is well known for its sponge-like network of interconnected pores with radii tunable in the nanometre range [125, 126]. The material is thus highly interesting in terms of band-gap engineering of semiconductors by spatial confinement. Filling the pores is however very challenging, due to their small dimensions. Martin Kaltenbrunner and Stepan Demchyshyn have shown that this can be accomplished for metal halide perovskites by depositing the precursors in solution onto npSi layers by

1 This chapter has been partly adapted from [45] and [46].
Sample preparation and all optical characterisation were performed by Stepan Demchyshyn (JKU). The project was conceived and supervised at JKU by Martin Kaltenbrunner and Eric Daniel Głowacki.
The scattering data presented in this chapter were acquired at the beamlines P07 and P08 at DESY together with Anton Böhm, Kilian Frank, and Bert Nickel (LMU) and Florian Bertram, Ann-Christin Dippel, Olof Gutowski, and Uta Rütt (DESY).

spincoating and subsequent annealing of the sample [45]. By this method they achieve metal-halide perovskite nanoparticels with narrow band photoluminescence that is blue-shifted by up to 150 nm compared to the bulk material emission. One of the most compelling advantages of using npSi is that this material allows for pore size tunability by the choice of the anodisation current density. Thus, the photoluminescence peak wavelenghth of the metal-halide perovskites confined within the pores can also be tuned continuously by tuning the anodisation current density [45]. While the group in Linz had already found a linear correlation between anodisation current density and photoluminescence peak wavelength, the correlation to actual structural properties of the samples remained unclear. To fill this gap, we performed different X-ray scattering experiments. High-energy X-ray microbeam diffraction enabled an investigation of the structural properties of the perovskite nanoparticles at different depths within the nanoporous layers. These experiments were complemented by a SAXS analysis of an unfilled npSi layer. This allowed us to draw conclusions about how the formation of perovskite nanocrystals is affected by the template.

7.1.1 *Depth-resolved $MAPbI_3$ crystallite size*

To quantify the size of the perovskite crystallites that form in thin films of npSi, we used high-energy X-ray microbeam diffraction in transmission with the porous layers aligned parallel to the incoming beam (Figure 7.1). This measurement geometry has three compelling advantages. First, it facilitates strong signal, as a long beam path within the thin layers can be achieved by choosing sample lengths of many millimetres. This is possible due to the increased attenuation length at high energies, as has been illustrated in Section 3.3.2.2. Second, the method is sensitive to anisotropy, as information about the structures in the plane of the porous layer ($\parallel$ - indicated in red in Figure 7.1) and perpendicular to it (out-of-plane, $\perp$ - indicated in blue in Figure 7.1) can be accessed separately by analysing different parts of the diffraction pattern. Third, it allows for a depth-resolved analysis of size and amount of crystalline particles by moving the tens of µm thick porous layers stepwise vertically through the beamprofile of few µm FWHM.

The measurements were performed at the High Energy Materials Science Beamline P07 at DESY. WAXS depth profiles of four $MAPbI_3$ filled npSi layers (npSi/$MAPbI_3$) anodised at different current densities (5, 15, 25, and 30 mA cm^{-2}) were recorded to probe the influence of the anodisation current density on size and spatial distribution of the perovskite crystallites. Figures 7.2 A to D show the scattered intensity from the different $MAPbI_3$-

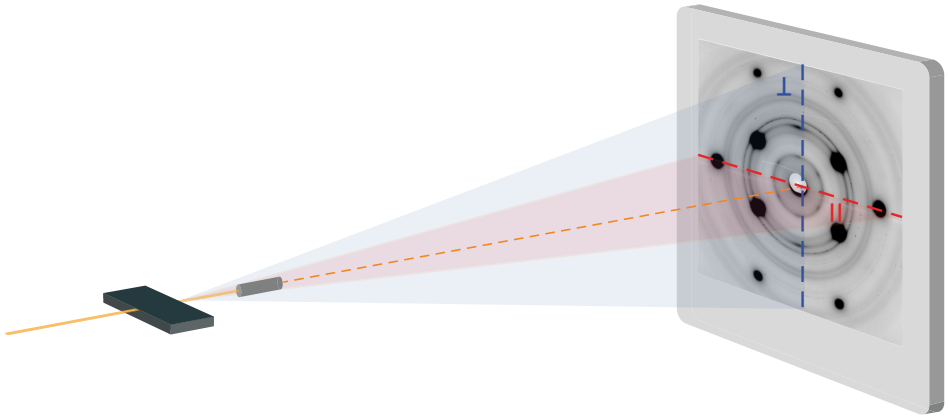

FIGURE 7.1: Sketch of the high-energy X-ray microbeam diffraction setup. The porous layer is aligned parallel to the incident beam (vertical FWHM 1.6 - 5 µm), which is blocked behind the sample. The scattered intensity is recorded by a 2d detector. Red (horizontal) and blue (vertical) dashed lines indicate the zones which are dominated by in-plane information (∥) and out-of-plane information (⊥) respectively. Adapted from [46].

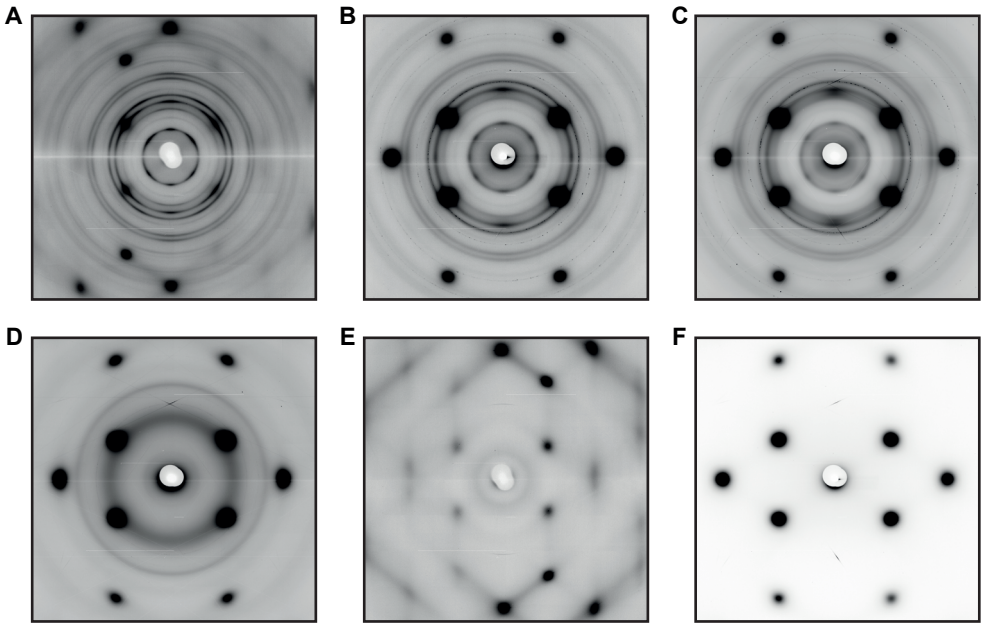

FIGURE 7.2: Diffraction patterns of npSi layers with and without $MAPbI_3$. **A** to **D**: Scattered intensity from differently prepared npSi layers infiltrated with $MAPbI_3$, recorded at the depth of maximum perovskite signal. The signal is a superposition of the background from the porous Si and continuous broad Debye-Scherrer rings from the perovskite crystallites within the pores. **A** $MAPbI_3$-infiltrated 30 mA cm^{-2} npSi measured 30 µm below the surface. **B** $MAPbI_3$-infiltrated 25 mA cm^{-2} npSi measured 25 µm below the surface. **C** $MAPbI_3$-infiltrated 15 mA cm^{-2} npSi measured 15 µm below the surface. **D** $MAPbI_3$-infiltrated 5 mA cm^{-2} npSi measured 6 µm below the surface. **E** and **F**: Reference measurements of npSi layers without perovskite. **E** 20 mA cm^{-2} npSi reference sample measured 30 µm below the surface during beamtime 1. **F** 15 mA cm^{-2} npSi reference sample measured 15 µm below the surface during beamtime 2. Partly adapted from [45].

infiltrated npSi layers, each recorded at the depth within the sample that provided the maximum perovskite signal. The obtained diffraction patterns are a superposition of the background due to the npSi and Debye-Scherrer rings of the perovskite crystallites within the pores. The regularly arranged broad peaks correspond to the crystal structure of <100> oriented Si [127] penetrated along the [110] direction. Due to the high X-ray energy the Ewald sphere has a very low curvature and thus intersects the reciprocal lattice in close proximity to several reciprocal lattice points. Thermal diffuse scattering and the finite thickness of the remaining Si between the pores led to strong peak broadening and consequently increased intensity in the recorded q-range. The appearance of Debye-Scherrer rings demonstrates that crystalline matter accumulated within the pores. All perovskite peaks are strongly broadened, indicating a small crystallite size. They are continuous over the entire circle, without obvious intensity variations, showing that all crystalline orientations occur.

7.1.1.1 *Data analysis and crystal structure*

To facilitate the removal of the background signal, reference patterns of npSi layers without perovskite were recorded at different depths below the surface at each beamtime. FIGURE 7.2 E shows an example of diffraction patterns of the reference sample measured with the same setup parameters as the 30 mA cm^{-2} npSi/$MAPbI_3$ sample. The reference diffraction pattern of a 15 mA cm^{-2} npSi layer probed 15 µm below the surface is shown in FIGURE 7.2 F. It was recorded with the same setup as the data of the 25 mA cm^{-2}, 15 mA cm^{-2} and 5 mA cm^{-2} npSi/$MAPbI_3$ samples and used for background correction of these data. A description of the background correction procedure is found in SECTION 5.2.4.

The $MAPbI_3$-infiltrated nanoporous layer anodised with 30 mA cm^{-2} and the respective reference sample were scanned in depth in steps of 10 µm. The real space resolution of the experiment was limited by the vertical FWHM of about 5 µm of the high-energy X-ray beam (98.5 keV) at sample position and additional uncertainty of the sample alignment that was typical for all investigated electrochemically etched silicon samples (see SECTION 5.2.4). Background corrected, azimuthally averaged intensity profiles are shown as a function of the momentum transfer q in FIGURE 7.3 for different depths below the surface. The peaks are indexed to a tetragonal structure with the lattice constants $a = b = 8.90 \pm 0.03$ Å and $c = 12.71 \pm 0.05$ Å (black vertical lines). These lattice constants match the literature values of Stoumpos et al [109], $a = b = 8.849 \pm 0.002$ Å and $c = 12.642 \pm 0.002$ Å within 0.6 %. Predominantly close to the surface additional sharp peaks appear (marked by

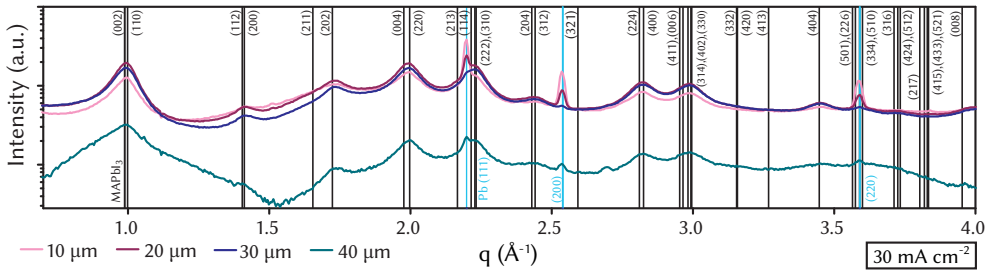

FIGURE 7.3: Background corrected, azimuthally averaged intensity of a $MAPbI_3$-infiltrated $30\,mA\,cm^{-2}$ npSi layer probed at different depths below the surface. Vertical lines indicate the peak positions expected for $MAPbI_3$ assuming a tetragonal structure with $a = b = 8.90 \pm 0.03$ Å and $c = 12.71 \pm 0.05$ Å (black) and face-centered cubic lead with $a = 4.9505$ Å (blue). Adapted from [45].

blue vertical lines), which can be attributed to traces of crystalline Pb.

The npSi layers anodised with $25\,mA\,cm^{-2}$, $15\,mA\,cm^{-2}$ and $5\,mA\,cm^{-2}$ are part of a second sample batch and were measured during a second beam time. The same measurement geometry was used, now with an X-ray energy of 80.0 keV and vertical FWHM of the beam of 2 µm, allowing us to scan the samples with a higher real space resolution. The background corrected, azimuthally averaged intensity profiles for different depths within the $MAPbI_3$ filled npSi layers etched with $25\,mA\,cm^{-2}$, $15\,mA\,cm^{-2}$ and $5\,mA\,cm^{-2}$ are shown in FIGURES 7.4 A, B and C, respectively. Even stronger broadening of the $MAPbI_3$ diffraction peaks is observed in these samples. Again Pb Bragg peaks appear, which decrease in intensity with increasing depth within the layer. Additional strongly broadened diffraction peaks appear primary close to the surface. Their signature is most pronounced in the diffraction profile recorded 5 µm below the surface of the $15\,mA\,cm^{-2}$ npSi/$MAPbI_3$ sample (dark grey line in FIGURE 7.4 B) and can be ascribed to lead(II) iodide (PbI_2). The peak positions calculated from the PbI_2 structure found by Wyckoff et al. [128] are marked by green vertical lines in FIGURES 7.4 A to C. For the $25\,mA\,cm^{-2}$ and $15\,mA\,cm^{-2}$ npSi/$MAPbI_3$ samples the perovskite signal was separated from this background for further analysis, as described in SECTION 5.2.4. The broadening of the diffraction peaks of the $5\,mA\,cm^{-2}$ npSi/$MAPbI_3$ sample was too strong to allow for a reliable separation of the $MAPbI_3$ and the PbI_2 signal. Hence, no further analysis of the diffraction data was performed for this sample.

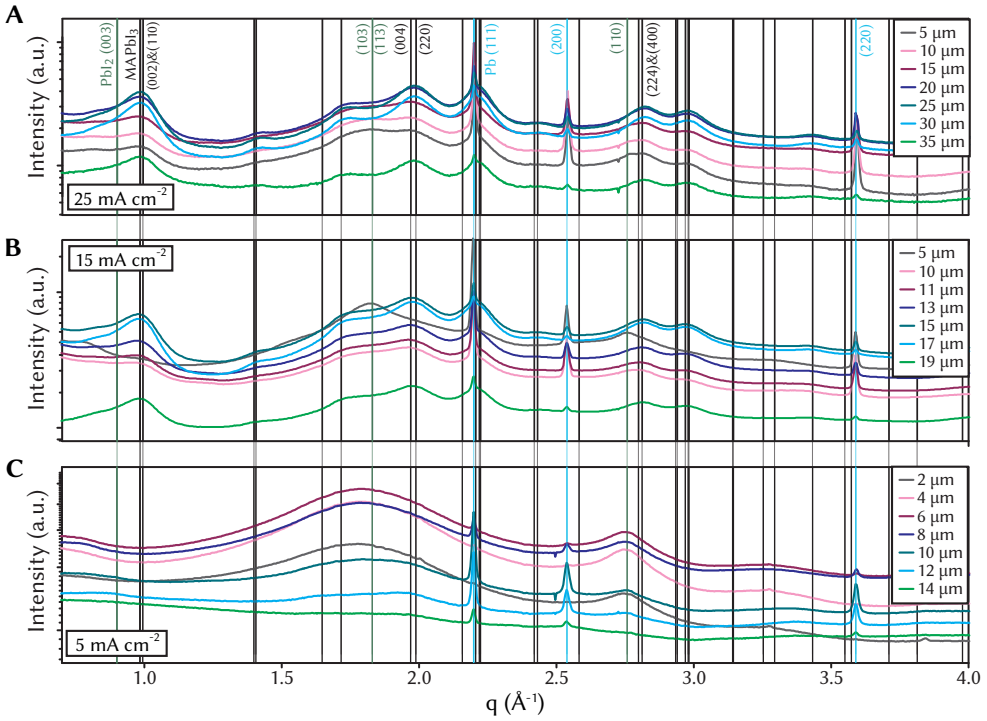

FIGURE 7.4: Background corrected, azimuthally averaged intensity of npSi layers that were anodised at different current densities plotted against the momentum transfer q. Several diffraction profiles recorded at different depths within the layers are shown for each sample. The peak broadening due to finite crystallite size increases with decreasing anodisation current densities. Vertical lines mark peak positions expected for $MAPbI_3$ (black), lead (blue) and PbI_2 (green). Partly adapted from [45]. **A** 25 mA cm^{-2} npSi/$MAPbI_3$. **B** 15 mA cm^{-2} npSi/$MAPbI_3$. **C** 5 mA cm^{-2} npSi/$MAPbI_3$.

7.1.1.2 *Depth-resolved crystallite sizes*

Using the Scherrer equation (EQUATION 3.6) [63], the depth-dependent crystallite size was calculated from the FWHM of the diffraction peaks (See SECTION 5.2.4 for details). The results are shown as red circles in FIGURES 7.5 A to C for the different anodisation current densities. The amount of perovskite material accumulating at a specific depth can be read off from the depth-dependent diffracted power (shown as black lines in FIGURE 7.5), that is, the normalised integrated intensity of the perovskite diffraction peaks. With a standard deviation of 3 Å in the 15 mA cm^{-2} and 25 mA cm^{-2} npSi layers and 4 Å in the 30 mA cm^{-2} npSi layer a rather narrow distribution of crystallite size versus depth is observed in all cases. The crystallite size was averaged over the whole layer thickness using the amount of $MAPbI_3$ at each specific depth as weight. The obtained average $MAPbI_3$ crystallite sizes are 1.8, 2.1, and 4.5 nm for 15, 25, and 30 mA cm^{-2} npSi, respectively. These values are depicted as red dashed lines in FIGURES 7.5 A to C.

It should be noted that the data does not allow to safely exclude any anisotropy of the crystallite shape or orientation. Analysing the data of separate sectors is strongly hampered by the superimposed broadened Si peaks as they render many data points unusable. This leads to a low signal to noise ratio and missing intensity values for considerable q-ranges in many sectors, causing increased uncertainties in the data analysis. A quantitative analysis was performed for the 15 mA cm^{-2} npSi/$MAPbI_3$ sample. The data was analysed for eight sectors with a width of 45° separately. The resulting low signal-to-noise ratio of the data led to an average uncertainty of the calculated crystallite size of 8 %. Within these limits of uncertainty of the analysis no significant difference between the in- and out-of-plane crystallite size was observed. It can thus be concluded that anisotropy of the shape of the crystallites formed in npSi is low.

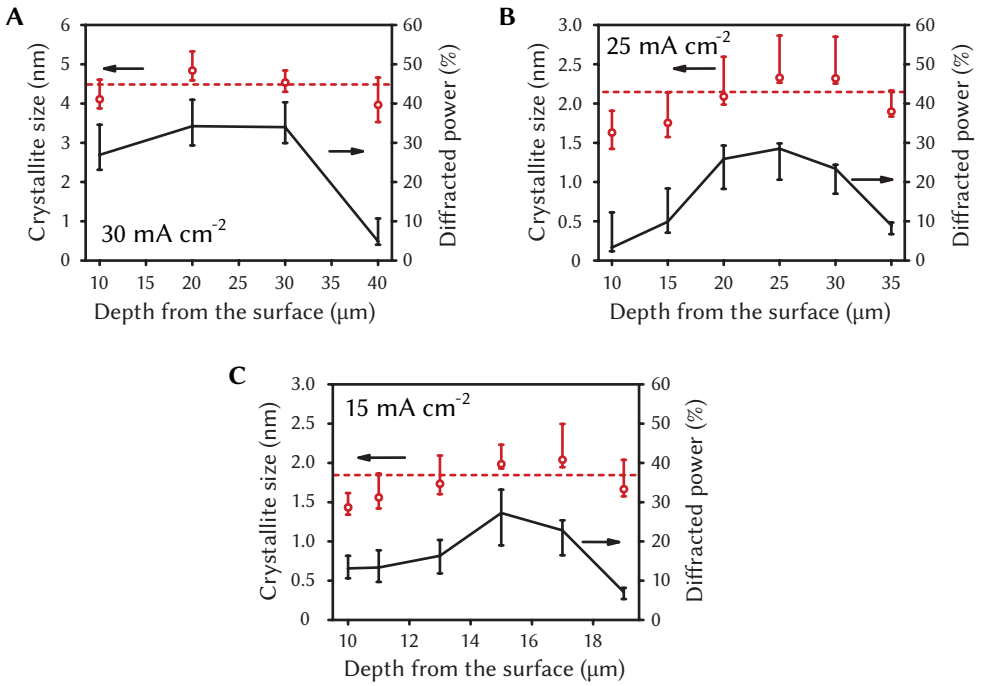

FIGURE 7.5: Crystallite size and diffracted power of the $MAPbI_3$ signal as function of depth for **A** 30 mA cm^{-2} npSi/$MAPbI_3$, **B** 25 mA cm^{-2} npSi/$MAPbI_3$, and **C** 15 mA cm^{-2} npSi/$MAPbI_3$. Red circles: Depth-dependent crystallite size. Black line: Normalised integrated intensity of the perovskite diffraction signal as a measure for the amount of perovskite at a specific depth. Dashed red line: Weighted average of the crystallite size. Error bars correspond to the 1-σ values of the uncertainty resulting from data analysis and the initial resolution of the experiment. Adapted from [45].

7.1.2 *Depth distribution of perovskite and residuals*

FIGURES 7.6 A to C illustrate where the different crystalline components are located in the porous layers. The amount of Pb residues at each depth (blue profile) is quantified by the integrated intensity of the Pb (200) diffraction. The PbI_2 signal strength is plotted in green. It is represented by the difference of the intensity of the two flanks of the $MAPbI_3$ (004)&(220) diffraction peak. The intensity at the low q flank is increased by the subjacent (103)&(113) PbI_2 diffraction peak, while the high q flank is not affected by scattering from PbI_2. It is, however, slightly increased by the neighbouring local maximum of the $MAPbI_3$ signal at $q \approx 2.21\,\text{Å}^{-1}$, which is caused by the merged $MAPbI_3$ diffractions from the (213), (114), (222), and (310) plane. Consequently, the difference between the intensity at the (103)&(113) PbI_2 position (q = $1.83\,\text{Å}^{-1}$) and the minimum intensity at q = $2.11\,\text{Å}^{-1}$ between the two neighbouring local maxima of the $MAPbI_3$ signal serves best as measure for the amount of PbI_2 at the respective depth of the layer. Although this parameter will underestimate the amount of PbI_2, it can serve as a qualitative measure to analyse its evolution with depth.

For comparison the $MAPbI_3$ diffracted power is shown in red. As an aid to orientation the qualitative depth dependency of the porosity of the layers is depicted in grey. It is represented by the integrated intensity originating from the broadened (311) Si peak. This constitutes a reasonable measure, as the decreasing thickness of the remaining pore walls causes increasingly strong broadening of the Si peaks for increasing porosities, causing them to extend further into the recorded part of the reciprocal space.

The results shown in FIGURES 7.6 A to C have an important implication for future device design concepts. While diffraction from Pb and PbI_2 residues

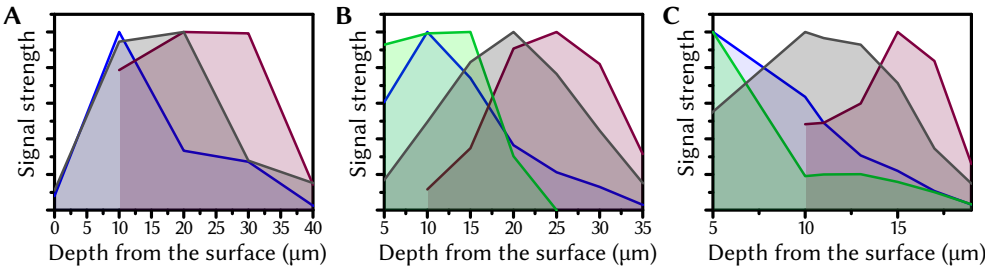

FIGURE 7.6: Signal strength of the crystalline substances in the samples as function of depth for **A** $30\,\text{mA cm}^{-2}$ npSi/$MAPbI_3$, **B** $25\,\text{mA cm}^{-2}$ npSi/$MAPbI_3$ and **C** $15\,\text{mA cm}^{-2}$ npSi/$MAPbI_3$. Dark red: Integrated intensity of the $MAPbI_3$ diffraction signal. Blue: Integrated intensity of the Pb (200) diffraction peak. Green: PbI_2 signal strength represented by the scaling factor used for the subtraction before the $MAPbI_3$ peak broadening analysis. Grey: Integrated intensity of the broadened (311) Si peak as a measure of the local porosity.

is strongest in the upper half of the npSi layers, the integrated intensity of the perovskite diffraction signal has a maximum in the lower half of the layer for all investigated samples. This strongly suggests to investigate possible methods to remove the upper part of the npSi layer and use the remaining - perovskite dominated - part for device fabrication.

7.1.3 *Relation of crystallite size to photoluminescence energy*

The average $MAPbI_3$ crystallite sizes of 1.8, 2.1, and 4.5 nm found in 15, 25, and 30 $mA\,cm^{-2}$ npSi, respectively, are comparable to, or lower than the values reported for the exciton Bohr diameter in $MAPbI_3$: Tanaka et al. found a Bohr diameter of 4.4 nm [129], Hirasawa et al. reported a value of 5.6 nm [130]. That the $MAPbI_3$ diffraction peaks of the 5 $mA\,cm^{-2}$ npSi sample were too broad to be analysed with the applied method suggests that even smaller crystallites were formed in these pores. Consequently, considerable blue shifts of the emission of the nanocrystals in all samples are expected. This is indeed observed, as photoluminescence (PL) spectra recorded by Stepan Demchyshyn reveal. Figure 7.7 A shows the PL spectra of the same samples that were subject to the X-ray analysis, with the exception of the 30 $mA\,cm^{-2}$ npSi sample, where the PL of a similarly prepared sample is shown. The PL of a bulk sample is plotted as a dashed line for comparison. An arrow indicates the direction of decreasing anodisation current density, which is expected to coincide with a decreasing pore size [125]. The PL emission is strongly blue-shifted for all samples. With a PL peak emission energy increased by 0.375 eV compared to the bulk sample, the 5 $mA\,cm^{-2}$ npSi sample shows the strongest blue shift. The PL peak emission energy increases with decreasing current density (Figure 7.7 B). The relation can be well approximated by a linear decrease of the PL peak emission energy with the anodisation current density with a slope of $-3.33\,meV/(mA\,cm^{-2})$. In Figure 7.7 C the PL peak emission energy is plotted against the average crystallite sizes obtained from the Scherrer analysis. It shows a strong increase of the PL emission energy with decreasing crystallite size as expected for the strong confinement regime [131].

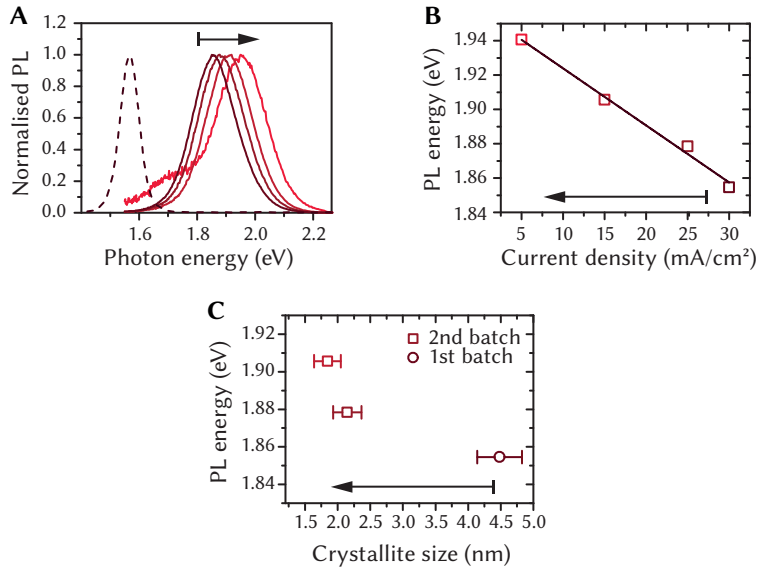

FIGURE 7.7: PL of $MAPbI_3$ nanocrystals in npSi. **A** Normalised PL of bulk $MAPbI_3$ (dashed line) and $MAPbI_3$ in npSi layers prepared at different current densities. From left to right: 30 mA cm^{-2}, 25 mA cm^{-2}, 15 mA cm^{-2}, 5 mA cm^{-2}. The data was kindly provided by Stepan Demchyshyn. **B** The PL peak emission energy shows a linear decrease with the current density used for npSi anodisation. **C** The PL peak emission energy shows a superlinear increase with decreasing crystallite size. Arrows indicate the direction of decreasing anodisation current density in all panels. Adapted from [45].

7.1.4 *Relation of pore to crystallite size*

Comparing the crystallite size of a $MAPbI_3$-infiltrated 15 mA cm^{-2} npSi film to the pore size of an empty npSi scaffold prepared under the same conditions provides information about the growth mode of the perovskite within the pores. Anton Böhm estimated the average pore diameter to be 4.0 nm following the method of Porod to analyse SAXS data (FIGURE 7.8) [45]. Comparing this with the results of crystal size analysis reveals that the formed perovskite nanocrystals are considerably smaller than the surrounding pores (1.8 nm versus 4.0 nm). Calculating the volume of perovskite precursor solution (11.8 vol%, see SECTION 4.2) needed to form a crystallite of the observed size shows that the volume of 1.5 spherical pores with a diameter of 4.0 nm is needed to form a cubic crystal with 1.8 nm edge length. Forming a spherical crystallite with 1.8 nm diameter requires a volume equivalent to 0.8 pores. These estimations encourage the concept that the pores act as weakly connected nanoreactors, which restrict the size of the perovskite crystallites below the pore size by providing a limited amount of precursor material. Due to this enhancement of the confinement, nanocrystals consisting of few unit cells only (e.g. 6 in the case of 15 mA cm^{-2} npSi) can be achieved, accounting for the strong PL blue-shifts in the npSi samples presented in SECTION 2.2 and SECTION 7.1.3. Based on the concept that the pores limit the reaction volume,

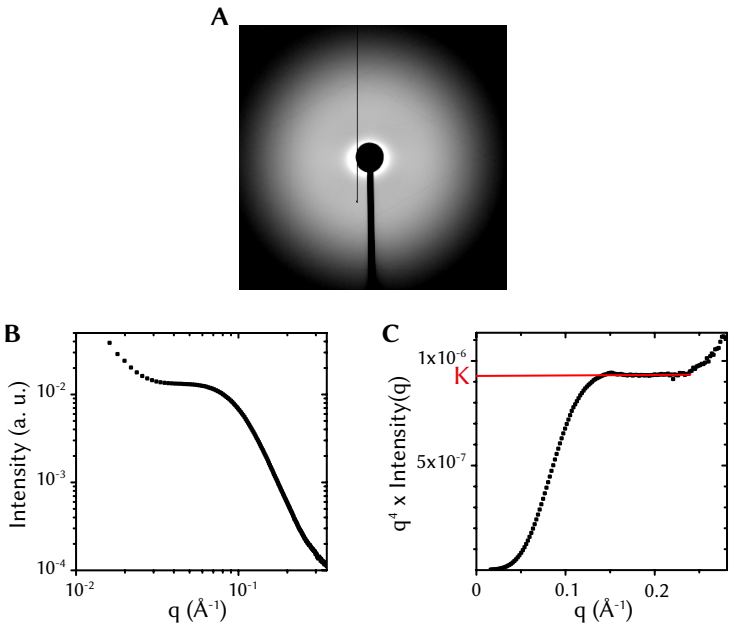

FIGURE 7.8: Porod analysis of SAXS data of a 15 mA cm^{-2} npSi film performed by Anton Böhm. **A** SAXS intensity pattern of a 15 mA cm^{-2} npSi layer recorded in transmission with an incident 20 keV beam parallel to the sample normal. **B** Azimuthally averaged intensity profile in double logarithmic representation. The region between q = 0.05 Å^{-1} and q = 0.24 Å^{-1} is dominated by the scattering signal of the nanopores. **C** The same data in the Porod representation. The Porod constant K is found by interpolating the plateau of the curve. Adapted from [45].

the concentration of the precursor solution can be expected to serve as a lever to further reduce the crystallite size by defining which proportion of the porous volume can be filled with perovskite.

7.1.5 *$MAPbBr_3$-infiltrated nanoporous silicon*

To investigate if different types of perovskite react differently to the confinement in npSi we analysed high-energy X-ray microbeam diffraction measurements of $MAPbBr_3$ in 25 mA cm^{-2} npSi. This perovskite material was chosen because it is known to crystallise in a cubic structure at room temperature [132]. For structures of lower symmetry diffractions from permutations of the same set of Miller indices occur at different scattering angles. This frequently causes peaks with slightly shifted positions to overlap, as observed in the diffraction profiles of $MAPbI_3$ crystallites in npSi (see FIGURES 7.3 and 7.4 in SECTION 7.1.1), where the effect significantly increased the uncertainties of the analysis. The cubic structure of $MAPbBr_3$ can thus be expected to allow for a more precise determination of the peak widths. For the same reason orientational anisotropy of the crystallite size is more easily accessible from diffraction data of cubic structures, making $MAPbBr_3$ a good choice for

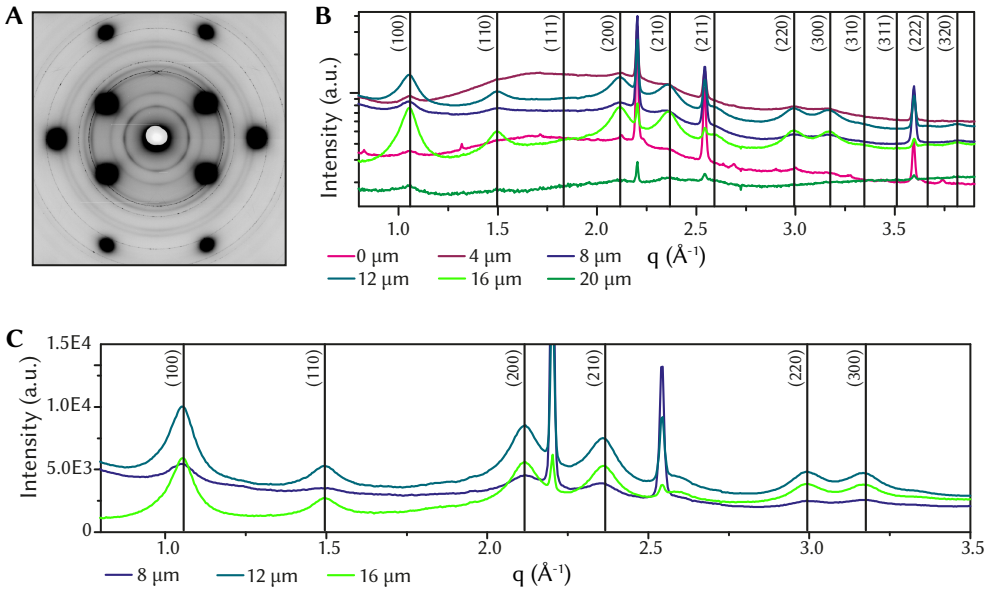

FIGURE 7.9: Diffracted intensity of a 25 mA cm^{-2} npSi layer infiltrated with $MAPbBr_3$. **A** Diffraction pattern recorded at the depth of maximum perovskite signal, i.e. 12 µm below the surface. **B** Azimuthally averaged intensity at different depths below the surface. At depths between 8 µm and 16 µm below the surface broadened perovskite peaks are clearly observed. They are indexed to a cubic structure with $a = 5.938$ Å. The sharp diffraction peaks at $q = 2.20$ Å^{-1} and $q = 2.54$ Å^{-1} correspond to crystalline Pb. Predominantly at the surface and 4 µm below a broad background is observed, that might result from residual perovskite precursor material. **C** Corrected perovskite signal measured 8 µm, 12 µm and 16 µm below the surface. The indexed peaks were analysed to quantify the crystallite size of the perovksite nanoparticles.

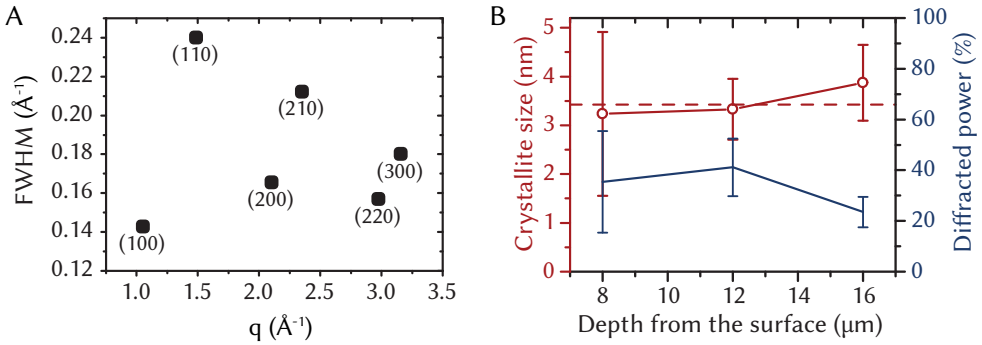

FIGURE 7.10: Diffraction peak widths and crystallite size of $MAPbBr_3$-infiltrated 25 mA cm^{-2} npSi. **A** The FWHM of the diffraction peaks vary considerably but show no clear trend with respect to q. **B** Estimation of the crystallite size according to Scherrer. The depth dependency of the size is shown as red circles, the dark blue line represents the diffracted intensity at each depth and acts as a measure for the amount of perovskite. Error bars correspond to the standard deviation of the results found for the six diffraction peaks. The red dashed line indicates the average crystallite size of the layer, taking the diffracted intensity into account.

addressing the question if there is a preferential direction of crystal growth.

Using the setup described in SECTION 7.1.1 a depth scan of the porous layer was performed. FIGURE 7.9 A shows the 2d diffraction pattern on the detector behind the sample at the measurement position with the strongest perovskite signal, i.e. at a depth of 12 µm below the surface. Azimuthally averaged diffraction profiles are shown in FIGURE 7.9 B for different depths within the layer. They have been corrected for the background from substrate, npSi and air as described in SECTION 5.2.4. Broadened perovskite peaks are observed, which can be indexed to a cubic crystal structure with a lattice constant of $a = 5.94$ Å. This is by 0.3 % larger than the cubic lattice spacing of 5.9195 Å found by Elbaz et al. [132] for bulk $MAPbBr_3$ at room temperature. Additional sharp diffraction peaks occur, which correspond to residual crystalline lead. The broad background that is observed for the measurements at the surface and 4 µm below suggests that this sample also contains some residual precursor material, in this case $PbBr_2$ and methylammonium bromide. The data were corrected for this additional background as described in SECTION 5.2.4.2. The resulting diffraction profiles are shown in FIGURE 7.9 C for the measurement positions which provided sufficient perovskite signal to allow for a reliable separation from the precursor background.

To quantify the crystallite size, the six perovskite peaks with the highest integrated intensity were fitted by the sum of six Gaussian peaks for each measurement. They are marked by vertical lines and their index in FIGURE 7.9 C. The FWHM from the measurement 12 µm below the surface are plotted against the magnitude of the scattering vector q in FIGURE 7.10 A. With a relative standard variation of 20 %, considerable variations of the peak

width are observed, showing neither a clear trend with respect to q, nor a consistent dependency on the crystallographic direction. Consequently, there is no significant indication of lattice strain, nor of a preferential growth direction. We therefore restrained the analysis to an estimation of the crystallite size following the Scherrer equation (EQUATION 3.6) [63] and averaged the results obtained from the FWHM of the different diffraction peaks irrespectively of their corresponding crystallographic direction. The associated standard deviation provides an estimation of the uncertainty of the analysis. The results are plotted in red against the depth within the layer in FIGURE 7.10 B. The integrated intensity of all fitted perovskite peaks, representing the diffracted power, is shown as dark blue line profile. These values are a measure for the amount of perovskite material at the respective depth and are used as weights to determine the average crystallite size of the layer, which is indicated by a red dashed line. With 3.4 nm and a standard deviation of 4 Å the size of $MAPbBr_3$ crystallites in 25 $mAcm^{-2}$ npSi lies between the values of 2.1 nm and 4.5 nm found for $MAPbI_3$ crystallites in 25 $mAcm^{-2}$ npSi and 30 $mAcm^{-2}$ npSi, respectively.

As the concentration of the precursor solution was slightly lower in the case of $MAPbBr_3$ (10.2 vol% vs. 11.8 vol% for $MAPbI_3$) a by 7 % smaller crystallite length would be expected for $MAPbBr_3$ if the two investigated perovskites react in the same way to the spatial limits inflicted by the pore walls and if the pore size in both samples can be assumed to be identical. The latter assumption might however not be justified, as large lateral inhomogeneities of the npSi films were discovered after the diffraction experiment had been performed. Analysing the profile of a 25 $mAcm^{-2}$ npSi film with scanning electron microscopy (SEM) revealed that the thickness of the nanoporous layer varies by at least 10 µm depending on the lateral position in the sample (see APPENDIX a.2). This might be indicative of an inhomogeneous current density, suggesting that lateral variations of the pore size and structure might likewise occur [56]. The fact that different background subtraction and fitting procedures were required for the two perovskites, additionally reduces comparability of the results. Thus, no clear conclusion about possible differences in the growth behaviour of different perovskites in npSi can be drawn from the existing data. In future diffraction experiments special care should be taken to perform all measurements at the same lateral position of the layers.

7.2 NANOPOROUS ANODIC ALUMINIUM OXIDE THIN FILMS

While perovskite nanoparticles within npSi proved to be challenging to address electrically, perovskite-infiltrated nanoporous anodic aluminium oxide (npAAO) thin films have been successfully used as active layers in LEDs. Their electroluminescence peak emission wavelength is blue-shifted compared to the corresponding bulk material by 60 nm and 12 nm for $MAPbI_3$ and for $CsPbBr_3$ respectively [45]. The npAAO scaffolds are electrically insulating before perovskite infusion, suggesting that in an operating device, electrons and holes move via the perovskite nanoparticles, when travelling across the active layer prior to recombination. Therefore, insights into the geometry of the perovskite nanoparticles and the pores are essential for understanding and improving device performance. In the following sections results of an investigation of these properties are presented, also addressing the question which nanoscale structural differences enable the integration of npAAO films into devices.

7.2.1 *Morphology of the nanoporous aluminium oxide films*

The morphology of the npAAO pore system was investigated by SAXS at beamline P08, DESY. A 870 nm thick npAAO film was prepared on a glass substrate as reported in SECTION 4.2.2. In order to quantify the average diameter of the pores ($2r_p$) and their nearest neighbour distance (D_p) the sample was measured in transmission mode with the X-ray beam along the surface normal (FIGURE 7.11 A). Details about the setup and data analysis are presented in SECTION 5.2.5. The intensity distribution recorded on a 2d detector behind the sample (FIGURE 7.11 B) is symmetric around the direct beam, indicating that shape and arrangement of the pores are isotropic within the plane of the sample surface. The azimuthally averaged signal is plotted against the magnitude of the scattering vector q in FIGURE 7.12 A as black circles.

A model to describe the SAXS intensity can be developed as described in the following paragraphs. We assume an arrangement of N cylindrical pores with their long axis predominantly aligned parallel to the incident X-ray beam of the intensity I_0, but allow for slight deviations of their orientation by integrating over a small angle range. The scattered intensity $I(q, \Delta)$ depends on the magnitude of the scattering vector q and the maximum deviation angle Δ of the axes of the cylinders as follows:

$$I(q,\Delta) = Constant \cdot I_0 \cdot \int_{\alpha'-\Delta}^{\alpha'+\Delta} d\alpha \sin\alpha \cdot S(q) \cdot \sum_{i=1}^{N} (\Delta\rho)^2 \cdot V_i^2 \cdot |F_i(q,\alpha)|^2 \quad (7.1)$$

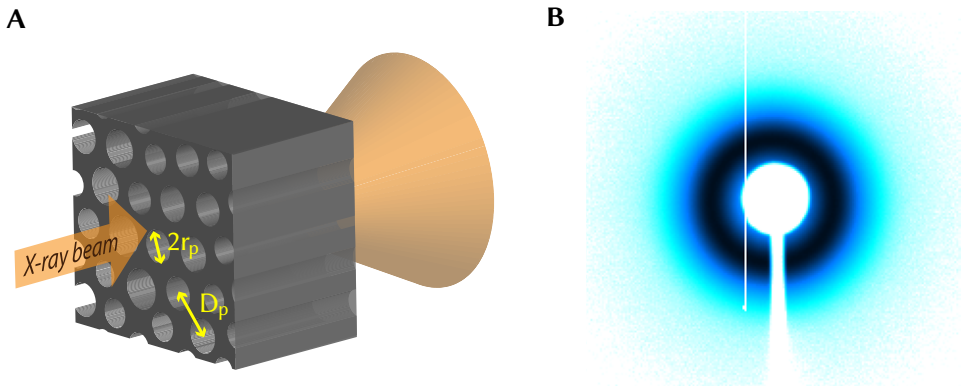

FIGURE 7.11: SAXS of a nanoporous aluminium oxide film. **A** Scheme of the SAXS scattering geometry. The sample is oriented perpendicular to the incident beam. Pore diameter ($2r_p$) and pore distance (D_p) are indicated. **B** SAXS intensity distribution on a 2d detector behind the sample. The symmetric distribution around the position of the incident beam indicates that the sample is isotropic within the plane of its surface. Adapted from [46].

Here α is the angle between the pore axis and the scattering vector, which reduces to $\alpha' = (\pi - 2\Theta)/2$ for pores that are parallel to the incoming beam. $S(q)$ is the structure factor, $\Delta\rho$ is the scattering length density difference between the aluminium oxide matrix surrounding the pores, and the air in the pores, V_i is the volume of pore i and $F_i(q, \alpha)$ is its form factor. The structure factor $S(q)$ corresponds to the spatial arrangement and distance of the pores, the form factor $F_i(q, \alpha)$ depends on the shape, size, and orientation of the respective pore (see SECTION 3.2.1). For cylindrical pores with radii r_i and equal lengths L volume and form factor are of the form:

$$V_i = \pi \cdot L \cdot r_i^2 \tag{7.2}$$

$$F_i(q, \alpha) = \left(\frac{2 \cdot \sin(q \cdot \cos\alpha \cdot L/2)}{q \cdot \cos\alpha \cdot L/2} \right) \cdot \left(\frac{J_1(q \cdot \sin\alpha \cdot r_i)}{q \cdot \sin\alpha \cdot r_i} \right) \tag{7.3}$$

where J_1 is the first order Bessel function of the first kind [133]. In the following the first factor of EQUATION 7.3 will be referred to as axial factor and to the second factor as cross-sectional factor.

To account for polydispersity, a weighted average of the form factors of differently sized pores is introduced using a Gaussian probability density function $p(r_p)$ of the pore radius r_p:

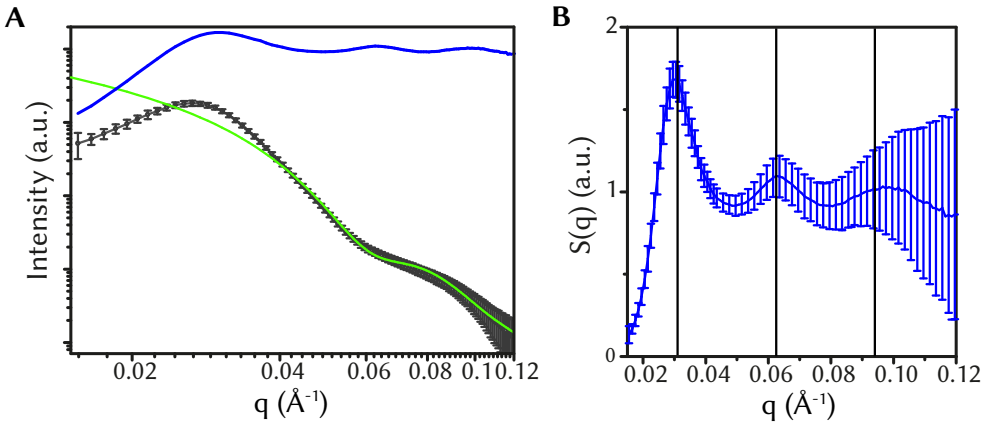

FIGURE 7.12: SAXS analysis of a nanoporous aluminium oxide film. **A** Double logarithmic plot of: the azimuthally averaged SAXS intensity $I(q)$ (black), the squared form factor $|F(q)|^2$, as calculated for slightly polydisperse cylindrical pores according to EQUATION 7.6 (green curve) and the structure factor $S(q)$ (blue curve) obtained by division of the measured intensity $I(q)$ by the calculated squared form factor $|F(q)|^2$. **B** The structure factor $S(q)$ in a linear plot. The periodicity marked by vertical lines corresponds to a characteristic interpore distance of 20 nm. Adapted from [46].

$$I(q,\Delta) = Constant \cdot I_0 \cdot \int_{\alpha'-\Delta}^{\alpha'+\Delta} d\alpha \sin\alpha \cdot S(q) \cdot L^2 \left(\frac{2 \cdot \sin(q \cdot \cos\alpha \cdot L/2)}{q \cdot \cos\alpha \cdot L/2} \right)^2 \cdot \sum_{r_p} p(r_p) \cdot \left(r_p \cdot \frac{J_1(q \cdot \sin\alpha \cdot r_p)}{q \cdot \sin\alpha} \right)^2 \cdot e^{-\sigma_p^2 \cdot q^2} \quad (7.4)$$

Here, pore wall roughness was accounted for by including a gradient of the scattering length density at the pore walls with the breadth σ_p as an exponential damping term as proposed by Engel et al. [133] and previously observed by Pépy et al. [134]. While slight variations of the pore alignment only have negligible effect on the cross-sectional factor [135], the result of the integration of the axial factor with respect to α can be approximated by q^{-1}. This step is discussed in the supplementary material of [46].

The intensity as a function of the magnitude of the scattering vector can thus be approximated by:

$$I(q) = Constant \cdot I_0 \cdot S(q) \cdot |F(q)|^2 \quad (7.5)$$

with the total squared form factor of the pores:

$$|F(q)|^2 = q^{-1} \cdot \sum_{r} p(r_p) \cdot \left(r \cdot \frac{J_1(q \cdot \sin\alpha \cdot r)}{q \cdot \sin\alpha} \right)^2 \cdot e^{-\sigma_p^2 \cdot q^2} \quad (7.6)$$

The green curve in FIGURE 7.12 shows EQUATION 7.6 for an average pore radius, pore size polydispersity, and pore wall roughness of $r_p = 5.85\,\text{nm}$,

$\sigma_r = 1.15\,\text{nm}$, and $\sigma_p = 0.5\,\text{nm}$, respectively. For $q > 0.04\,\text{Å}^{-1}$ it yields a satisfying agreement with the data. At smaller q-values a considerable deviation between the calculated $|F(q)|^2$ and the data is observed, suggesting that the scattering signal is affected by the pore arrangement, and the structure factor $S(q)$ has to be taken into account. For further analysis $S(q)$ was isolated from the measured intensity $I(q)$ by division, i.e. $S(q) = I(q)/|F(q)|^2$. It is shown as blue line in FIGURE 7.12 A. As expected, $S(q)$ approaches an average value of 1 for large q. In the linear plot in FIGURE 7.12 B a characteristic peak repeat distance of $\Delta q \approx 0.03\,\text{Å}^{-1}$ of the damped oszillations becomes evident, as indicated by vertical lines. This corresponds to a characteristic interpore distance of $D_p = (2\pi)/\Delta q = 20\,\text{nm}$. The FWHM of the first order peak FWHM_1 of $\sim 0.01\,\text{Å}^{-1}$ allows for an estimation of the lower limit of the correlation length ξ_p among different pores yielding $\xi_p = 2\pi/\text{FWHM}_1 = 65\,\text{nm}$. In summary the presented SAXS results are in agreement with the assumption that the investigated npAAO thin film exhibits regularly arranged tubular pores which are oriented almost parallel to the surface normal of the films with only a small angular divergence.

7.2.2 *Size and shape of the perovskite crystallites*

7.2.2.1 *Anisotropic crystallite size of $MAPbBr_3$ in npAAO*

To probe size and shape of $MAPbBr_3$ crystallites formed within the pores, high-energy X-ray microbeam wide-angle diffraction measurements were performed at beamline P07 at DESY. The ~1 µm thick nanoporous films were aligned parallel to the direct beam with a vertical FWHM of ~1.6 µm (FIGURE 7.13 A) and measured in transmission. This measurement geometry (FIGURE 7.1) enhanced the scattering signal and allowed for separated analysis of in-plane and out-of-plane signal, as described in SECTION 7.1.1.

FIGURE 7.13 B shows the intensity distribution on the detector for a npAAO layer filled with $MAPbBr_3$. It exhibits pronounced powder rings of the perovskite crystallites within the pores, clearly surmounting the background signal of substrate, npAAO template, and air scattering. The sample horizon is depicted as a red dashed line. It corresponds to the line that only contains in-plane information ($\parallel$), while the blue dashed line marks the zone that is dominated by out-of-plane scattering ($\perp$). Circular sectors with a width of $\pm$ 15° around these lines were analysed separately to probe for anisotropy of crystallite size and structure.

FIGURE 7.14 shows the background corrected azimuthally averaged data of the out-of-plane sector S_1 (blue dashed line) and the in-plane sector S_2 (red solid line). The diffraction profile corresponds to a cubic structure, in

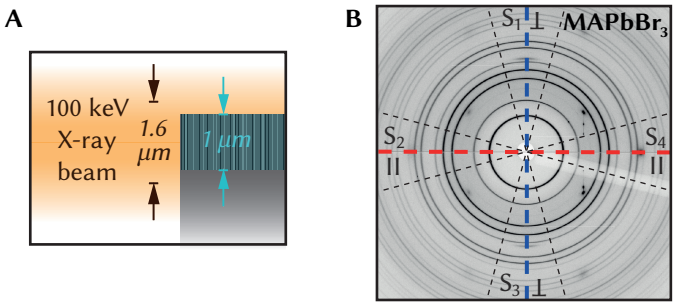

FIGURE 7.13: High-energy microfocus WAXS analysis of perovskite-infiltrated nanoporous aluminium oxide films. **A** Side view of scattering geometry: The ~100 keV X-ray beam is aligned parallel to the samples surface. With a FWHM of 1.6 µm it simultaneously probes the entire 1 µm thickness of the porous layer. **B** Diffracted intensity from a npAAO film infiltrated with $MAPbBr_3$ recorded at the sample position with maximum perovskite signal. Positions on the detector that are dominated by in-plane or out-of-plane information are marked by a red and a blue dashed line, respectively. Black dotted lines indicate the sectors that were used for further analysis. Adapted from [46].

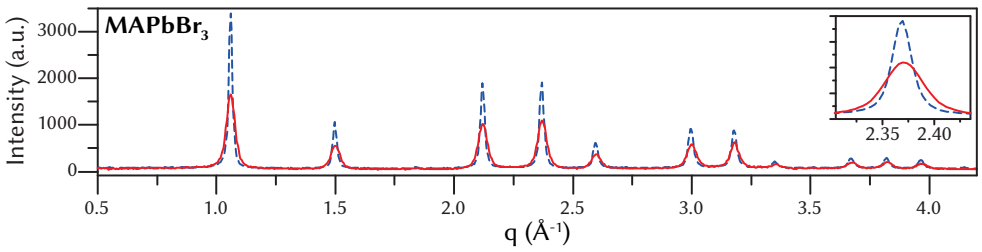

FIGURE 7.14: Azimuthally averaged background subtracted diffraction profiles of a $MAPbBr_3$-infiltrated npAAO layer probed at the depth of maximum perovskite signal. The out-of-plane signal obtained from sector S_1 is shown as blue dashed line, the in-plane signal obtained from sector S_2 as red solid line. The inset shows a magnification of the (210) diffraction and highlights the differently pronounced peak broadening of in- and out-of-plane signal, as well as the slight difference between the peak centres. Adapted from [46].

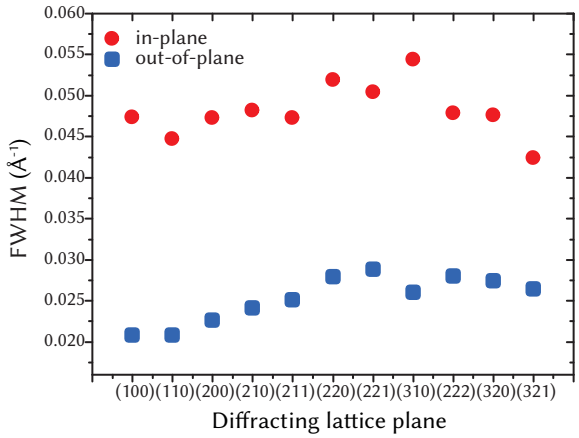

FIGURE 7.15: In-plane (red) and out-of-plane (blue) FWHM of diffraction peaks of $MAPbBr_3$ crystallites in npAAO sorted by the Bragg angle. The absence of a clear trend of the FWHM with the miller index suggests, that finite crystal size is the main contribution to the broadening of the peaks. Adapted from [46].

accordance with room temperature measurements on bulk $MAPbBr_3$ [132] and our analysis of $MAPbBr_3$ crystallites in npSi presented in SECTION 7.1.5. A strong anisotropy in peak width is observed, with the in-plane signal showing much stronger broadening than the out-of-plane signal. This becomes evident in the inset in FIGURE 7.14, which shows a magnification of the (210) diffraction. The in-plane peaks appear at slightly larger q-values than the equivalent out-of-plane peaks. This deviation suggests a minimal anisotropy of the lattice constant with respect to the direction in the sample. The effect is observed for all peaks, indicating that the symmetry of the crystal structure remains unaltered. Moreover, no indication for anisotropy of the crystallites orientation within the pores is found. There are neither obvious differences of the ratios of the intensity of the different diffractions between the in-plane and the out-of-plane signal (FIGURE 7.14), nor does FIGURE 7.13 B reveal azimuthal oscillations of the peak intensities between the sectors S_1 and S_2.

A quantitative analysis of crystallite size and lattice spacing was performed by fitting the diffraction profiles by the sum of 12 Gaussian peaks. Assuming cubic structure, the peak positions were expressed in terms of the lattice parameter a, which was varied in the fitting procedure. The 12 values for the FWHM of the peaks additionally served as fit parameters. FIGURE 7.15 shows the FWHM of the in- and out-of-plane peaks ordered by their Bragg angle. The values have been averaged over eight measurements at slightly shifted depths in the layer and over the two equivalent sectors of the 2d diffraction pattern. The corresponding diffraction profiles are shown in FIGURE a.3 in the APPENDIX a.3.1. The (111) peak is omitted in FIGURE 7.15 and further analysis, as the FWHM found by the fits and their standard errors were of the same order of magnitude for this peak. No systematic increase of

the peak width with the Miller index is observed. This indicates that finite size effects are the main contribution to the peak broadening, justifying the neglection of lattice strain effects. The crystallite size was calculated according to the Scherrer equation (Equation 3.6) [63] using the peak positions and the FWHM after correction for instrumental broadening (see Section 5.2.4.4). The results calculated from the nine diffraction peaks with the lowest fit uncertainty were considered for each sector, and the in-plane and out-of-plane crystallite sizes were calculated for each sample position by averaging the respective values of both equivalent sectors each. Again averaging over eight measurements at slightly shifted sample positions yields a mean out-of-plane crystallite length of $L_\perp = 27 \pm 3\,\text{nm}$, while the corresponding in-plane value is $L_\parallel = 13 \pm 1\,\text{nm}$. Implications of this result will be discussed at the end of the following section and put into a broader context in Section 7.3. Analogously to the evaluation of the anisotropic crystallite size, the average lattice parameter was calculated separately for both directions in the sample, yielding an out-of-plane lattice parameter of $a_\perp = 5.931 \pm 0.001\,\text{Å}$ and an in-plane lattice parameter of $a_\parallel = 5.926 \pm 0.001\,\text{Å}$. This indicates that the lattice constant of $MAPbBr_3$ crystallites in npAAO pores is slightly anisotropic (0.1 %) and marginally larger than the bulk constant $a = 5.9195 \pm 0.0001\,\text{Å}$ reported by Elbaz et al. (by 0.2 % and 0.1 % for $a_\perp$ and $a_\parallel$, respectively) [132].

7.2.2.2 *Anisotropic crystallite size of $CsPbBr_3$ in npAAO*

In order to investigate if the npAAO template affects the crystallite growth of different types of perovskite in the same manner, similar measurements as described in the previous Section 7.2.2.1 were performed on a ~1 µm thick npAAO layer filled with $CsPbBr_3$. The background corrected azimuthally averaged intensity profile at the sample position of maximum perovskite signal is shown in Figure 7.16. The respective raw data is shown in Figure a.4 in the Appendix a.3.2. The $CsPbBr_3$ nanoparticles exhibit an orthorhombic crystal

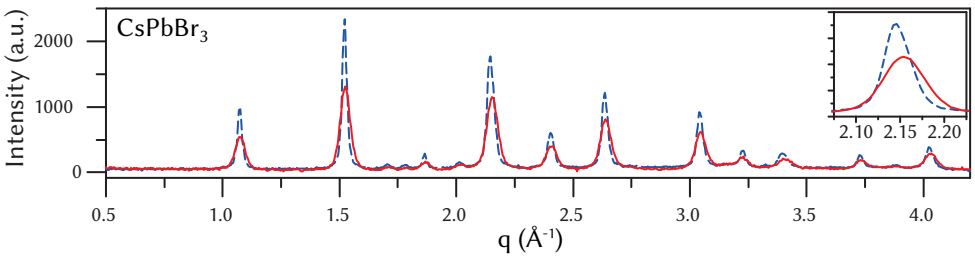

Figure 7.16: Azimuthally averaged background subtracted diffraction profiles of a npAAO layer infiltrated with $CsPbBr_3$ and probed at the depth of maximum perovskite signal. Blue dashed line: Out-of-plane signal obtained from the sector S_1. Red solid line: In-plane signal obtained from sector S_2. The inset shows the peak consisting of the (040) and (202) diffraction. Adapted from [46].

structure that resembles the structure found by Stoumpos et al. for room temperature measurements on bulk-like $CsPbBr_3$ [110]. For a quantitative analysis the two intensity maxima that are composed of only two diffraction peaks, i.e. $(020)\&(101)$ and $(040)\&(202)$, were fitted by a superposition of Gaussian peaks. The proportions of the three lattice parameters and the ratio of the areas under the superimposed individual diffraction peaks were kept fixed to the values expected for the structure described by reference Stoumpos et al. [110]. The peak positions were expressed as function of the lattice parameter a, which acted as a fit parameter. The FWHMs extracted from the fit were corrected for instrumental broadening, and together with the peak positions yield the crystallite size in the Scherrer approximation [63]. Averaging the results from all fitted diffractions for the three different sample positions and both equivalent sectors, respectively, yields an out-of-plane crystallite size of $L_\perp = 26 \pm 5\,\text{nm}$ and an in-plane crystallite size of $L_\parallel = 13 \pm 2\,\text{nm}$. The resulting average out-of-plane lattice parameter $a_\perp$ is $8.262 \pm 0.002\,\text{Å}$ and the in-plane lattice parameter $a_\parallel$ is $8.246 \pm 0.002\,\text{Å}$. This corresponds to a lattice parameter anisotropy of 0.2 %. Accordingly $b_\perp = 11.761 \pm 0.003\,\text{Å}$ and $b_\parallel = 11.738 \pm 0.003\,\text{Å}$ and $c_\perp = 8.216 \pm 0.002\,\text{Å}$ and $c_\parallel = 8.200 \pm 0.002\,\text{Å}$ can be calculated from the lattice parameter proportions that were kept fixed in the fitting procedure.

The close match of crystallite size and shape of two different perovskites in identically processed npAAO films indicates, that using tubular aluminium oxide pores as template for crystallisation is an effective method to shape metal halide perovskite nanoparticles. The similarity of the observed lateral crystallite size and the pore diameter further support this conclusion. The high aspect ratio of crystallites formed within npAAO can be expected to be highly beneficial for the operation of npAAO based perovskite nanoparticle LEDs. The larger crystallite size along the pore axis makes continuous perovskite pathways across the active layer of a typical thickness of 40 nm more likely, thereby most probably favouring charge carrier transport and recombination. Simultaneously the reduced lateral dimension of the crystallites is small enough to account for the observed PL blue-shifts of 10 nm and 12 nm for $MAPbBr_3$ and $CsPbBr_3$ respectively [45]. The analysis indicated a slight anisotropy of the lattice parameters with respect to the directions in the nanoporous film for both investigated types of perovskite. With a relative difference of 0.1 % and 0.2 % this effect is however weak and it can not unambiguously excluded that it might be caused by a measurement artefact. Even if a real phenomenon it could be assumed to have minor relevance for the performance and optoelectronic properties of devices. The interested reader is referred to the discussion in Appendix a.3.3.

7.2.2.3 *Homogeneity of $MAPbBr_3$ crystallites over the depth in a npAAO layer*

A measurement series consisting of exposures at vertically shifted sample positions was performed for two main reasons. First, it increased the significance of the results reported in the previous sections. Moving the beam centre through the layer and averaging the results from these measurement positions ensured that all parts of the layer contributed equally to the obtained average values of the investigated parameters. Second, it provided information about possible inhomogeneities of the obtained parameters over the depth within the layer, which will be presented in this section.
It should be noted that it was not possible to exclusively probe only a part of the layer thickness at a time, as the FWHM of 1.6 µm exceeded the thickness of ~1 µm of the probed npAAO layers (see FIGURE 7.13 A). Consequently, in each diffraction profile the signal from different depths within the layer superimposes. Yet the sensitivity to certain depths within the layer varies from measurement to measurement, as the profile of the incident intensity within the layer is different in every exposure. Thus, drastic differences over the depth as e.g accumulation of bulk perovskite at the surface, can be expected to be revealed by the study. An overall range of 10 µm was scanned in 100 steps of 0.1 µm. FIGURE 7.17 gives an overview over the diffraction profiles of a $MAPbBr_3$-infiltrated npAAO film recorded in the 2 µm thick range that provided the strongest perovskite signal. For reasons of clarity only every third step of the scan is shown. The azimuthally averaged data of the out-of-plane sector S_1 as defined in FIGURE 7.13 B are represented by dashed lines; continuous lines correspond to the in-plane sector S_2. While the intensity of all peaks varies strongly with the depth, the two qualitative observations that were already pointed out in FIGURE 7.14 are made at all depths: The in-plane signal shows much stronger peak broadening than the out-of-plane signal, and the in-plane peaks appear at slightly higher q-values. These effects can be more easily observed in the magnification of the (210) diffraction shown in the inset in FIGURE 7.17 but occur in the same manner for all other diffractions.

The anisotropic crystallite size was determined for each measurement position as described in SECTION 7.2.2.1. FIGURES 7.18 A and B show the out-of-plane and in-plane results for the 20 measurement positions with the strongest $MAPbBr_3$ signal. Error bars correspond to the standard deviation of the 18 equivalent results (9 peakwidth values x 2 sectors each). These uncertainties are of comparable size or larger than the standard deviation of the size variations with the depth of 3.7 Å and 2.3 Å for the out-of-plane and in-plane results, respectively. Additionally considering the intensity profile of the incident beam, which limits the depth resolution and is illustrated in beige in FIGURE 7.18, and the thickness of the porous layer (indicated in

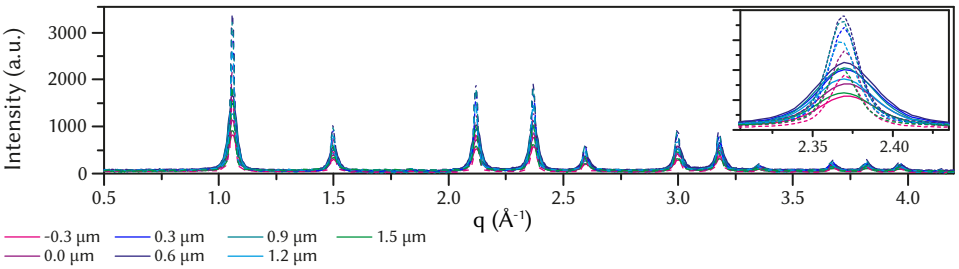

FIGURE 7.17: Azimuthally averaged background subtracted diffraction profiles of a $MAPbBr_3$-infiltrated npAAO layer probed at different depths. Dashed lines correspond to the out-of-plane sector S_1, solid lines to the in-plane sector S_2 . The inset shows the (210) diffraction. At all depth the in-plane peaks are broader than the out-of-plane peaks and slightly shifted to larger q-values. Adapted from [46].

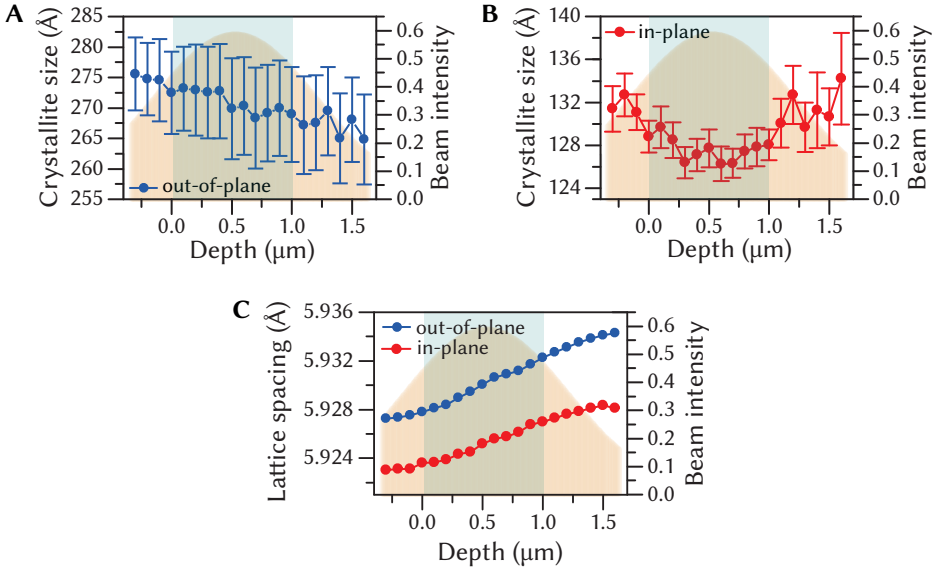

FIGURE 7.18: Crystallite size calculated at different sample depths. Sensitivity to inhomogenousity with the depth within the layer is accomplished by moving the sample vertically through the X-ray beam, whose intensity profile is indicated in beige. The FWHM of the beam of 1.6 µm exceeds the layer thickness of ~1 µm (indicated as turquoise shade). **A** and **B** Out-of-plane and in-plane crystallite size do not show variations exceeding the uncertainty of the experiment. Error bars correspond to the standard deviation of the averaging procedure. **C** Out-of-plane (blue) and in-plane lattice parameter (red) plotted against the depth within the layer.

turquoise), it is evident that the accuracy of the analysis only suffices to reveal drastic changes with depth. As this is not observed we can exclude accumulation of bulk material on top of the layer. The same limitations of the spatial resolution have to be considered when probing for a depth dependency of the lattice parameter a. In FIGURE 7.18 C, the depth variation of the average out-of-plane lattice parameter $a_\perp$ and in-plane lattice parameter $a_\parallel$, each obtained from two equivalent sectors, are plotted in blue and red, respectively. Both lattice parameters appear to increase monotonously with the depth. In spite of the lack of a reliable measure of the uncertainty of the results, the steadiness of this increase might indicate that it corresponds to a real feature of the sample. Both parameters show an overall change of 0.1 % in the depicted depth range. This coincides with the relative difference between $a_\perp$ and $a_\parallel$. The observation thus motivates an assessment of the possibility that it could be caused by a measurement artefact, as well as a discussion about possible origins of a lattice parameter anisotropy. Both issues will be addressed in APPENDIX a.3.3. In the following section the findings that are directly relevant for the integration of perovskite-infiltrated nanoporous thin films into LEDs will be discussed, with the focus on the differences between npSi and npAAO.

7.3 COMPARISON OF THE TWO NANOPOROUS SYSTEMS AND CONCLUSIONS

To summarise, profound differences in the crystallisation behaviour of perovskites in npSi and npAAO were found. The presented SAXS results are in agreement with the assumption that npAAO thin films exhibit regularly arranged tubular pores which are oriented almost parallel to the surface normal of the films and exhibit only a small angular divergence. Perovskite crystallites forming within these pores were found to be anisotropically shaped. While the lateral crystallite growth appears to be directly restricted by the pore diameter, the crystallite length along the pore axis is about twice as large. This clearly distinguishes these samples from perovskite-infiltrated npSi, for which no anisotropy of the crystallite size could be observed. Although the fact that npAAO can easily be produced in tens of nanometres-thin layers is certainly a major contribution to the success of npAAO as template for perovskite nanoparticle LEDs, the observed promotion of elongated crystallites is an important advantage of the system. It therefore seems promising to focus future work on npAAO, aiming to improve pore size tunability in this material. As the high-energy WAXS results suggest that crystallites forming in npSi in all dimensions have a considerably smaller size than their surrounding pores, it seems very challanging to achieve a continuous

pathway for charge carriers to travel via the perovskite across the active layer. In npAAO in contrast, a further improvement of charge carrier transport and recombination seems feasible. It can be expected that the number of continuous paths spanning the active layer thickness could be strongly increased by using higher precursor concentrations. Providing an excess of precursor material and subsequently removing potential bulk accumulations from the top of the layers might even allow for almost complete pore-filling, as observed by Ashley et al. [136] for pore sizes of down to 50 nm.

Part IV

CONCLUSIONS AND OUTLOOK

8

SUMMARY AND CONCLUSIONS

This thesis provides detailed insights into the nanoscale structure of two material systems. In both systems the (opto)electronic properties are critically influenced by structure. In organic semiconductors such as the investigated pentacene and fullerene C_{70}, charge transport is known to depend strongly on crystal structure, defect density and grain size [17–20], and there is ongoing discussion about a crucial influence of fullerene crystallinity on the charge carrier separation efficiency at organic heterojunctions [43]. In perovskite-infiltrated nanoporous thin films, size and shape of the crystallites formed within the pores influence emission wavelength and charge transport in light-emitting diodes (LEDs) [45, 46, 137].

The disorder in C_{70} films deposited by sublimation onto thin-film phase pentacene was quantified for a set of different C_{70}-deposition temperatures. It was shown that disorder can be tuned in a wide range, even without exploiting the option of sample cooling. A minimum paracrystalline distortion of 2.3 % was observed for deposition at 75 °C, as determined from X-ray reflectivity measurements. For deposition at 25 °C a paracrystalline distortion of 5.4 % was found. These changes are accompanied by a continuous transition of the crystal structure. The out-of-plane lattice spacing was found to increase linearly with the C_{70}-deposition temperature. GIWAXS measurements support the assumption that C_{70} deposition at temperatures below 100 °C results in a rhombohedral phase with $\alpha < 90°$, where the lattice angle α increases with the C_{70}-deposition temperature, merging into a face-centred cubic structure for deposition at 105 °C. A GISAXS study suggests two characteristic spacings of disconnected C_{70}-aggregates produced by submonolayer deposition onto thin-film phase pentacene. With the help of atomic force microscopy these spacings were interpreted as the distance of aggregates along the pentacene step edges and perpendicular to them. These too are dependent on the C_{70}-deposition temperature. The work thus provides the required knowledge to prepare well-defined pentacene-C_{70} heterojunctions with tunable crystallinity in the fullerene domains. It likewise demonstrates how closely different structural aspects are correlated. This needs to be considered in design and interpretation of future experiments that should aim to shed light on the relation of optoelectronic and structural properties. A number of suggestions are discussed in Chapter 9.

The results on shape and size of metal-halide perovskite crystallites confined in nanoporous thin films contribute to a better understanding of how different templates affect the formation of nanocrystals in this rather novel method. This was accomplished by combining information about the morphologies of nanoporous silicon (npSi) and aluminium oxide (npAAO) obtained from SAXS data with a diffraction analysis of the perovskite crystallites confined within them. It was found that in sponge-like npSi the pores are by far larger than the average crystallite size, suggesting that the pores restrict the aggregate size to the amount of precursor material provided by the contained solution. Forming a methylammonium lead triiodide ($MAPbI_3$) crystallite of the observed average size of 1.8 nm requires the solution filling 0.8 pores of 4.0 nm diameter in average. This facilitates the growth of small crystallites, as low concentrations of precursor solutions can be expected to result in a further reduction of the crystallite size. The crystallite size in npSi was moreover found to depend on the anodisation current density used for pore formation, ranging from 1.8 nm in npSi etched at 15 $mAcm^{-2}$ to 4.5 nm for 30 $mAcm^{-2}$. Nanoporous silicon consequently offers versatile tunability of emission wavelength. While confinement in npAAO films also yields blue-shifted emission, tuning the magnitude of the shift has not been accomplished so far [45]. A SAXS analysis is in agreement with the presupposition from the literature that npAAO exhibits aligned cylindrical pores that are oriented along the surface normal of the film [54]. An average pore diameter of 12 nm was found. High-energy X-ray diffraction revealed that methylammonium lead tribromide ($MAPbBr_3$) and caesium lead tribromide ($CsPbBr_3$) exhibit almost identical crystallite size and shape when being confined in npAAO. For both materials an average in-plane crystallite size of 13 nm was found. The out-of-plane crystallite sizes were 27 nm and 26 nm in $MAPbI_3$ and $CsPbBr_3$, respectively. These findings suggest that the in-plane growth of the perovskites is restricted by the lateral cross section of the pore, while remaining precursor material can accumulate in out-of-plane direction. A comparison of the proposed growth mechanisms strongly indicates that the differences in the pore morphology of npSi and npAAO are a major reason why perovskite filled npAAO films have been successfully applied as active layers in LEDs, while comparable attempts with npSi have failed. The elongated pores in npAAO appear to facilitate anisotropic crystallite growth, quite likely providing some continuous conductive paths across typically few tens of micrometres-thick active layers. This does not seam achievable in npSi, as crystallite growth in npSi appears to be restricted to individual pores, making a spatial separation of the crystallites unavoidable in this template.

The variety of insights into different aspects of the nanostructure of the two material systems provided by this work illustrates the power of X-ray scattering as an analysis tool. By choosing an appropriate X-ray energy for the investigated material, the ratio between the cross sections of coherent scattering and photoelectric absorption can be adjusted to the requirements of the sample, the addressed question and the desired analysis method. An X-ray energy of 20 keV was well suited for the investigation of the carbon-based organic semiconductors that are generally associated with rather low photon-matter interaction. Here standard techniques, namely X-ray reflectivity, GIWAXS and GISAXS provided all data required to extract the relevant structural parameters. Heavy elements in lead-halide perovskites result in much stronger photon-matter interaction. This suggests the use of higher X-ray energies to achieve a suitable compromise between scattering signal and photoelectric absorption. Additionally employing aluminium compound refractive lenses to focus the beam down to a vertical cross section as small as 1.6 µm at sample position, enables a rather unusual but powerful measurement geometry. By measuring thin films in transmission with the beam parallel to their surface, strong diffraction signal can be gathered even from micrometre-thin films that contain only low amounts of the investigated material. Additional unique advantages of the method are its inherent suitability to analysing parameters in out-of-plane and in-plane directions separately from a single 2d detector exposure, as well as the option to scan samples in depth with a real space resolution defined by the beam width.

9

OUTLOOK

As discussed in Chapter 2, an experimental investigation of the influence of fullerene crystallinity on charge carrier separation efficiency at the heterojunction with a donor material could provide valuable information about this controversial topic. The detailed analysis of the tunability of the C_{70} crystallinity on thin-film phase pentacene provided in this work, constitutes an advantageous starting point for such investigations. Employing disconnected C_{70} aggregates can be highly recommended for this purpose, as this can be expected to result in a reduction of the complexity of the system by eliminating effects at C_{70} grain boundaries.

Another promising study that could build on this well-defined sample morphology could focus on the question of which interface-to-volume ratio yields the best balance of charge carrier separation, transport and recombination properties. In this context the presented GISAXS data of the sample morphology could be a beneficial basis. A thorough pre-characterisation of the individual samples by an imaging technique such as atomic force microscopy may enable a qualified choice of starting values and boundaries that could allow for successful fitting of the curves. In this case shape, size and distribution of the C_{70} grains would be accessible with high statistical significance from a single 2d scattering pattern.

Additional data about the relation of charge carrier transport and crystallinity could be accessed by in-situ measurements of ambipolar pentacene-C_{70} transistors during the deposition of the C_{70} layer for different deposition temperatures. If performed in the laboratory employed for this work, this would constitute a straightforward experiment, as the setup implemented during the project enables all required functions.

Follow-up research about confinement of perovskites in nanoporous films for the fabrication of LEDs should aim to further advance the npAAO-based approach, as efforts to achieve electrical addressability of npSi do not appear promising. The proposed growth mechanism of pervoskite crystallites in npAAO suggests that a further improvement of charge transport across the active layer could be achieved by improving the pore-filling ratio. To this end, testing the effect of higher precursor concentrations appears promising. Further, a more efficient exploitation of capillary and centrifugal forces might be achievable if an approach presented by Ashley et al. [136] for diameters

between 50 and 200 nm proves applicable to smaller pores. They report that a redissolvation step on rapidly rotating perovskite filled npAAO films followed by annealing resulted in recrystallisation with improved pore filling [136].

In order to achieve tunability of the emission wavelength of perovskites confined in npAAO different anodisation conditions could be employed. This should allow for precise tuning of the pore diameter down to 10 nm [55]. Additionally, methods to further reduce the pore size after anodisation should be explored, to enable tuning of the emission down to even shorter wavelengths. This could e.g. be accomplished by atomic-layer deposition [138].

The X-ray analysis method applied to the perovskite filled nanoporous films could be further advanced by the implementation of high-energy microfocus SAXS. This would allow for a separate analysis of the out-of-plane and in-plane scattering and depth-resolved probing of thin films analogously to the high-energy WAXS study presented in this work. Due to the associated smaller scattering angles, accessing small q-values is challenging in high-energy experiments. The same applies for achieving high q-resolution at small scattering angles, as is evident from Section 3.3.2.4. Suitably high q-resolution can however be accomplished by employing very large sample to detector distances, a feature that is now also available at beamline P07 at DESY.[1] For a further improvement of the resolution at low q it is advisable to choose a beamsize that is only as small as required to achieve the wanted spatial resolution, in order to keep beam divergence as low as possible.

1 personal communication, Olof Gutowski, Beamline Engineer at P07

Part V

APPENDIX

a

APPENDIX

A.1 X-RAY REFLECTIVITY OF C_{70} ON SIO_2

X-ray reflectivity measurements of C_{70} deposited onto silicon substrates with a 20 nm thick thermal SiO_2 layer are shown in FIGURE a.1. Different rates and substrate temperatures were investigated. No Bragg diffraction is observed, indicating amorphous growth of C_{70} on SiO_2. The narrow oscillations observable at $q < 0.4\,\text{Å}^{-1}$ are most likely Kiessig fringes [121] originating from the 20 nm thick thermal SiO_2 layer. The measurements were performed in the scope of my master's thesis using a molybdenum-anode-based in-house setup [139].

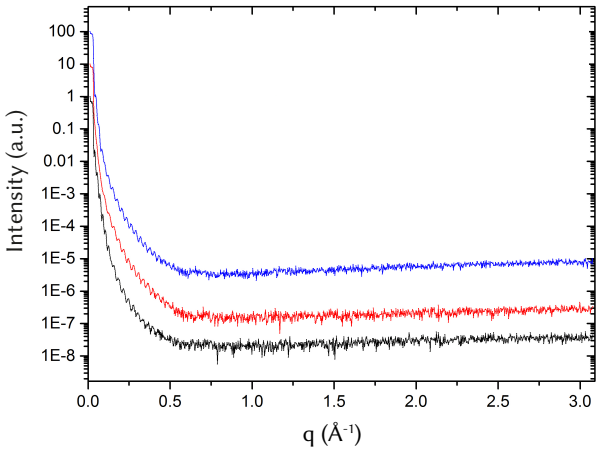

FIGURE A.1: X-ray reflectivity from C_{70} deposited onto SiO_2 using different vacuum deposition parameters. The black line corresponds to a layer thickness of 20 nm, a sample temperature of 25 °C, and a deposition rate of 0.03 Å/s, the red line to 16 nm, 100 °C, and 0.02 Å/s, and the blue line to 20 nm, 100 °C, and 0.15 Å/s. The curves have been normalised to 1, 10, and 100 for reasons of clarity. Adapted from [139].

A.2 INHOMOGENEITY OF NPSI LAYER THICKNESS

SEM revealed that the thickness of the porous layer of npSi etched at a current density of $25\,\text{mAcm}^{-2}$ shows large variations over the lateral position in the sample. FIGURES a.2 A and B show SEM images taken at different lateral positions in the beam. For the position shown in FIGURE a.2 A a thickness

of 26 µm was determined using the distance measurement function of the electron microscope. FIGURE a.2 B shows a position closer to the edge of the layer. Here a thickness of 16 µm was found. The micrographs were acquired with a LEO DSM-982 scanning electron microscope by Philip Altpeter at the Chair of Solid State Physics at LMU Munich.

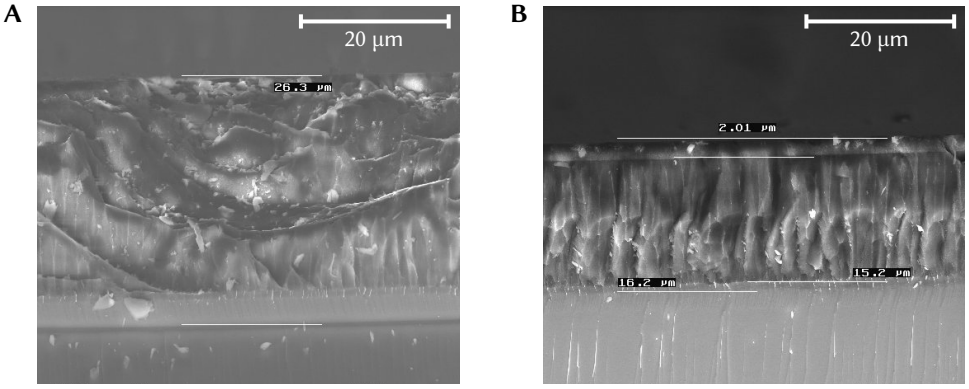

FIGURE a.2: SEM images of different lateral positions in a 25 mAcm^{-2} npSi layer. The scaling in both panels is identical. **A** Close to the centre of the layer a layer thickness of around 26 µm is found. **B** Closer to the edge of the sample the layer is only around 16 µm thick.

a.3 ADDITIONAL MATERIAL ON PEROVSKITES CONFINED IN NANOPOROUS ANODIC ALUMINIUM OXIDE

a.3.1 *Diffraction from $MAPbBr_3$ crystallites*

a.3.1.1 *Azimuthally averaged intensity from $MAPbBr_3$ confined in npAAO*

The diffraction profiles from the eight measurement positions which yielded the strongest perovskite signal are shown in FIGURE a.3 A. The out-of-plane data from sector S_1 are shown as dashed lines and the in-plane data from sector S_2 are shown as continuous lines. These profiles and the ones of their respective equivalent sectors were used to determine the average anisotropic crystallite sizes and lattice parameters.

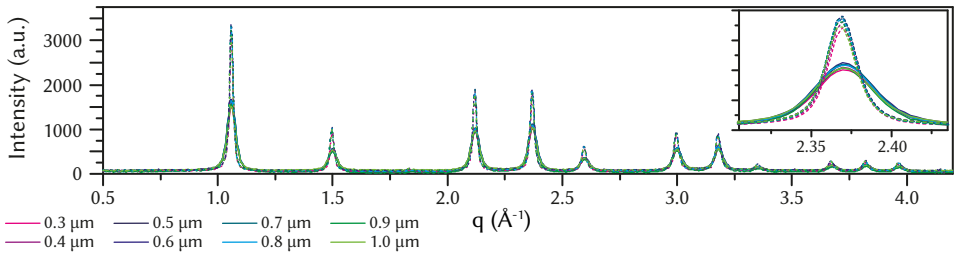

FIGURE A.3: Diffraction profiles of a npAAO film infiltrated with $MAPbBr_3$ probed at the eight measurement positions with the strongest perovskite signal. Dashed lines correspond to the intensity averaged azimuthally over the out-of-plane sector S_1, continuous lines correspond to the in-plane sector S_2. The inset shows the (210) peak. Adapted from [46].

A.3.2 *Diffraction from $CsPbBr_3$ crystallites*

The raw data that was used to determine the anisotropic crystallite size and lattice constant of $CsPbBr_3$ is shown in FIGURE A.4. As already observed for $MAPbBr_3$ crystallites in npAAO, the Debye-Scherrer rings are continuous without obvious graininess. This indicates that there is no predominant orientation of the crystallites within the pores.

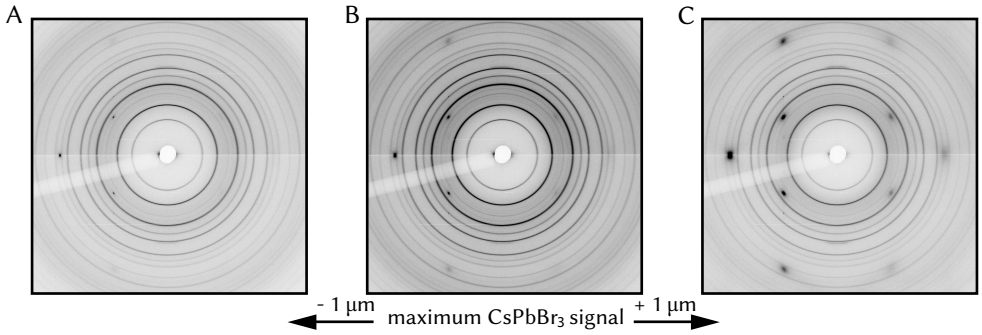

FIGURE A.4: Diffraction patterns of a npAAO film infiltrated with $CsPbBr_3$ probed 1 µm below the sample position of maximum perovskite signal (A), at the sample position of maximum perovskite signal (B) and 1 µm below it (C). Adapted from [46].

A.3.3 *Discussion of the lattice parameter anisotropy*

In this section the observations of anisotropic perovskite lattice constants in npAAO and their increase with the depth in the layer will be discussed. First, the question will be addressed, if the effects can be traced back to measurement artefacts. Subsequently possible causes for an anisotropy of the lattice parameter will be given.

Although it is infeasible to unambiguously prove that the observations are no artefacts of the method, many possible causes can be excluded. Analysing identically processed scattering data of a LaB_6 sample did not show any dif-

ference between in- and out-of-plane peak positions. Thus deficiencies of the calibration as e.g. an inadequate correction for detector tilts are not causing the anisotropy observed for the $MAPbBr_3$ peak positions. Consequently, it can be assumed to originate from the sample. This raises the question if the effect might result from refraction effects of the scattered X-ray beam occurring at the sample-air interface. Due to the low thickness of the porous layers the major part of the intensity scattered out of the plane of the sample surface exits the porous layer via its surface or bottom, while intensity scattered in the plane exits the layer exclusively at its end. Refraction effects would thus artificially decrease the scattering angles at which in-plane diffraction peaks appear. Scattered intensity exiting the sample at the top would be refracted to larger scattering angles, which would let the extracted lattice parameter $a_\perp$ appear smaller, i.e. the opposite of the observed effect would be expected. Thus, the difference of $a_\parallel$ and $a_\perp$ is most likely no artefact caused by refraction effects.

Accordingly it is worth considering the implications and possible origins of a lattice parameter anisotropy. The diffraction patterns of all sectors were in accordance with cubic crystal structure and no predominant orientation of the crystallites within the pores was observed (see Section 7.2.2.1). An anisotropic lattice parameter would thus imply that, independently of their orientation in the sample, the lattices of the crystallites were compressed in the dimensions that lie within the plane of the sample surface compared to the dimension perpendicular to it. This suggests that the anisotropy would be induced by the shape of the crystallites or the influence of the surrounding matrix. A divergence of the lattice parameter observed for nanoparticles in comparison to their bulk structure is common, as the high percentage of surface atoms increases the influence of surface effects as lattice relaxation [140–143]. An increased lattice parameter for nanoparticles has been predicted for many perovskites, including $CsPbBr_3$ [141] and $MAPbBr_3$ [142]. This is in line with the fact that we found lattice parameters that are slightly larger than the ones found for bulk structures in literature [110, 132]. However, such surface effects are most likely strongly influenced by the close environment, i.e. in our case the pore walls, which makes predictions difficult. Another effect on the lattice parameter might be given by the spatial confinement in the pores combined with thermal expansion of perovskite and the surrounding scaffold during the annealing process. If the precursor material assembles to nanoparticles in the pores before the substrate has reached its final annealing temperature and crystallisation happened in this latter stage, then the density of the precursor material would be anisotropic during crystallisation. This might explain the observed difference of in- and out-of-plane lattice constants in case the resulting crystal structure remained stable while the sample cools

down. Due to the high thermal expansion of the investigated perovskites, i.e. $33.3 \times 10^{-6}\,K^{-1}$ and $30.7 \times 10^{-6}\,K^{-1}$ for $MAPbBr_3$ and $CsPbBr_3$, respectively [144] [145], an expansion of about 0.3 % can be expected for the temperature difference of 95 K during the annealing process, which is sufficiently large to explain the observed difference of 0.1 % and 0.2 %. In this case the observed depth dependence of the lattice parameters might also result from squeezing effects during annealing: Assuming the porous layer with a linear thermal expansion coefficient of about $8 \times 10^{-6}\,K^{-1}$ [146] is firmly attached to the solid substrate with much lower thermal expansion (Si: $\sim 3 \times 10^{-6}\,K^{-1}$ [147]) it seems likely that the lateral expansion of the scaffold is larger on the top of the layer than on the bottom. Consequently, lateral pressure would decrease with the depth in the layer, i.e. the depth dependency of the in-plane lattice parameter could be attributed to this effect. The inhibited lateral expansion of the scaffold close to the substrate could then only be compensated in out-of-plane direction, providing additional space for the perovskite nanoparticles. It seems plausible that this could cause an increase of the out-of-plane lattice parameter with the depth.

LIST OF FIGURES

BIBLIOGRAPHY

[1] C. R. Poelking. "Organic Electronics in a Nutshell." In: *The (Non-)Local Density of States of Electronic Excitations in Organic Semiconductors*. Ed. by C. R. Poelking. Cham: Springer International Publishing, 2018, pp. 1–11. URL: https://doi.org/10.1007/978-3-319-69599-0_1.

[2] M. A. Green, A. Ho-Baillie, and H. J. Snaith. "The emergence of perovskite solar cells." In: *Nature Photonics* 8.7 (July 2014), pp. 506–514. DOI: 10.1038/NPHOTON.2014.134.

[3] L. X. Meng et al. "Organic and solution-processed tandem solar cells with 17.3% efficiency." In: *Science* 361.6407 (Sept. 2018), pp. 1094–1098. DOI: 10.1126/science.aat2612.

[4] M. I. H. Ansari, A. Qurashi, and M. K. Nazeeruddin. "Frontiers, opportunities, and challenges in perovskite solar cells: A critical review." In: *Journal of Photochemistry and Photobiology C-Photochemistry Reviews* 35 (June 2018), pp. 1–24. DOI: 10.1016/j.jphotochemrev.2017.11.002.

[5] S. Bauer, S. Bauer-Gogonea, I. Graz, M. Kaltenbrunner, C. Keplinger, and R. Schwödiauer. "25th Anniversary Article: A Soft Future: From Robots and Sensor Skin to Energy Harvesters." In: *Adv. Mater.* 26.1 (Jan. 2014), pp. 149–162. ISSN: 0935-9648. DOI: 10.1002/adma.201303349.

[6] Y. Q. Wong, H. Meng, H. Y. Wong, C. S. Tan, C. Wu, P. Tsai, C. Chang, S. Horng, and H. Zan. "Efficient semitransparent organic solar cells with good color perception and good color rendering by blade coating." In: *Organic Electronics* 43 (Apr. 2017), pp. 196–206. DOI: 10.1016/j.orgel.2017.01.003.

[7] M. Kaltenbrunner et al. "Flexible high power-per-weight perovskite solar cells with chromium oxide-metal contacts for improved stability in air." In: *Nature Materials* 14.10 (Oct. 2015), pp. 1032–1039. DOI: 10.1038/NMAT4388.

[8] B. Chen et al. "Efficient Semitransparent Perovskite Solar Cells for 23.0%-Efficiency Perovskite/Silicon Four-Terminal Tandem Cells." In: *Advanced Energy Materials* 6.19 (Oct. 2016), p. 1601128. DOI: 10.1002/aenm.201601128.

[9] C. O. R. Quiroz, C. Bronnbauer, I. Levchuk, Y. Hou, C. J. Brabec, and K. Forberich. "Coloring Semitransparent Perovskite Solar Cells via Dielectric Mirrors." In: *ACS Nano* 10.5 (May 2016), pp. 5104–5112. DOI: 10.1021/acsnano.6b00225.

[10] N. Yeh and P. Yeh. "Organic solar cells: Their developments and potentials." In: *Renewable & Sustainable Energy Reviews* 21 (May 2013), pp. 421–431. DOI: 10.1016/j.rser.2012.12.046.

[11] M. B. Upama, M. Wright, N. K. Elumalai, M. A. Mahmud, D. Wang, K. H. Chan, C. Xu, F. Hague, and A. Uddin. "High performance semitransparent organic solar cells with 5% PCE using non-patterned MoO3/Ag/MoO3 anode." In: *Current Applied Physics* 17.2 (Feb. 2017), pp. 298–305. DOI: 10.1016/j.cap.2016.12.010.

[12] Q. Xue et al. "Dual Interfacial Modifications Enable High Performance Semitransparent Perovskite Solar Cells with Large Open Circuit Voltage and Fill Factor." In: *Advanced Energy Materials* 7.9 (May 2017), p. 1602333. DOI: 10.1002/aenm.201602333.

[13] L. Protesescu, S. Yakunin, M. I. Bodnarchuk, F. Krieg, R. Caputo, C. H. Hendon, R. X. Yang, A. Walsh, and M. V. Kovalenko. "Nanocrystals of Cesium Lead Halide Perovskites (CsPbX3, X = Cl, Br, and I): Novel Optoelectronic Materials Showing Bright Emission with Wide Color Gamut." In: *Nano Letters* 15.6 (June 2015), pp. 3692–3696. DOI: 10.1021/nl5048779.

[14] Y. G. Rong, Y. Hu, A. Y. Mei, H. R. Tan, M. I. Saidaminov, S. I. Seok, M. D. McGehee, E. H. Sargent, and H. W. Han. "Challenges for commercializing perovskite solar cells." In: *Science* 361.6408 (Sept. 2018), eaat8235. DOI: 10.1126/science.aat8235.

[15] *NREL Best Research-Cell Efficiency Chart*. Access: 18 March 2019. URL: https://www.nrel.gov/pv/cell-efficiency.html.

[16] Z. Xiao, X. Jia, and L. M. Ding. "Ternary organic solar cells offer 14% power conversion efficiency." In: *Science Bulletin* 62.23 (Dec. 2017), pp. 1562–1564. DOI: 10.1016/j.scib.2017.11.003.

[17] G. Schweicher, Y. Olivier, V. Lemaur, and Y. H. Geerts. "What Currently Limits Charge Carrier Mobility in Crystals of Molecular Semiconductors?" In: *Israel Journal of Chemistry* 54.5-6 (June 2014), pp. 595–620. DOI: 10.1002/ijch.201400047.

[18] J. Fischer, J. Widmer, H. Kleemann, W. Tress, C. Koerner, M. Riede, K. Vandewal, and K. Leo. "A charge carrier transport model for donor-acceptor blend layers." In: *Journal of Applied Physics* 117.4 (Jan. 2015), p. 045501. DOI: 10.1063/1.4906561.

[19] S. M. O'Neill M.and Kelly. "Ordered Materials for Organic Electronics and Photonics." In: *Adv. Mater.* 23.5 (Feb. 2011), pp. 566–584. ISSN: 0935-9648. DOI: 10.1002/adma.201002884.

[20] H. C. Wang, Z. Bao, H. Y. Tsai, A. C. Tang, and R. S. Liu. "Perovskite Quantum Dots and Their Application in Light-Emitting Diodes." In: *Small* 14.1 (Jan. 2018), p. 1702433. DOI: 10.1002/smll.201702433.

[21] A. Gluchowski, K. L. G. Gray, S. N. Hood, and I. Kassal. "Increases in the Charge Separation Barrier in Organic Solar Cells Due to Delocalization." In: *Journal of Physical Chemistry Letters* 9.6 (Mar. 2018), pp. 1359–1364. DOI: 10.1021/acs.jpclett.8b00292.

[22] M. Casalegno, R. Pastore, J. Ide, R. Po, and G. Raos. "Origin of Charge Separation at Organic Photovoltaic Heterojunctions: A Mesoscale Quantum Mechanical View." In: *Journal of Physical Chemistry C* 121.31 (Aug. 2017), pp. 16693–16701. DOI: 10.1021/acs.jpcc.7b03640.

[23] M. Schwoerer and H.C. Wolf. *Organische Molekulare Festkörper: Einführung in die Physik von pi-Systemen*. Wiley, 2012.

[24] V. Coropceanu, J. Cornil, D. A. da Silva, Y. Olivier, R. Silbey, and J. L. Bredas. "Charge transport in organic semiconductors." In: *Chemical Reviews* 107.4 (Apr. 2007), pp. 926–952. DOI: 10.1021/cr050140x.

[25] P. Friederich et al. "Molecular Origin of the Charge Carrier Mobility in Small Molecule Organic Semiconductors." In: *Advanced Functional Materials* 26.31 (Aug. 2016), pp. 5757–5763. DOI: 10.1002/adfm.201601807.

[26] S. M. Ryno, M. K. Ravva, X. K. Chen, H. Y. Li, and J. L. Bredas. "Molecular Understanding of Fullerene - Electron Donor Interactions in Organic Solar Cells." In: *Advanced Energy Materials* 7.10 (May 2017), p. 1601370. DOI: 10.1002/aenm.201601370.

[27] B. Kippelen and J. L. Bredas. "Organic photovoltaics." In: *Energy & Environmental Science* 2 (Jan. 2009), pp. 251–261. DOI: 10.1039/b812502n.

[28] J. L. Bredas, J. E. Norton, J. Cornil, and V. Coropceanu. "Molecular Understanding of Organic Solar Cells: The Challenges." In: *Accounts of Chemical Research* 42.11 (Nov. 2009), pp. 1691–1699. DOI: 10.1021/ar900099h.

[29] A. Hinderhofer and F. Schreiber. "Organic-Organic Heterostructures: Concepts and Applications." In: *ChemPhysChem* 13.3 (Feb. 2012), pp. 628–643. DOI: 10.1002/cphc.201100737.

[30] H. Kang, G. Kim, J. Kim, S. Kwon, H. Kim, and K. Lee. "Bulk-Heterojunction Organic Solar Cells: Five Core Technologies for Their Commercialization." In: *Advanced Materials* 28.36 (Sept. 2016), pp. 7821–7861. DOI: 10.1002/adma.201601197.

[31] M. Linares et al. "On the Interface Dipole at the Pentacene-Fullerene Heterojunction: A Theoretical Study." In: *Journal of Physical Chemistry C* 114.7 (Feb. 2010), pp. 3215–3224. DOI: 10.1021/jp910005g.

[32] Y. T. Fu, C. Risko, and J. L. Bredas. "Intermixing at the Pentacene-Fullerene Bilayer Interface: A Molecular Dynamics Study." In: *Advanced Materials* 25.6 (Feb. 2013), pp. 878–882. DOI: 10.1002/adma.201203412.

[33] S. Joseph, M. K. Ravva, and J. L. Bredas. "Charge-Transfer Dynamics in the Lowest Excited State of a Pentacene-Fullerene Complex: Implications for Organic Solar Cells." In: *Journal of Physical Chemistry Letters* 8.20 (Oct. 2017), pp. 5171–5176. DOI: 10.1021/acs.jpclett.7b02049.

[34] J. Sakai, T. Taima, T. Yamanari, Y. Yoshida, A. Fujii, and M. Ozaki. "Pentacene:Fullerene Multilayer-Heterojunction Organic Photovoltaic Cells Fabricated by Alternating Evaporation Method." In: *Japanese Journal of Applied Physics* 49.3 (2010), p. 032301. DOI: 10.1143/JJAP.49.032301.

[35] S. Schiefer, M. Huth, A. Dobrinevski, and B. Nickel. "Determination of the crystal structure of substrate-induced pentacene polymorphs in fiber structured thin films." In: *Journal of the American Chemical Society* 129.34 (Aug. 2007), pp. 10316–10317. DOI: 10.1021/ja0730516.

[36] C. F. Macrae, I. J. Bruno, J. A. Chisholm, P. R. Edgington, P. McCabe, E. Pidcock, L. Rodriguez-Monge, R. Taylor, J. van de Streek, and P. A. Wood. "Mercury CSD 2.0 - new features for the visualization and investigation of crystal structures." In: *Journal of Applied Crystallography* 41 (Apr. 2008), pp. 466–470. DOI: 10.1107/S0021889807067908.

[37] *Molekülvisualisierung - Didaktik der Chemie - Universität Bayreuth*. Access: 16 March 2016. URL: http://daten.didaktikchemie.uni-bayreuth.de/3d_molekuele/structure_downl/inorg/c70.mol.

[38] Y. Sun, Q. Gong, S. Yang, Y.H. Zou, L. Fei, X. Zhou, and D. Qiang. "Optical limiting properties of buckminsterfullerene C60/C70." In: *Optics Communications* 102.3-4 (Oct. 1993), pp. 205–207. ISSN: 0030-4018. URL: http://www.sciencedirect.com/science/article/pii/003040189390382F.

[39] A. P. Isakina, A. I. Prokhvatilov, M. A. Strzhemechny, and K. A. Yagotintsev. "Structure, lattice parameters, and thermal expansion anisotropy of C70 fullerite." In: *Low Temperature Physics* 27.12 (2001), pp. 1037–1047. DOI: http://dx.doi.org/10.1063/1.1430849.

[40] A. A. Bakulin, A. Rao, V. G. Pavelyev, P. H. M. van Loosdrecht, M. S. Pshenichnikov, D. Niedzialek, J. Cornil, D. Beljonne, and R. H. Friend. "The Role of Driving Energy and Delocalized States for Charge Separation in Organic Semiconductors." In: *Science* 335.6074 (Mar. 2012), pp. 1340–1344. DOI: 10.1126/science.1217745.

[41] H. Tamura and I. Burghardt. "Ultrafast Charge Separation in Organic Photovoltaics Enhanced by Charge Delocalization and Vibronically Hot Exciton Dissociation." In: *Journal of the American Chemical Society* 135.44 (Nov. 2013), pp. 16364–16367. DOI: 10.1021/ja4093874.

[42] S. Gelinas, A. Rao, A. Kumar, S. L. Smith, A. W. Chin, J. Clark, T. S. van der Poll, G. C. Bazan, and R. H. Friend. "Ultrafast Long-Range Charge Separation in Organic Semiconductor Photovoltaic Diodes." In: *Science* 343.6170 (Jan. 2014), pp. 512–516. DOI: 10.1126/science.1246249.

[43] B. Bernardo, D. Cheyns, B. Verreet, R. D. Schaller, B. P. Rand, and N. C. Giebink. "Delocalization and dielectric screening of charge transfer states in organic photovoltaic cells." In: *Nature Communications* 5 (Feb. 2014), p. 3245. DOI: 10.1038/ncomms4245.

[44] G. D'Avino, Y. Olivier, L. Muccioli, and D. Beljonne. "Do charges delocalize over multiple molecules in fullerene derivatives?" In: *Journal of Materials Chemistry C* 4.17 (2016), pp. 3747–3756. DOI: 10.1039/c5tc03283k.

[45] S. Demchyshyn et al. "Confining metal-halide perovskites in nanoporous thin films." In: *Science Advances* 3.8 (Aug. 2017), e1700738. DOI: 10.1126/sciadv.1700738.

[46] J. M. Roemer, S. Demchyshyn, A. Böhm, O. Gutowski, K. Frank, N. S. Sariciftci, M. Kaltenbrunner, and B. Nickel. "X-ray study of anisotropically shaped metal halide perovskite nanoparticles in tubular pores." In: *Appl. Phys. Lett.* 113.25 (Dec. 2018), p. 251901. ISSN: 0003-6951. DOI: 10.1063/1.5054271.

[47] M. V. Kovalenko, L. Protesescu, and M. I. Bodnarchuk. "Properties and potential optoelectronic applications of lead halide perovskite nanocrystals." In: *Science* 358.6364 (Nov. 2017), pp. 745–750. DOI: 10.1126/science.aam7093.

[48] S. A. Veldhuis, P. P. Boix, N. Yantara, M. J. Li, T. C. Sum, N. Mathews, and S. G. Mhaisalkar. "Perovskite Materials for Light-Emitting Diodes and Lasers." In: *Advanced Materials* 28.32 (Aug. 2016), pp. 6804–6834. DOI: 10.1002/adma.201600669.

[49] A. Kostopoulou, E. Kymakis, and E. Stratakis. "Perovskite nanostructures for photovoltaic and energy storage devices." In: *Journal of Materials Chemistry A* 6.21 (June 2018), pp. 9765–9798. DOI: 10.1039/c8ta01964a.

[50] J. Zhang, X. K. Yang, H. Deng, K. K. Qiao, U. Farooq, M. Ishaq, F. Yi, H. Liu, J. Tang, and H. S. Song. "Low-Dimensional Halide Perovskites and Their Advanced Optoelectronic Applications." In: *Nano-micro Letters* 9.3 (July 2017), p. 36. DOI: 10.1007/s40820-017-0137-5.

[51] D. N. Dirin, L. Protesescu, D. Trummer, I. V. Kochetygov, S. Yakunin, F. Krumeich, N. P. Stadie, and M. V. Kovalenko. "Harnessing Defect-Tolerance at the Nanoscale: Highly Luminescent Lead Halide Perovskite Nanocrystals in Mesoporous Silica Matrixes." In: *Nano Letters* 16.9 (Sept. 2016), pp. 5866–5874. DOI: 10.1021/acs.nanolett.6b02688.

[52] H. C. Kwon, A. Kim, H. Lee, D. Lee, S. Jeong, and J. Moon. "Parallelized Nanopillar Perovskites for Semitransparent Solar Cells Using an Anodized Aluminum Oxide Scaffold." In: *Advanced Energy Materials* 6.20 (Oct. 2016), p. 1601055. DOI: 10.1002/aenm.201601055.

[53] V. Malgras, J. Henzie, T. Takei, and Y. Yamauchi. "Stable Blue Luminescent CsPbBr3 Perovskite Nanocrystals Confined in Mesoporous Thin Films." In: *Angewandte Chemie - International Edition* 57.29 (July 2018), pp. 8881–8885. DOI: 10.1002/anie.201802335.

[54] W. Lee and S. J. Park. "Porous Anodic Aluminum Oxide: Anodization and Templated Synthesis of Functional Nanostructures." In: *Chemical Reviews* 114.15 (Aug. 2014), pp. 7487–7556. DOI: 10.1021/cr500002z.

[55] A. M. M. Jani, D. Losic, and N. H. Voelcker. "Nanoporous anodic aluminium oxide: Advances in surface engineering and emerging applications." In: *Progress In Materials Science* 58.5 (June 2013), pp. 636–704. DOI: 10.1016/j.pmatsci.2013.01.002.

[56] M. J. Sailor. *Porous Silicon in Practice: Preparation, Characterization and Applications*. Wiley-VCH, 2012. DOI: DOI:10.1002/9783527641901.

[57] A. M. Hindeleh and R. Hosemann. "Paracrystals Representing the Physical State of Matter." In: *Journal of Physics C - Solid State Physics* 21.23 (Aug. 1988), pp. 4155–4170. DOI: 10.1088/0022-3719/21/23/004.

[58] A. M. Hindeleh and R. Hosemann. "Microparacrystals - the Intermediate Stage Between Crystalline and Amorphous." In: *Journal of Materials Science* 26.19 (Oct. 1991), pp. 5127–5133. DOI: 10.1007/BF01143202.

[59] R Hosemann, AM Hindeleh, and R Brückner. "Paracrystalline Lattice Structure of Silica Glass, alpha- and beta-Crystobalite." In: *physica status solidi (a)* 126.2 (1991), pp. 313–324. ISSN: 0031-8965. DOI: 10.1002/pssa.2211260203.

[60] J. Rivnay, R. Noriega, R. J. Kline, A. Salleo, and M. F. Toney. "Quantitative analysis of lattice disorder and crystallite size in organic semiconductor thin films." In: *Physical Review B* 84.4 (July 2011), p. 045203. DOI: 10.1103/PhysRevB.84.045203.

[61] B. E. Warren. *X-Ray Diffraction*. Dover Publications, 1990.

[62] D. A. Arms, R. S. Shah, and R. O. Simmons. "X-ray Debye-Waller factor measurements of solid ^{3}He and ^{4}He." In: *Phys. Rev. B* 67.9 (Mar. 2003), p. 094303. DOI: 10.1103/PhysRevB.67.094303.

[63] Paul Scherrer. "Bestimmung der Größe und der inneren Struktur von Kolloidteilchen mittels Röntgenstrahlen." In: *Nachrichten von der Gesellschaft der Wissenschaften zu Göttingen, Mathematisch-Physikalische Klasse* 2 (1918), 98–100. URL: http://eudml.org/doc/59018.

[64] R. Hosemann and A. M. Hindeleh. "Structure of Crystalline and Paracrystalline Condensed Matter." In: *Journal of Macromolecular Science - Physics* B34.4 (1995), pp. 327–356. DOI: 10.1080/00222349508219497.

[65] J. Als-Nielsen and D. McMorrow. *Elements of Modern X-ray Physics*. Second Edition. Wiley, 2011.

[66] A. Guinier and G. Fournet. *Small-angle scattering of X-rays*. Wiley, 1955.

[67] J. S. Pedersen. "Analysis of small-angle scattering data from colloids and polymer solutions: modeling and least-squares fitting." In: *Advances in Colloid and Interface Science* 70 (July 1997), pp. 171–210. DOI: 10.1016/S0001-8686(97)00312-6.

[68] H. Schnablegger and Y. Singh. *The SAXS guide: getting acquainted with the principles*. Anton Paar GmbH, Austria, 2013.

[69] A. K. Soper. "On the Determination of the Pair Correlation-function From Liquid Structure Factor Measurements." In: *Chemical Physics* 107.1 (Aug. 1986), pp. 61–74. DOI: 10.1016/0301-0104(86)85059-5.

[70] K. G. Yager, Y. G. Zhang, F. Lu, and O. Gang. "Periodic lattices of arbitrary nano-objects: modeling and applications for self-assembled systems." In: *Journal of Applied Crystallography* 47 (Jan. 2014), pp. 118–129. DOI: 10.1107/S160057671302832X.

[71] H. Dosch. "Evanescent absorption in kinematic surface Bragg diffraction." In: *Phys. Rev. B* 35.5 (Feb. 1987), pp. 2137–2143. DOI: 10.1103/PhysRevB.35.2137.

[72] A. Hexemer and P. Müller-Buschbaum. "Advanced grazing-incidence techniques for modern soft-matter materials analysis." In: *IUCrJ* 2 (Jan. 2015), pp. 106–125. DOI: 10.1107/S2052252514024178.

[73] P. Müller-Buschbaum. "Grazing incidence small-angle X-ray scattering: an advanced scattering technique for the investigation of nanostructured polymer films." In: *Analytical and Bioanalytical Chemistry* 376.1 (May 2003), pp. 3–10. DOI: 10.1007/s00216-003-1869-2.

[74] C. Frank, R. Banerjee, M. Oettel, A. Gerlach, J. Novák, G. Santoro, and F. Schreiber. "Analysis of island shape evolution from diffuse x-ray scattering of organic thin films and implications for growth." In: *Phys. Rev. B* 90.20 (Nov. 2014), p. 205401. URL: http://link.aps.org/doi/10.1103/PhysRevB.90.205401.

[75] S. Vass, J. S. Pedersen, J. Plestil, P. Laggner, E. Retfalvi, I. Varga, and T. Gilanyi. "Ambiguity in determining the shape of alkali alkyl sulfate micelles from small-angle scattering data." In: *Langmuir* 24.2 (Jan. 2008), pp. 408–417. DOI: 10.1021/la702139n.

[76] K.-D. Liss, A. Bartels, A. Schreyer, and H. Clemens. "High-energy X-rays: a tool for advanced bulk investigations in materials science and physics." In: *Textures and Microstructures* 35.3-4 (2003), pp. 219–252. DOI: 10.1080/07303300310001634952.

[77] *ID15A - Materials Chemistry and Materials Engineering*. Access: 14 March 2019. URL: https://www.esrf.eu/home/UsersAndScience/Experiments/StructMaterials/ID15A.html.

[78] *P21 Swedish Materials Science Beamline (SMS)*. 14.03.2019. DESY. URL: https://petra3-extension.desy.de/e84814/e260936/.

[79] *Beamline Characteristics - I12 (Diamond)*. Access: 14 March 2019. URL: https://www.diamond.ac.uk/Instruments/Imaging-and-Microscopy/I12/Beamline-Characteristics.html.

[80] M. Fuchs et al. "Laser-driven soft-X-ray undulator source." In: *Nature Physics* 5.11 (Nov. 2009), pp. 826–829. DOI: 10.1038/NPHYS1404.

[81] *ID31 - High-energy beamline for buried interface structure and materials processing*. Access: 13 March 2019. URL: https://www.esrf.eu/UsersAndScience/Experiments/StructMaterials/ID31.

[82] *P07 The High Energy Materials Science Beamline of Helmholtz-Zentrum Geesthacht (HZG) and DESY*. Access: 14 March 2019. URL: http://photon-science.desy.de/facilities/petra_iii/beamlines/p07_high_energy_materials_science/index_eng.html.

[83] *Parameters ESRF*. Access: 14 March 2019. URL: https://www.esrf.eu/home/UsersAndScience/Accelerators/parameters.html.

[84] *PETRA III - Facility Information*. Access 14 March 2019. URL: http://photon-science.desy.de/facilities/petra_iii/facility_information/index_eng.html.

[85] P. J. Chupas, K. W. Chapman, and P. L. Lee. "Applications of an amorphous silicon-based area detector for high-resolution, high-sensitivity and fast time-resolved pair distribution function measurements." In: *Journal of Applied Crystallography* 40 (June 2007), pp. 463–470. DOI: 10.1107/S0021889807007856.

[86] J. E. Daniels and M. Drakopoulos. "High-energy X-ray diffraction using the Pixium 4700 flat-panel detector." In: *Journal of Synchrotron Radiation* 16 (July 2009), pp. 463–468. DOI: 10.1107/S0909049509015519.

[87] M. J. Berger, J. H. Hubbell, S. M. Seltzer, J. Chang, J. S. Coursey, R. Sukumar, D. S. Zucker, and K. Olsen. *Xcom: Photon cross sections database, NIST standard reference database 8 (XGAM)*. 2010. Access: 15 March 2019. URL: http://physicsnist.gov/PhysRefData/Xcom/Text/XCOM.html.

[88] A.-C. Dippel, M. Roelsgaard, U. Boettger, T. Schneller, O. Gutowski, and U. Ruett. "Local atomic structure of thin and ultrathin films via rapid high-energy X-ray total scattering at grazing incidence." In: *IUCrJ* 6 (Mar. 2019), pp. 290–298. DOI: 10.1107/S2052252519000514.

[89] T. Egami and S. J. L. Billinge. *Underneath the Bragg Peaks: Structural Analysis of Complex Materials*. Elsevier Science, 2012.

[90] P. J. Chupas, X. Y. Qiu, J. C. Hanson, P. L. Lee, C. P. Grey, and S. J. L. Billinge. "Rapid-acquisition pair distribution function (RA-PDF) analysis." In: *Journal of Applied Crystallography* 36 (Dec. 2003), pp. 1342–1347. DOI: 10.1107/S0021889803017564.

[91] I. B. Ramsteiner, A. Schöps, H. Reichert, H. Dosch, V. Honkimaki, Z. Zhong, and J. B. Hastings. "High-energy X-ray diffuse scattering." In: *Journal of Applied Crystallography* 42.3 (2009), pp. 392–400. DOI: 10.1107/S0021889809011492.

[92] J. Gustafson, M. Shipilin, C. Zhang, A. Stierle, U. Hejral, U. Ruett, O. Gutowski, P.-A. Carlsson, M. Skoglundh, and E. Lundgren. "High-Energy Surface X-ray Diffraction for Fast Surface Structure Determination." In: *Science* 343.6172 (Feb. 2014), pp. 758–761. DOI: 10.1126/science.1246834.

[93] U. Hejral et al. "High-energy x-ray diffraction from surfaces and nanoparticles." In: *Physical Review B* 96.19 (Nov. 2017), p. 195433. DOI: 10.1103/PhysRevB.96.195433.

[94] F. Reikowski, T. Wiegmann, J. Stettner, J. Drnec, V. Honkimaki, F. Maroun, P. Allongue, and O. M. Magnussen. "Transmission Surface Diffraction for Operando Studies of Heterogeneous Interfaces." In: *Journal of Physical Chemistry Letters* 8.5 (Mar. 2017), pp. 1067–1071. DOI: 10.1021/acs.jpclett.7b00332.

[95] *P07 - High Energy Materials Science Beamline - Unified Data Sheet*. Access: 14 March 2019. URL: http://photon-science.desy.de/facilities/petra_iii/beamlines/p07_high_energy_materials_science/unified_data_sheet_p07/index_eng.html.

[96] W. Demtröder. *Experimentalphysik 3 - Atome, Moleküle und Festkörper, 3. Auflage*. Springer-Verlag Berlin Heidelberg, 2005.

[97] S. Hunklinger. *Festkörperphysik*. Oldenbourg Wissenschaftsverlag, München, 2009.

[98] S. Schiefer. "Crystal structure of fiber structured pentacene thin films." Dissertation. Ludwig-Maximilians-Universität München, 2007. URL: https://edoc.ub.uni-muenchen.de/7579/.

[99] I. Horcas, R. Fernandez, J. M. Gomez-Rodriguez, J. Colchero, J. Gomez-Herrero, and A. M. Baro. "WSXM: A software for scanning probe microscopy and a tool for nanotechnology." In: *Review of Scientific Instruments* 78.1 (Jan. 2007), p. 013705. DOI: 10.1063/1.2432410.

[100] F. Salah, B. Harzallah, and A. van der Lee. "Data reduction practice in X-ray reflectometry." In: *Journal of Applied Crystallography* 40 (Oct. 2007), pp. 813–819. DOI: 10.1107/S0021889807030403.

[101] R. Hosemann, M. P. Hentschel, F. J. Balta-Calleja, and G. S. Y. Yeh. "Generalisation of PP Ewald's intensity function for microparacrystals in colloids and their superstructures." In: *Journal of Physics C: Solid State Physics* 16.25 (1983), p. 4959. DOI: 10.1088/0022-3719/16/25/005.

[102] S. Fischer. "Small-angle X-ray scattering analysis of nanomaterials." Dissertation. 2017. URL: https://edoc.ub.uni-muenchen.de/23327/.

[103] E. M. Gullikson. *X-Ray Interactions With Matter - Index of Refraction*. URL: http://henke.lbl.gov/optical_constants/getdb2.html.

[104] B. L. Henke, E. D. G. M. Gullikson, and J. C. Davis. "X-Ray Interactions: Photoabsorption, Scattering, Transmission, and Reflection at E = 50-30,000 eV, Z = 1-92." In: *Atomic Data and Nuclear Data Tables* 54.2 (1993), pp. 181–342. ISSN: 0092-640X. DOI: 10.1006/adnd.1993.1013.

[105] C. A. Schneider, W. S. Rasband, and K. W. Eliceiri. "NIH Image to ImageJ: 25 years of image analysis." In: *Nature Methods* 9 (June 2012), pp. 671–675. DOI: 10.1038/nmeth.2089.

[106] G H. Vineyard. "Grazing-incidence diffraction and the distorted-wave approximation for the study of surfaces." In: *Phys. Rev. B* 26.8 (Oct. 1982), pp. 4146–4159. DOI: 10.1103/PhysRevB.26.4146.

[107] I. Hirosawa, T. Watanabe, T. Koganezawa, M. Kikuchi, and N. Yoshimoto. "Surface morphology of vacuum-evaporated pentacene film on Si substrate studied by in situ grazing-incidence small-angle X-ray scattering: I. The initial stage of formation of pentacene film." In: *Japanese Journal of Applied Physics* 57.3 (Mar. 2018), 03EG12. DOI: 10.7567/JJAP.57.03EG12.

[108] J. Ilavsky. "Nika: software for two-dimensional data reduction." In: *Journal of Applied Crystallography* 45.2 (2012), pp. 324–328. DOI: 10.1107/S0021889812004037.

[109] C. C. Stoumpos, C. D. Malliakas, and M. G. Kanatzidis. "Semiconducting Tin and Lead Iodide Perovskites with Organic Cations: Phase Transitions, High Mobilities, and Near-Infrared Photoluminescent Properties." In: *Inorganic Chemistry* 52.15 (Aug. 2013), pp. 9019–9038. DOI: 10.1021/ic401215x.

[110] C. C. Stoumpos et al. "Crystal Growth of the Perovskite Semiconductor CsPbBr3: A New Material for High-Energy Radiation Detection." In: *Crystal Growth & Design* 13.7 (July 2013), pp. 2722–2727. ISSN: 1528-7483. DOI: 10.1021/cg400645t.

[111] I. Bressler, J. Kohlbrecher, and A. F. Thunemann. "SASfit: a tool for small-angle scattering data analysis using a library of analytical expressions." In: *Journal of Applied Crystallography* 48 (Oct. 2015), pp. 1587–1598. DOI: 10.1107/S1600576715016544.

[112] F. Schreiber. "Organic molecular beam deposition: Growth studies beyond the first monolayer." In: *Physica Status Solidi A - Applications and Materials Science* 201.6 (May 2004), pp. 1037–1054. DOI: 10.1002/pssa.200404334.

[113] J. Yang and T.-Q. Nguyen. "Effects of thin film processing on pentacene/C60 bilayer solar cell performance." In: *Organic Electronics* 8.5 (2007), pp. 566–574. ISSN: 1566-1199. DOI: 10.1016/j.orgel.2007.04.005.

[114] S. J. Noever, S. Fischer, and B. Nickel. "Dual Channel Operation Upon n-Channel Percolation in a Pentacene-C60 Ambipolar Organic Thin Film Transistor." In: *Advanced Materials* 25.15 (2013), pp. 2147–2151. ISSN: 0935-9648. DOI: 10.1002/adma.201203964.

[115] T. Breuer and G. Witte. "Diffusion-Controlled Growth of Molecular Heterostructures: Fabrication of Two-, One-, and Zero-Dimensional C-60 Nanostructures on Pentacene Substrates." In: *ACS Applied Materials & Interfaces* 5.19 (Oct. 2013), pp. 9740–9745. DOI: 10.1021/am402868s.

[116] W. I. F. David, R. M. Ibberson, J. C. Matthewman, K. Prassides, T. J. S. Dennis, J. P. Hare, H. W. Kroto, R. Taylor, and D. R. M. Walton. "Crystal structure and bonding of ordered C60." In: *Nature* 353.6340 (1991), pp. 147–149. ISSN: 1476-4687. DOI: 10.1038/353147a0.

[117] G. B. M. Vaughan, P. A. Heiney, D. E. Cox, J. E. Fischer, A. R. McGhie, A. L. Smith, R. M. Strongin, M. A. Cichy, and A. B. Smith. "Structural phase transitions and orientational ordering in C70." In: *Chemical Physics* 178.1 (1993), pp. 599–613. ISSN: 0301-0104. DOI: 10.1016/0301-0104(93)85096-Q.

[118] C. Christides, I. M. Thomas, T. J. S. Dennis, and K. Prassides. "Pressure and Temperature Evolution of the Structure of Solid C70." In: *Europhysics Letters* 22.8 (1993), pp. 611–618. ISSN: 1286-4854. DOI: 10.1209/0295-5075/22/8/009.

[119] M. A. Verheijen, H. Meekes, G. Meijer, P. Bennema, J. L. de Boer, S. van Smaalen, G. van Tendeloo, S. Amelinckx, S. Muto, and J. van Landuyt. "The structure of different phases of pure C70 crystals." In: *Chemical Physics* 166.1-2 (1992), pp. 287–297. DOI: 10.1016/0301-0104(92)87026-6.

[120] H. Kawamura, M. Kobayashi, Y. Akahama, H. Shinohara, H. Sato, and Y. Saito. "Orientational ordering in solid C70 under high pressure." In: *Solid State Communications* 83.8 (1992), pp. 563–565. ISSN: 0038-1098. DOI: 10.1016/0038-1098(92)90652-P.

[121] H. Kiessig. "Interferenz von Röntgenstrahlen an dünnen Schichten." In: *Annalen der Physik* 402.7 (1931), pp. 769–788. DOI: 10.1002/andp.19314020702.

[122] S. Kowarik. "Thin film growth studies using time-resolved x-ray scattering." In: *Journal of Physics - Condensed Matter* 29.4 (Feb. 2017), p. 043003. DOI: 10.1088/1361-648X/29/4/043003.

[123] B. Nickel, R. Barabash, R. Ruiz, N. Koch, A. Kahn, L. C. Feldman, R. F. Haglund, and G. Scoles. "Dislocation arrangements in pentacene thin films." In: *Phys. Rev. B* 70.12 (Sept. 2004), pp. 125401–. DOI: 10.1103/PhysRevB.70.125401.

[124] R. Ruiz, A. C. Mayer, G. G. Malliaras, B. Nickel, G. Scoles, A. Kazimirov, H. Kim, R. L. Headrick, and Z. Islam. "Structure of pentacene thin films." In: *Appl. Phys. Lett.* 85.21 (Nov. 2004), pp. 4926–4928. ISSN: 0003-6951. DOI: 10.1063/1.1826229.

[125] R. Herino, G. Bomchil, K. Barla, C. Bertrand, and J. L. Ginoux. "Porosity and Pore Size Distributions of Porous Silicon Layers." In: *Journal of The Electrochemical Society* 134.8 (Aug. 1987), pp. 1994–2000. DOI: 10.1149/1.2100805.

[126] M.I.J. Beale, J.D. Benjamin, M.J. Uren, N.G. Chew, and A.G. Cullis. "An experimental and theoretical study of the formation and microstructure of porous silicon." In: *Journal of Crystal Growth* 73.3 (1985), pp. 622–636. ISSN: 0022-0248. DOI: 10.1016/0022-0248(85)90029-6.

[127] K. Lejaeghere, V. Van Speybroeck, G. Van Oost, and S. Cottenier. "Error Estimates for Solid-State Density-Functional Theory Predictions: An Overview by Means of the Ground-State Elemental Crystals." In: *Critical Reviews in Solid State and Materials Sciences* 39.1 (Jan. 2014), pp. 1–24. DOI: 10.1080/10408436.2013.772503.

[128] R. W. G. Wyckoff. *Crystal Structures*. Second edition. Interscience Publishers, New York, 1963.

[129] K. Tanaka, T. Takahashi, T. Ban, T. Kondo, K. Uchida, and N. Miura. "Comparative study on the excitons in lead-halide-based perovskite-type crystals CH3NH3PbBr3 CH3NH3PbI3." In: *Solid State Communications* 127.9-10 (Sept. 2003), pp. 619–623. ISSN: 0038-1098. DOI: 10.1016/S0038-1098(03)00566-0.

[130] M. Hirasawa, T. Ishihara, T. Goto, K. Uchida, and N. Miura. "Magnetoabsorption of the lowest exciton in perovskite-type compound (CH3NH3)PbI3." In: *Physica B: Condensed Matter* 201 (1994), pp. 427–430. ISSN: 0921-4526. DOI: 10.1016/0921-4526(94)91130-4.

[131] A. D. Yoffe. "Semiconductor quantum dots and related systems: electronic, optical, luminescence and related properties of low dimensional systems." In: *Advances In Physics* 50.1 (Jan. 2001), pp. 1–208. DOI: 10.1080/00018730010006608.

[132] G. A. Elbaz, D. B. Straus, O. E. Semonin, T. D.D. Hull, D. W. Paley, P. Kim, J. S. Owen, C. R. Kagan, and X. Roy. "Unbalanced Hole and Electron Diffusion in Lead Bromide Perovskites." In: *Nano Lett.* 17.3 (Mar. 2017), pp. 1727–1732. ISSN: 1530-6984. DOI: 10.1021/acs.nanolett.6b05022.

[133] M. Engel, B. Stühn, J. J. Schneider, T. Cornelius, and M. Naumann. "Small-angle X-ray scattering (SAXS) off parallel, cylindrical, well-defined nanopores: from random pore distribution to highly ordered samples." In: *Applied Physics A - Materials Science & Processing* 97.1 (Oct. 2009), pp. 99–108. DOI: 10.1007/s00339-009-5346-4.

[134] G. Pépy and A. Kuklin. "An orientation process to study nuclear membranes by small angle neutron scattering." In: *Nuclear Instruments & Methods in Physics Research Section B - Beam Interactions with Materials and Atoms* 185 (Dec. 2001), pp. 198–203. DOI: 10.1016/S0168-583X(01)00833-3.

[135] O. Glatter and O. Kratky. *Small angle x-ray scattering*. London: Academic Press, 1982, pp. –.

[136] M. J. Ashley, M. N. O'Brien, K. R. Hedderick, J. A. Mason, M. B. Ross, and C. A. Mirkin. "Templated Synthesis of Uniform Perovskite Nanowire Arrays." In: *J. Am. Chem. Soc.* 138.32 (Aug. 2016), pp. 10096–10099. ISSN: 0002-7863. DOI: 10.1021/jacs.6b05901.

[137] V. Malgras, S. Tominaka, J. W. Ryan, J. Henzie, T. Takei, K. Ohara, and Y. Yamauchi. "Observation of Quantum Confinement in Monodisperse Methylammonium Lead Halide Perovskite Nanocrystals Embedded in Mesoporous Silica." In: *Journal of the American Chemical Society* 138.42 (Oct. 2016), pp. 13874–13881. DOI: 10.1021/jacs.6b05608.

[138] S. M. George. "Atomic Layer Deposition: An Overview." In: *Chem. Rev.* 110.1 (Jan. 2010), pp. 111–131. ISSN: 0009-2665. DOI: 10.1021/cr900056b.

[139] J. M. Roemer. "Nukleation von C70-Aggregaten auf Pentacen-Dünnschichten zur Nanostrukturierung organischer Grenzflächen." Master's Thesis. Ludwig-Maximilians-Universität München, 2014.

[140] M. Soosen Samuel, L. Bose, and K. C. George. "Optical properties of ZnO nanoparticles." In: *Academic Review* (2009), pp. 57–65.

[141] P. Cottingham and R. L. Brutchey. "On the crystal structure of colloidally prepared CsPbBr3 quantum dots." In: *Chem. Commun.* 52.30 (2016), pp. 5246–5249. ISSN: 1359-7345. DOI: 10.1039/C6CC01088A.

[142] X. Y. Che, B. Traore, C. Katan, M. Kepenekian, and J. Even. "Does Rashba splitting in CH3NH3PbBr3 arise from 2 x 2 surface reconstruction?" In: *Physical Chemistry Chemical Physics* 20.14 (Apr. 2018), pp. 9638–9643. DOI: 10.1039/c8cp00745d.

[143] K. Ishikawa and T. Uemori. "Surface relaxation in ferroelectric perovskites." In: *Physical Review B* 60.17 (Nov. 1999), pp. 11841–11845. DOI: 10.1103/PhysRevB.60.11841.

[144] H. Mashiyama, Y. Kawamura, E. Magome, and Y. Kubota. "Displacive character of the cubic-tetragonal transition in $CH_3NH_3PbX_3$." In: *Journal of the Korean Physical Society* 42 (Apr. 2003), S1026–S1029.

[145] M. Rodová, J. Brožek, K. Knížek, and K. Nitsch. "Phase transitions in ternary caesium lead bromide." In: *Journal of Thermal Analysis and Calorimetry* 71.2 (2003), pp. 667–673. DOI: 10.1023/A:1022836800820.

[146] T. F. Retajczyk and A. K. Sinha. "Elastic Stiffness and Thermal-expansion Coefficients of Various Refractory Silicides and Silicon-nitride Films." In: *Thin Solid Films* 70.2 (1980), pp. 241–247. DOI: 10.1016/0040-6090(80)90364-8.

[147] T. Middelmann, A. Walkov, G. Bartl, and R. Schödel. "Thermal expansion coefficient of single-crystal silicon from 7 K to 293 K." In: *Physical Review B* 92.17 (Nov. 2015), p. 174113. DOI: 10.1103/PhysRevB.92.174113.